FLEXIBLE ALGAE PHOTO-BIOREACTORS IN WATER WAVES

Bright Felix Chifamba

Submitted in fulfilment of the requirements of the degree of
Master of Science in Engineering (Civil),
College of Agriculture,
Engineering and Science,
University of KwaZulu Natal

2016

Supervisor: Professor Derek D Stretch

I. DECLARATION

I Bright Felix Chifamba hereby declare that this research project is my own work. No part of this dissertation has been submitted to any other institution. The contributions of other authors or researchers are clearly referenced in-text and on the reference list page. Figures and tables obtained from other sources are clearly referenced. This research was done under the supervision of Professor Derek D Stretch, the Professor of Environmental fluid mechanics at the school of engineering, University of KwaZulu-Natal.

……..

Bright Felix Chifamba

Date …..... /…… /……

As the candidate's Supervisor I agree/do not agree to the submission of this dissertation.

……..

Professor Derek D. Stretch

Date …… /……. /……..

II. ACKNOWLEDGEMENTS

I thank God Almighty for making this research a success by giving me the strength to work, health and knowledge. I want to thank my supervisor Professor Derek Stretch for his endless supervision and financial support throughout my research. I want to thank Dr Katrin Tirok, Dr Stefano Corbella and Dr Justin Pringle and for their assistance. I thank my classmates for their support and encouragement. I want to thank the laboratory technical team namely Mr Logan Govendar, Ms Fathima Ali, Mr Logan Pillay and Mr Sydney Mpungose for their assistance in setting up the experiments. Lastly but not least, my family for their endless support.

I. ABSTRACT

Due to the irreversible and alarming depletion of fossil fuels, the world is facing a serious energy crisis. Biofuels are potential carbon neutral and renewable sources of energy that can replace fossil fuels. The broad objective of this research is to contribute to developing a system for microalgae cultivation as a biomass feedstock for biofuel production, waste water treatment and CO_2 sequestration. Photo-bioreactor systems consisting of flexible tubes (FTPBRs) deployed in the ocean can be used for the cultivation of microalgae and wastewater treatment. FTPBRs can utilise ocean discharges of wastewater as a source of nutrients (nitrogen and phosphorus), together with solar energy and waste CO_2 for cultivating microalgae. Ocean wave energy can be utilised to power the operational processes of FTPBRs such as pumping, mixing and harvesting of microalgal biomass. In this research a piston wave generator and a wave tank were the modelling equipment used to simulate simplified ocean waves. A flexible tube filled with water was deployed in the wave tank in order to investigate the effect of waves on the flow. Wave-induced pressures drive periodic tube deformations, pumping water through the flexible tube in a manner analogous to peristalsis of substances in vascular systems. The average flows were measured as a function of wave parameters (e.g. frequency f, water depth h and wave height H), the tube's elevation relative to the surface of waves and the internal pressure Δp of the tube. Results show that flow rate increases with h and H but decreases with increase in Δp. Even though flow increases with h, there is a limit to this effect since the wave- induced pressure perturbations also decay with depth below the free surface. The wave height H increases with frequency f but flow rate increases with H at constant f. This implies that flow through tube is mainly influenced by H and that f has little effect on the flow rate. Approximately the same volume of water flows at constant H and time τ but the size of the pulses depends on the wave frequency. Particle tracking velocimetry (PTV) was used to measure the local velocities of polystyrene particles seeded in the flow as representatives of the actual fluid particles. Tube constrictions drive fluid ahead of them in the wave direction but allow for the backward movement of water within the constrictions. Where the flow constriction expands, adverse pressure gradients cause the particles to decelerate resulting in a burst of turbulence. The turbulent mixing is essential for enhancing the availability of nutrients to the microalgae cultivar. Even though the movement of fluid in the flexible tube is oscillatory, net flow is in the wave direction.

II. TABLE OF CONTENTS

III. LIST OF FIGURES

IV. LIST OF TABLES

V. IMPORTANT NOMENCLATURE

CO_2	Carbon dioxide
O_2	Oxygen
h	Still water depth
f	Wave frequency
H	Wave height
L	Wave length
k_p	Wave number
g	Gravitational acceleration (m/s^2)
Δp	Pressure head
D	Tube's diameter
D_y	Tube's cross sectional dimension in the vertical direction
D_z	Tube's cross sectional dimension in the horizontal direction
v_x	Horizontal component of velocity
v_y	Vertical component of velocity

VI. IMPORTANT ACRONYMS

PTV	Particle tracking velocimetry
PIV	Particle image velocimetry
FTPBR	Flexible tubular photo-bioreactors
PBR	Photo-bioreactor
GHG	Greenhouse gas
SWL	Still water level
LDPE	Low-density polyethylene

CHAPTER 1 : INTRODUCTION

1.1 Project description

Flexible tubes filled or partially filled with water deployed in ocean waves are distorted by the waves while also influencing the wave fields. The distortions of the tubes drive a flow of the fluid that they contain in a way analogous to peristaltic flows in vascular systems. In this project the fluid mechanics of this phenomenon will be explored by measuring the flow induced in the tubes for various wave parameters such as frequency, celerity and wave height. This will provide the knowledge and insights to utilise such systems as bioreactors for application to the production of algal biomass for renewable energy, CO_2 sequestration and waste water treatment.

1.2 Background of the research

Due to irreversible depletion of fossil fuels, the world is facing a serious energy crisis (see e.g. Hoel and Kvemdokk, 1996). The exploitation of these non-renewable energy sources has caused problems such as environmental pollution, global warming due to greenhouse gas (GHG) emissions and health problems such as skin cancer (see e.g. Powlson et al. 2005). Biofuels are viewed as environmentally sustainable energy sources which are a potential replacement of non-renewable fossil fuels (Patil et al. 2008). The broad objective of this project is to contribute to developing a system for algae cultivation as a feedstock for biofuel production and wastewater treatment. Photo-bioreactor systems that consist of flexible tubes (FTPBRs) deployed in oceans can be used to clean wastewater (Hoffmann, 1998), to grow algae for biofuel production and for CO_2 sequestration. FTPBRs can utilise ocean discharges of wastewater from coastal cities as the source of nutrients (nitrogen and phosphates) and waste CO_2 from power plants and heavy industries to cultivate algae. The other main input for algae cultivation is solar energy which is required for photosynthesis where it is converted to chemical energy. Ocean wave energy can be utilised to power the operational processes of the FTPBRs such as pumping, mixing and harvesting of algae. The turbulence caused by ocean waves

drives the mixing, suspension and transportation of microalgal cells and they enhance the availability of nutrients.

Laboratory wave tanks are used to simulate simplified narrow-band ocean waves. An FTPBR system will be built in the laboratory and the fluid mechanics of its flexible tubes will be investigated experimentally. The flexible tube deployed in a wave tank will be influenced by the pressures of the simplified progressive water waves of different characteristics. Ultimately the effects of flow and turbulence on the functioning of the algae in these photo-bioreactors can be elucidated in order to develop insight regarding the optimal conditions for operating these bioreactors. However, the growing of algae in the FTPBR system is beyond the scope of this research. Particle tracking velocimetry (PTV) or particle image velocimetry (PIV) can be used to investigate the turbulence structure and the flow fields in filled or partially filled tubes.

1.3 Research questions

1. What are the qualitative and quantitative features of the flow fields induced inside flexible tubes by periodic waves of various amplitudes, frequencies and water depths?
2. What are the pumping characteristics of these wave driven systems?

1.4 Aims

1. To investigate the fluid mechanics of flexible tube bio-reactors (FTPBRs) in progressive water waves

2. To contribute to developing a system for algae cultivation as a feedstock for biofuel production, carbon dioxide sequestration and wastewater treatment

1.5 Objectives

1. To build a simple FTPBR system consisting of a piston paddle wave generator and a wave tank for simulating simplified narrow-band ocean water waves.
2. To measure the average flow rates through flexible tubes filled with water and induced by various wave characteristics
3. To measure the effects of wave frequency, wave height, the tube's internal pressure and its elevation relative to the waves' free surface on the flow rates.
4. To measure the magnitudes of deformations (shape analysis) in flexible tubes under various wave conditions.
5. To investigate the qualitative and quantitative structure of turbulence induced by progressive waves on the flexible tube.

1.6 Approach

The methodological approach consisted of a literature review where relevant sources of information were reviewed in detail. A simple FTPBR together with a piston water wave generator are the physical modelling tools that were used for the experiments of this research project. The wave generator consisted of a piston paddle system that generated periodic progressive waves. The flow fields in the FTPBR were investigated using particle tracking velocimetry (PTV). The PTV requires an optically transparent test section, a digital image recording system, an illuminating light source such as a high energy strobe light or a fluorescent lamp and a computer software such as Matlab for post image processing. Tracer polystyrene particles were seeded in the fluid in the flexible tube of the FTPBR system to characterise the flow of the actual fluid particles. The tracer particles must follow the streamlines of the flow and must be efficient scatters of the illuminating light for them to be an acceptable representation of the actual fluid particles. A digital video camera was used to record the motion of tracer particles in the fluid. The displacement of each particle in two successive images and the exposure time are then used to calculate the approximate local velocities of each of the particles in the fluid. The velocity vectors were located randomly in the field of view. The results of the experiments provided new insights into the flow fields induced in distorted flexible tubes by progressive waves. Errors were minimised by careful selection of experiment conditions.

1.7 Structure of the research

This document consists of 4 other chapters. Chapter 2 is the literature review of relevant contributions by other researchers. Chapter 3 is the methodology describing the experimental procedures for this research. The results of the experiments are presented and discussed in chapter 4. Chapter 5 discusses conclusions obtained from this research as well as recommendations for future work related to this research.

CHAPTER 2 : LITERATURE REVIEW

Fossil fuels are currently the main sources of fuel energy but their exploitation is irreversible. The production of fossil fuels has negative impacts on the environment such as air pollution and acidification of natural bodies. There is need for sustainable and potential carbon-neutral sources of energy. Biofuels are renewable sources of energy which have the potential to replace the fossil fuels (see e.g. Chisti, 2007). This research focuses on microalgae for the production of biofuels and wastewater treatment. Microalgae can be grown and harvested in flexible tubular photo- bioreactors (FTPBRs). The fluid mechanics of flexible tubes deployed in progressive water waves will be investigated in the subsequent chapters of this thesis. Ocean water waves can provide the energy required for pumping and mixing of microalgae cells with nutrient-enriched fresh-water in the cultivation processes. This chapter reviews previous work by other researchers on how microalgae can be grown in FTPBR systems together with the applications of techniques such as PIV and PTV in measuring instantaneous fluid flows through FTPBR systems. Based on the literature review, a simple FTPBR system will be built together with a piston wave generator which will be the modelling equipment for waves of the experiment of the research.

2.1. Current fuel problems

Fossil fuels are non-renewable sources of energy and they are depleting at an alarming rate that it is feared the world is facing an energy crisis. Currently, researchers are searching for reliable, sustainable and cleaner sources of fuel energy that can replace fossil fuels. The production of fossil fuels and their uses have serious negative environmental impacts. Under combustion, fossil fuels emit CO_2 which is a greenhouse gas (GHG). The emission of GHGs is believed to be responsible for negative impacts on the environment such as global warming (see e.g. Brennan and Owende, 2010) and acidification of natural water bodies (Mata et al. 2010) which has negative effects on the biodiversity of the marine ecosystem. One of the GHGs, CO_2 reacts with water, raising the pH of the water which can negatively affect the growth of plants and animals in that water body.

Biofuels produced from microalgal biomass are potential carbon-neutral sources of energy that can replace fossil fuels if grown on scales that meet current and future demand. The cultivation of microalgae plays an important role in the sequestration of CO_2 from power plants and other industries. This research will give insight on the microalgae cultivation in FTPBR for biofuel production. The actual cultivation of microalgae will not be covered in the experiments of this research.

2.2 Microalgae

2.2.1 What are microalgae?

Microalgae are single-cell or simple multi-cell photosynthetic micro-organisms (Mata et al. 2010). Microalgae can duplicate themselves during photosynthesis by converting solar energy into chemical energy (Richmond, 2004). They require nutrients such as nitrogen and phosphorus and adequate aeration (Mata et al. 2010) and fresh water for their growth (see e.g. Chisti, 2007). Like other photosynthetic plants or organism, microalgae cells inhale CO_2 while producing O_2 as a by-product.

2.2.2 Why microalgae?

Since microalgae can be grown offshore in FTPBRs, there is no competition for land so the growing of food crops is not compromised (Chisti, 2007). Microalgae can also be cultivated in ponds constructed in areas which are not suitable for agriculture. Besides production from microalgae, biofuels can also be produced from palm oil, soybeans, jatropha, corn oil, coconut, canola, animal fat etc. (Chisti, 2007) but previous researches show that microalgae cells have the highest oil yields as shown in Table 2-1 in Mata et al. (2010).

Table 2-1 Comparison of microalgae with other plants in terms of oil content, land use and biofuel production. Source: Mata et al. (2010)

Plant source	Seed oil content (% oil by wt in biomass)	Oil yield (L oil/ha year)	Land use (m^2 year/kg biodiesel)	Biodiesel productivity (kg biodiesel/ha year)
Corn/Maize (*Zea mays* L.)	44	172	66	152
Hemp (*Cannabis sativa* L.)	33	363	31	321
Soybean (*Glycine max* L.)	18	636	18	562
Jatropha (*Jatropha curcas* L.)	28	741	15	656
Camelina (*Camelina sativa* L.)	42	915	12	809
Canola/Rapeseed (*Brassica napus* L.)	41	974	12	862
Sunflower (*Helianthus annuus* L.)	40	1070	11	946
Castor (*Ricinus communis*)	48	1307	9	1156
Palm oil (*Elaeis guineensis*)	36	5366	2	4747
Microalgae (low oil content)	30	58,700	0.2	51,927
Microalgae (medium oil content)	50	97,800	0.1	86,515
Microalgae (high oil content)	70	136,900	0.1	121,104

Table 2-1 shows that the 3 microalgae species have by far higher biodiesel productivity and growth rates as compared to agricultural crops. Biodiesel production from microalgae also uses the least land as compared to other plant sources. Microalgae grow rapidly, they can double their biomass within a day (Chisti, 2007). These are some of the reasons for choosing microalgae over other plant sources for biofuel production. The use of microalgae in wastewater treatment will be discussed briefly in the subsequent subsection.

2.2.3 Microalgae in photo-bioreactors (PBRs) and use in wastewater treatment

Many factors such as the intensity of sunlight, availability of nutrients and the concentration of CO_2 affect the production of microalgal biomass. Artificial light can also be used but that would increase the cost of production. There are thousands of microalgae species but photo-bioreactors (PBRs) can make it possible to culture specific species for optimal productivity (Chisti, 2007). Most PBR systems consist of transparent plastic tubes which allow sunlight to pass through. The diameters of the tubes must be limited to allow sunlight to penetrate through the liquid medium which is usually dense with nutrients (Chisti, 2007). The nutrients for microalgae cultivation (nitrogen, phosphorus and irons) are readily available in wastewater and can be fed into the systems for wastewater treatment (Park et al. 2011). This means that wastewater is treated in the process of microalgae cultivation and it is an alternative way of treating wastewater.

Waste water for many coastal cities is discharged into oceans which makes it readily available for use in the PBRs at little or no cost.

Waste CO_2 from power plants and other industries is another raw input readily available at little cost. The microalgae and wastewater in the PBR system must be pumped and mixed in order to enhance the availability of nutrients to the microalgae cells (Chisti, 2007). Ocean waves can be utilised for the pumping and mixing processes of the system. The wave induced pressures deform flexible tube photo-bioreactors (FTPBRs) in a way analogous to peristalsis of substances in the vascular system. The tubes must be limited to a certain length to reduce potential oxygen (O_2) accumulation, the depletion of CO_2 as well as pH variation along the tube (Brennan and Owende, 2010). This suggests that efficient FTPBR systems should have many shorter reactor units rather than few longer ones. However, CO_2 can be supplied through gas permeable silicone membranes if necessary (Lee and Hing, 1989). The membranes should be small enough to allow gaseous fluid flow only.

2.3 Water waves classification

In this research, water waves are the source of energy for the pumping and mixing of fluid around FTPBRs. Waves of various characteristics occur naturally in oceans. Each wave has an effect on the average pumping rate of fluid around the FTPBR systems. The energy of a wave is proportional the square of its amplitude and the bulk of the total energy of a wave is within a water height of $\frac{1}{2}L$ (where L is the wavelength) from the wave surface (see e.g. Dean and Dalrymple, 2010). The influence of waves on the motion of water particles therefore decreases with increase in water depth h (see e.g. Smith, 1983).

Waves are usually classified in terms of their L/h ratios. Water waves tend to be shallow when $L/h \geq 20$ (Chappell, 1969). However, waves do not suddenly become shallow when $L/h = 20$ but it is a gradual process where the limiting conditions become more accurate towards this value. Waves are referred to as deep when $L/h < 2$ (Chappell, 1969). Waves are also classified according to the wave steepness i.e. wave height to wave length ratio (H/L). Waves break when they reach a limiting steepness value that occurs when water particles on the wave crest reaches a centripetal acceleration equal to the

gravitational acceleration g (Chappell, 1969). The H/L and L/h ratios are useful in establishing geometric comparisons between laboratory waves and natural ocean waves. Froude and Reynolds numbers are also useful in geometric and similarity analyses. Celerity c of a wave is given by equation 2.1 as follows:

$$c = \sqrt{\frac{gL}{2\pi} tanh \frac{2\pi h}{L}} \qquad (2\text{-}1)$$

where $g, h \; and \; L$ are the gravitational acceleration, still water depth and wavelength respectively (Chappell, 1969).

For waves with $L/h \; < 2$, the values of $tanh \frac{2\pi h}{L}$ in radians approach 1 then equation 2.1 for celerity reduces to $c = \sqrt{\frac{gL}{2\pi}}$ and when $L/h \; \geq 20$, the values of $tanh \frac{2\pi h}{L}$ approach $\frac{2\pi h}{L}$ and the celerity is given as $c = \sqrt{gh}$ (Chappell, 1969). Celerity for shallow water waves is dependent on the still water depth h since g is a constant.

Waves can also be classified as either stationary or progressive waves. This research focuses only on progressive waves. A simple sinusoidal progressive wave is defined as follows:

$$\eta(x,t) = \frac{H}{2} cos(kx - \sigma t) \qquad (2\text{-}2)$$

where

$\eta(x,t)$ is the wave surface profile with respect to time t and distance x from reference point.

k (a wave number = $\frac{2\pi}{L}$) and $\sigma = \frac{2\pi}{T}$ where T is the wave period (Dean and Dalrymple, 2010).

Figure 2-1 shows graphs of $\eta(x,t)$ at two time steps Δt apart, with L = 2000 mm and $H = 15mm$. The waves are moving from right to left.

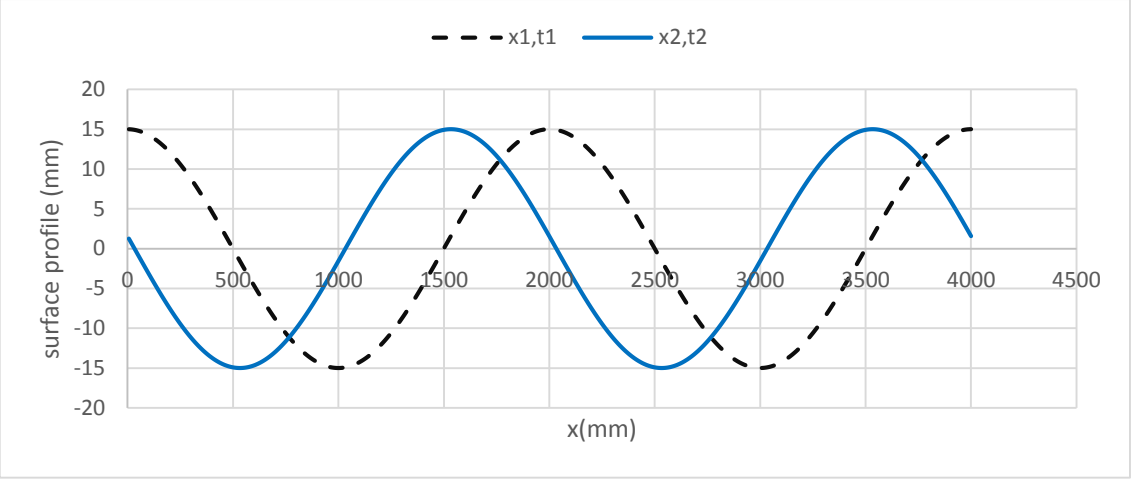

Figure 2-1 The graphs of η(x,t) at two time steps Δt apart. The waves are moving from right to left

Shallow water ocean waves are not always sinusoidal, cnoidal waves occur when water depth h is less than a tenth of the wavelength L (Wiegel, 1959). Both sinusoidal and cnoidal waves induce non uniform pressures on flexible tubes filled or partially filled with water, creating instantaneous flow fields within the tubes, therefore their effects are important in this research.

The wave induced pressures p are given by:

$$p = -\rho g z + \rho g \eta K_p z \qquad (2\text{-}3)$$

where z is as illustrated in Figure 2-2, h is the still water depth, ρ is the density of water, g is the gravitational acceleration and $K_p z = \frac{\cosh k(h+z)}{\cosh kh}$ (Dean and Dalrymple, 2010). $K_p z$ is a pressure response factor. The terms $\rho g z$ and $\rho g \eta K_p z$ are the hydrostatic and dynamic components of p respectively.

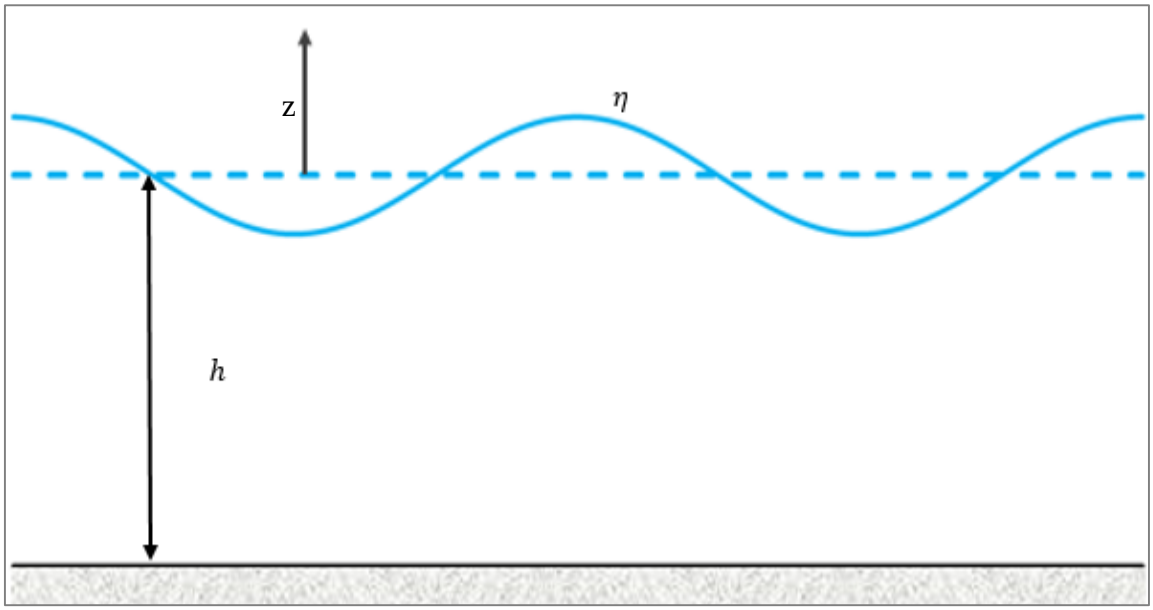

Figure 2-2 A schematic representation of wave parameters h and z and the wave free surface profile η.

The dynamic pressures are created due to the displacement of the free surface of the wave (see e.g. Dean and Dalrymple, 2010). The wave dynamic pressures are dependent on z and vary along the wave profile. The hydrostatic pressure is dependent on the water depth h. Highest pressure p occurs under crests and lowest pressure under troughs.

2.4 Laboratory wave generators

Laboratory wave generators are the modelling tools for simulating simplified narrow-band ocean waves. Laboratory models are useful in designing full-scale prototypes. A geometric comparison between laboratory models and prototypes can be established through the use of ratios such as Froude numbers, Reynolds numbers, steepness ratios etc. It is recommended to build feasible laboratory models before attempting to build the full-scale prototypes.

Various types of wave generators such as piston, flanger and plunger wave generators can be used for the laboratory experiments (Chappell, 1969). In this research, a piston type generator with a flat paddle will be used since it is readily available in the laboratory. The piston wave generator will be tested to see if it is consistent with the shallow water wave generator theory. The theory states that the volume of water displaced by the paddle of

the wave generator is equal to the volume of water in the crest of the generated propagating waveform (see e.g. Dean and Dalrymple, 2010) as shown in Figure 2-3. This was first published by Biesel and Suquet (1951). The two shaded areas in Figure 2-3 are approximately equal for shallow water waves.

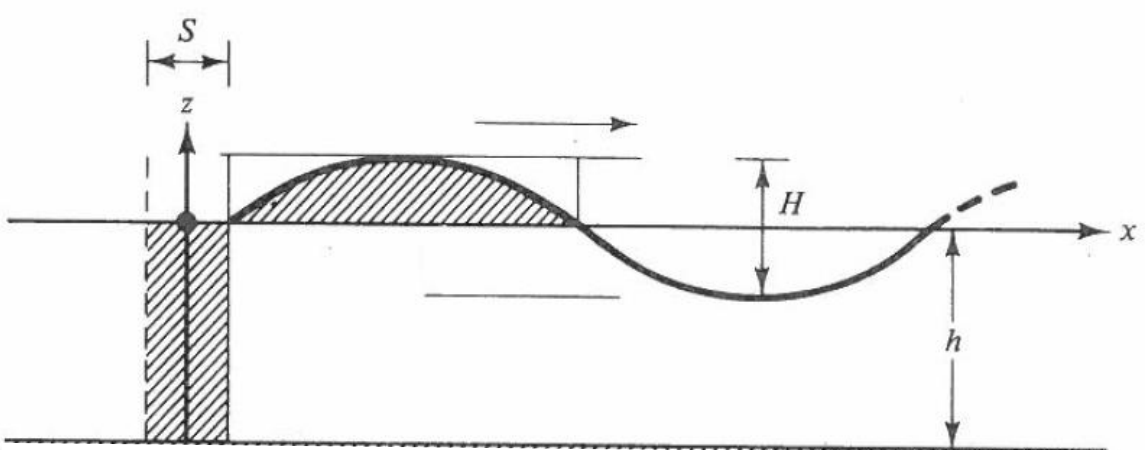

Figure 2-3 The shallow water wavemaker theory for piston wave generator. S is the paddle stroke, H is wave height and h is still water depth. The waves are moving in the direction of x. (source: Dean and Dalrymple, 2010).

For a piston wave generator with a constant stroke S, the displaced volume of water with still water depth h over the full stroke S is equal to Sh.

The volume of water in the crest is equal to:

$$\int_0^{L/2} \left(\frac{H}{2}\right) Sin\ kx\ dx = H/k \qquad (2\text{-}4)$$

The shallow water wave theory assumes that:

$$Sh = \left(\frac{H}{2}\right) \int_0^{L/2} Sin\ kx\ dx \qquad (2\text{-}5)$$

$$= \frac{H}{2}\ \frac{1}{k}\ [-\cos kx]_0^{L/2}$$

$$= \frac{H}{2}\ \frac{L}{2\pi}\ \left[\left(-\cos\frac{2\pi}{L}x\frac{L}{2}\right) - (-\cos 0)\right]$$

$$= \frac{H}{2}\ \frac{L}{2\pi}\ [1+1] = \frac{H}{k}\,, \qquad (2\text{-}6)$$

whence $H/S = kh$. For a piston wave generator, H/S is given by equation 2.7:

$$\frac{H}{S} = \frac{4sinh^2 kh}{sinh\,2kh+2kh} \text{ (see e.g. Hughes, 1993)} \qquad (2\text{-}7)$$

Plotting H/S against kh gives a linear relationship for shallow water waves.

2.5 Peristalsis in flexible tubes, shape analysis and models

This section discusses peristalsis of fluids such as water in flexible tubes and vascular systems. Peristalsis in flexible tubes is a process of fluid transportation that arise from progressive waves of area change (Muthu et al. 2001) travelling along the flexible tubes/vessels (Xiao and Damodaran, 2002). The movement of food from the mouth down through the oesophagus and the urine flow in the ureter are some examples of peristaltic motion (see e.g. Misra and Pandey, 2001). Wave-induced pressures deform flexible tubes in such a way that the fluid flux is pumped through the tubes. Since the external pressures are not constant along the tube as discussed earlier, dynamic constrictions are created along the tubes which pump the fluid flux. The constrictions move along the tube at the same frequency as the external progressive waves. Grotberg and Jensen (2004) performed experiments using an enclosed system consisting of an elastic tube segment between rigid tubes. The fluid flux was driven by the pressure drop in the elastic tube. The motion of the tube's wall was described by equation 2.8:

$$\xi(Z,\tau) = a\,cos[2\pi(Z - c\tau)/\lambda] \qquad (2\text{-}8)$$

where

Z and R are the axial and radial coordinates respectively,

c and a are the velocity and amplitude of the waves respectively,

τ and λ are time and wavelength respectively,

$\xi(Z,\tau)$ is the radial displacement of tube's wall from the mean position (Muthu et al. 2001).

Figure 2-4 in Muthu et al. (2001) is an illustration of the peristaltic wave motion in a flexible tube.

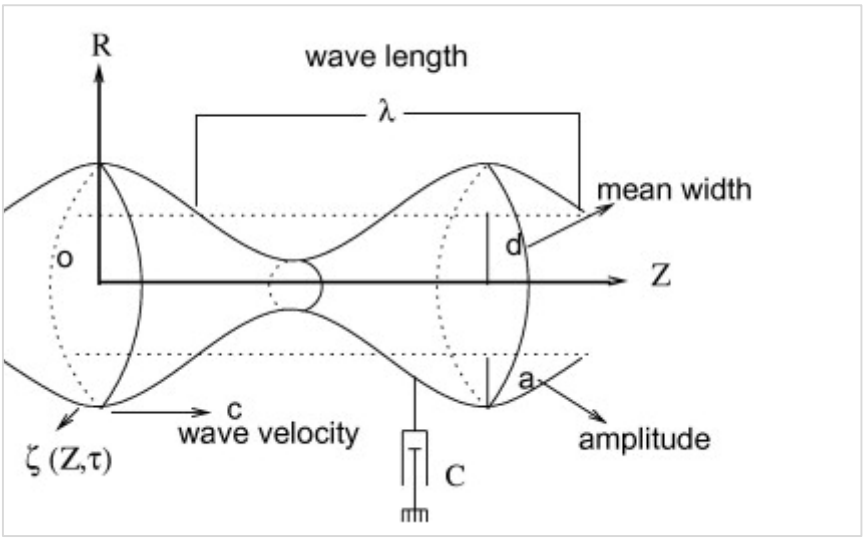

Figure 2-4 The peristaltic wave motion in a cylindrical flexible tube (source: Muthu et al. 2008).

Hayat et al. (2002) gave a slightly different equation for the movement of a flexible tube wall deployed in progressive water waves. The equation is as follows:

$$R_{wall} = \xi(Z,\tau) = a + b\ sin[\frac{2\pi}{\lambda}(Z - c\tau)] \qquad (2\text{-}9)$$

where

R_{wall} is the radial displacement of the tube,

a is the tube's radius,

b is the wave amplitude.

The equation is valid for an inextensible flexible tube containing an incompressible fluid like water. When the interior pressure of a flexible tube is greater than exterior pressures, the cross-sectional area of the tube becomes circular in shape (see e.g. Jensen, 2013). Under these conditions, the tube resists the change in area but when the external pressure is greater than interior pressure, it buckles and deforms into an elliptical cross-sectional shape (Jensen, 2013). The deformation of flexible tubes can also be illustrated using a Starling resistor shown in Figure 2-5. Starling resistor is usually used for medical experiments related to vascular systems.

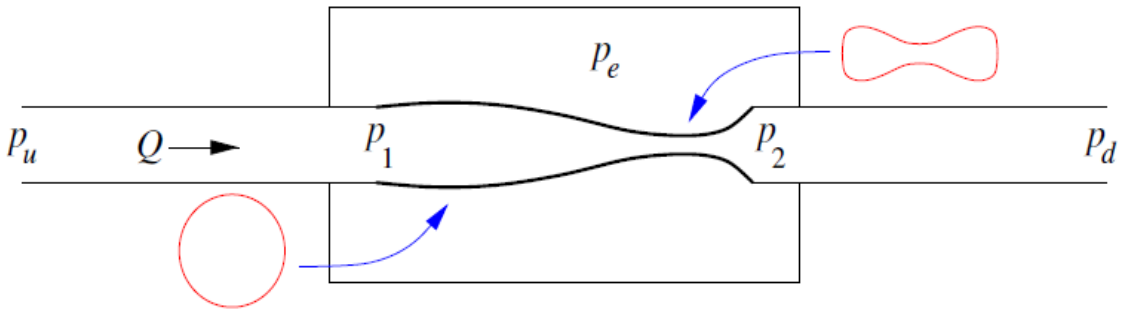

Figure 2-5 The Starling resistor to illustrate tube deformations (source: Jensen, 2013).

P_1 and P_2 are the upstream and downstream pressures respectively in the flexible tube which are controlled by valves in the rigid parts of the resistor. The pressure drops i.e. the difference between inlet and outlet pressures (P_u and P_d) respectively causes a fluid flux Q to be transported from left to right as shown in Figure 2-5. The flexible segment of the resistor can deform depending on the magnitude of the external pressure P_e in the chamber that encloses it. The principles of the Starling resistor will be adopted for the experiments of this research where P_e will be the wave induced pressures.

Chaplin et al. (2012) developed a laboratory model for the testing of the performance of a distensible tube which they named Anaconda. The diameter and the length of the tube were 250mm and 7m respectively. The tube was 1mm thick aligned with 4 inelastic fabrics. It was pressurised with water and made to float just below the water surface and aligned with the generated water waves. The wave induced external pressures on the tube created constrictions and bulges which travelled along the tube in the direction of the waves. The Anaconda was partially filled. However, in this research, the tubes will be filled to maintain positive pressure heads. The principles used in these experiments will the used to design the experiments of the present research.

2.6 Measuring particle flow fields

Although the overall flow rate of a fluid through a flexible tube can be measured simply as the volume collected per unit time, it does not give sufficient information about the

flow fields of the fluid particles. Particle tracking velocimetry (PTV) and particle image velocimetry (PIV) are useful techniques for obtaining flows fields of fluid particles. The main difference between PIV and PTV is they are based on Eulerian and Lagrangian motions respectively.

2.6.1 Eulerian and Lagrangian motion of particles in a fluid

The Eulerian motion refers to a motion of a fluid particle observed at a fixed point while Lagrangian motion is when the observer is moving with the fluid particle (see e.g. Dean and Dalrymple, 2010). Eulerian motion considers velocity, density, pressure and other physical quantities of a fluid as functions of position and time. For example, $u = u(x, t)$ is the velocity of a fluid at location x and time t while $\rho = \rho(x, t)$ is the fluid density at the same position x and time t (Phillips, 1977). The rate of change in the flow field is given by the partial derivatives of the physical quantities with respect to t and x (Phillips, 1977).

In a Lagrangian motion, a fluid particle is described by its position a at an initial time t_0, the motion to the next location and the velocity of the particle (Phillips, 1977). Lagrangian motion is described by:

$$x = x(a, t - t_0) \tag{2-10}$$

where,

$t - t_0$ is the time taken by a particle to move from initial position a to its final position x. The displacement $(x - a)$ of a fluid particle from initial position a to a final position x is then given by:

$$x - a = \int_{t_0}^{t} u(a, t - t_0)dt \tag{2-11}$$

where u is the velocity of the particle (Phillips, 1977).

2.6.2 PIV and PTV in particle flow measurements

To measure the velocity of fluid particles using either PIV or PTV, neutrally buoyant tracer particles are seeded in the fluid in a flexible tube. The velocities of the tracer particles must be approximately equal to the velocities of the fluid particles (Westerweel, 1997). Velocities of fluid particles are evaluated from image positions of particles (seeded in the fluid) at successive time instances (Umeyama et al. 2010). The velocity fields of the tracer particles are calculated from the displacement of the individual particles and the exposure time between the successive images.

The seeded particles are usually illuminated by laser light or light emitting diodes to make them more visible in the fluid. The particles should be able to scatter the light so that they can be traced separately (Feng, et al. 2011). In both PIV and PTV analysis, particles of a fluid trace a path-line. A path-line is defined as a time exposure showing the direction a fluid particle takes at successive time steps (Massey, 1983). When a particle moves from one position to another, it accelerates only if the velocities at the two positions are different (Massey, 1983). Cross-correlation refers to a technique for estimating the position of a particle in successive images (Cowen and Monismith, 1997; Umeyama et al. 2010). Unlike PIV, PTV can use more than two frames in the analysis to give tracks traced by particles. However, only two successive frames will be used in this research.

The particle density i.e. the number of particles per field of view must be limited to avoid ambiguity in the pairing process during cross-correlation (Cowen and Monismith, 1997). Both PTV and PIV give information about the flow only where the tracer particles are located (Westerweel, 1997). This means that an adequate number of particles must be seeded in the flow to obtain more accurate information about the fluid motion.

The raw images of the seeded particles usually contain a lot of unnecessary information hence there is need to threshold the images according to the pixel values of the particles in the images. The whole set of images is analysed to determine the minimum and maximum pixel values which will then be used to subtracted unnecessary information from the images (Cowen and Monismith, 1997). The aim being having images with only particles and a black background to make cross-correlation process easier.

The velocity v of a tracer particle is measured as displacement $D(X; t', t'')$ in a time interval defined as $\Delta t = t'' - t'$ (Westerweel, 1997). The displacement of the tracer particles is then given as follows:

$$D(X;\ t', t'') = \int_{t'}^{t''} v[X(t), t]dt \qquad (2\text{-}12)$$

where $v[X(t), t]$ is the tracer particle's velocity with respect to position X and time t (Westerweel, 1997).

If $v[X(t), t]$ is equal to the fluid's local velocity $u(X, t)$, then the particles can be referred to as ideal (Westerweel, 1997). In practice, this is usually not the case so the displacements of the tracer particles are just approximations of the actual flow fluids. Errors may occur from using this measurement technique. Random patterns produced by the tracer particles describe the fluid flow. A tracer pattern is described as follows:

$$G(X, t) = \sum_{i=1}^{N} \delta[X - X_i\,(t)] \qquad (2\text{-}13)$$

where

$X_i(t)$ is the position vector of the tracer particle at time *t*,

N is the number of tracer particles available in the field of view,

$\delta(X)$ is a Dirac function (Westerweel, 1997).

Geometric consistency is considered in determining every possible path a particle can take (Ohmi and Li, 2000). The path of all the neighbouring match-particles are considered but the path of the best-match particle is selected (Ohmi and Li, 2000). The displacement is extrapolated using iterations. An iterative method is also used to search neighbouring particles. The techniques are also based on the matching probability. Iterative probability is given as follows:

$$\sum_j P_{ij} + P_i^* = 1 \qquad (2\text{-}14)$$

where

P_{ij} is the probability that particles i and j in two successive frames match,

P_i^* is the probability a particle loses its match (Ohmi and Li, 2000).

It is common for a particle to lose its partner i.e. when the particle disappears from the field of view and when there are too many particles in the field of view. The loss of

particles during the tracking must be minimised by seeding only an adequate number of particles in the field of view.

2.7 Tracer particles for fluid flow measurements

As discussed earlier, for the seeded tracer particles to accurately describe the motion of the fluid particles, they should follow the fluid motion perfectly without changing the properties of the fluid or altering the flow in any way and they must not interact with each other (Westerweel, 1997). Ideal particles are neutrally buoyant i.e. their densities must be approximately the same as the density of the fluid in which they are seeded.

Settling velocities of particles in a static fluid are dependent on properties of both the particles and the fluid. These properties include the viscosity and density of the fluid, the shape, surface texture, density and size of the particles (Dietrich, 1982). The settling velocities can also depend on the concentration of the particles (Cheng, 1997). At a certain concentration, the particles begin to collide with each other so the number of particles must be limited.

In this research, settling velocities of particles will be measured in still water. The settling velocities of particles in still water differ from the settling velocities of the same particles in turbulent flows because of the bias due to the particle inertia (Wang and Maxey, 1993).

CHAPTER 3 : RESEARCH METHODOLOGY

The previous chapter contains relevant literature about flexible tubular photo-bioreactors (FTPBRs) for growing microalgae offshore and the techniques of measuring fluid particle velocities in flexible tubes. The experiments for this research were performed in a laboratory flume with the FTPBR influenced by simplified narrow-band ocean swell waves created by a piston wave generator. The detailed experimental procedures for these experiments will be discussed in the subsequent sections of this chapter in the following order:

1. *Testing the wave generator and the associated wave characteristics*
2. *Shape analysis of a flexible polyethylene tube in the simplified Ocean waves*
3. *Experiments on tracer particles (white, spherical polystyrene particles) to make them neutrally buoyant so that they follow the flow and can therefore be used to characterise*
4. *Application of particle tracking velocimetry (PTV) to measure the mean velocities and turbulence of fluid flow in the FTPBR.*

3.1 The piston wave generator and the wave characteristics

A rectangular wave tank made from transparent Plexiglas (or Perspex) with a height of 200 *mm*, a width of 170*mm* and a total length of 9*m* (consists of 3 sections of 3m each) filled to a water depth $h < 200$ *mm*. Periodic progressive waves were simulated by a wave generator consisting of an electric motor with a maximum rotational speed of 60 revolutions per second, a Plexiglas circular disk mounted to the electric motor and a piston paddle. The circular disk was connected to the paddle and mounted on a trolley by a metal bar (Figures 3-1 and 3-2) so that the circular disk rotated with the motor. The periodic linear strokes produced progressive waves in the wave flume. The radial attachment position on the circular disk could be varied to change the stroke length S of the paddle. Two pebble beaches were situated at both ends inside the wave tank to absorb the generated waves in order to minimise reflection of the incident waves.

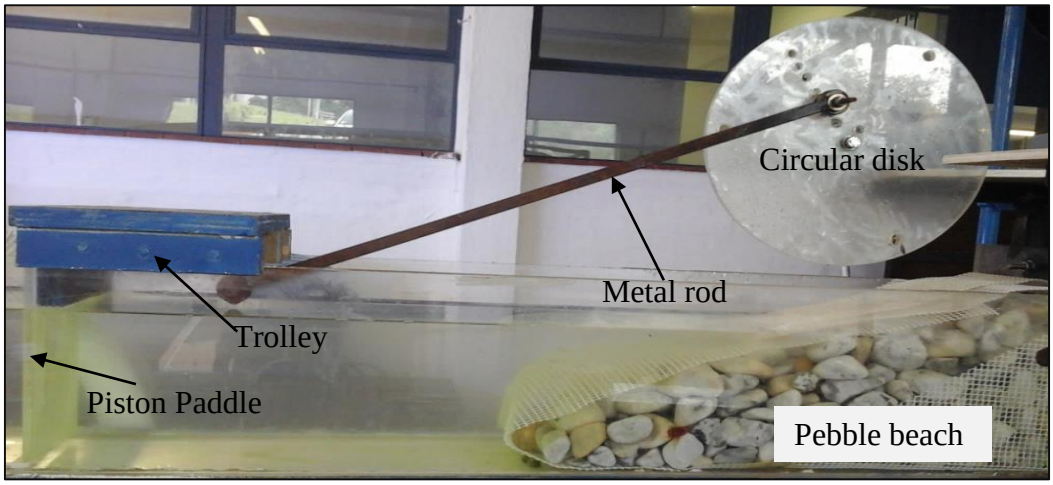

Figure 3-1 *The piston wave generator and a pebble beach to reduce reflection of waves and splashing of water in the wave flume.*

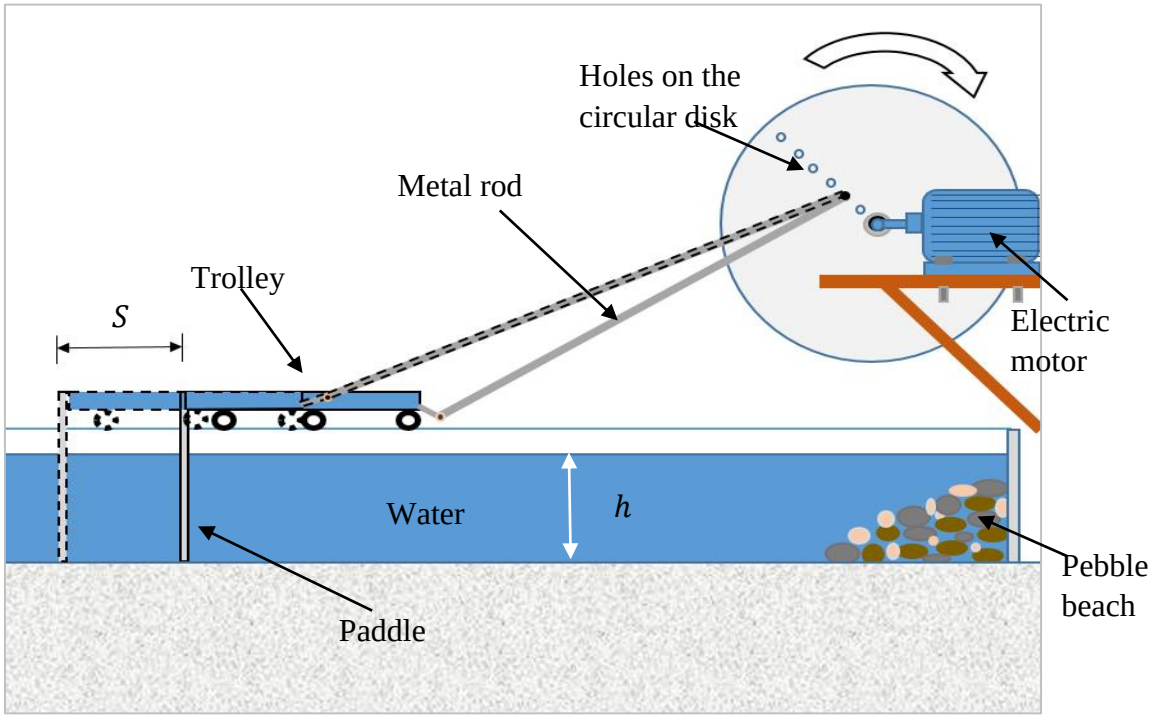

Figure 3-2 *Schematic of the piston wave generation equipment consisting of an electric motor, a circular disk connected to a trolley-mounted paddle by a metal rod. The holes on the disk allow the stroke length S of the wave paddle. The frequency of the waves could be varied by changing the rotational speed of the motor and disk.*

The still water depths h and the paddle stroke lengths S were measured manually. The wave lengths L and the wave heights H were measured from still images captured by a Nikon D7000 digital camera.

A schematic representation of the full set of the wave generation experiment is shown in Figure 3-3.

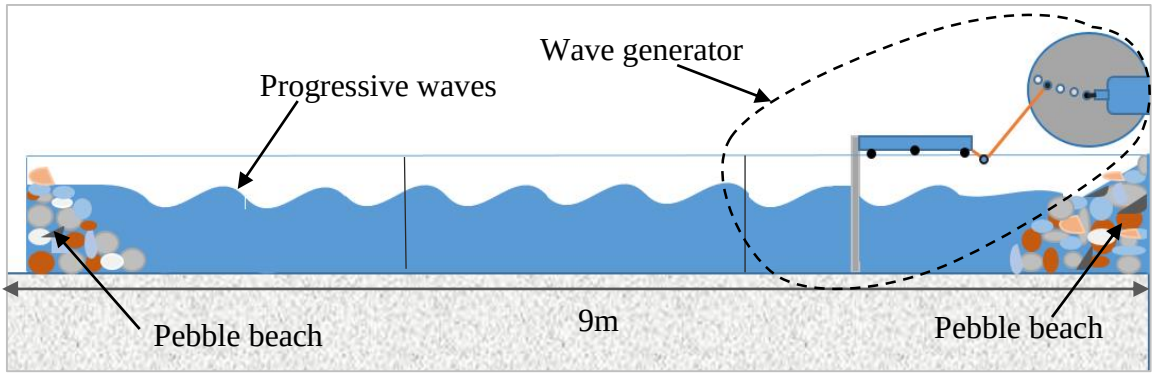

Figure 3-3 A schematic representation of the full set of the piston wave generation equipment showing the electric motor, the paddle, the wave tank with water and the beaches at both ends of the tank

The effects of wave parameters such as the water depth h, frequency f as well as piston paddle stroke S on the generated waves were investigated independently. The volume of water in the flume displaced is dependent on S. The wave generator was tested for its consistency with shallow water wave theory (Biesel and Suquet, 1951) and the results were compared to the results summarised by Dean and Dalrymple, 2010.

3.2 Shape analysis of the flexible, floating tubes in water waves

This section gives experimental procedures used in the present research to measure the deformations of a polyethylene flexible tube in wave tank. The tube deformations are 3 dimensional. The effects of wave parameters such as wave frequency f, wave height H and the still water depth h as well as the stroke S, the tube's elevation relative to the free surface of the waves and the tube's internal pressure head Δp on the tube deformation were investigated independently. The effects of the tube on the progressive waves were also investigated.

The pressure head Δp was defined as the difference between still water levels (SWL) in the wave flume and that in the reservoirs. A schematic representation of the set-up of these experiments is shown in Figure 3-4. This research focused on positive pressure heads i.e. when the SWL of the reservoirs $>$ the SWL of the wave tank. The spill/overflow tube in the reservoir acted as a one-way valve.

The waves were generated as described in the previous section. A transparent polyethylene flexible tube was clamped at both ends to hold it in position as shown in Figure 3-4. The tube had a diameter D of 30mm and a total length of 6.25m.

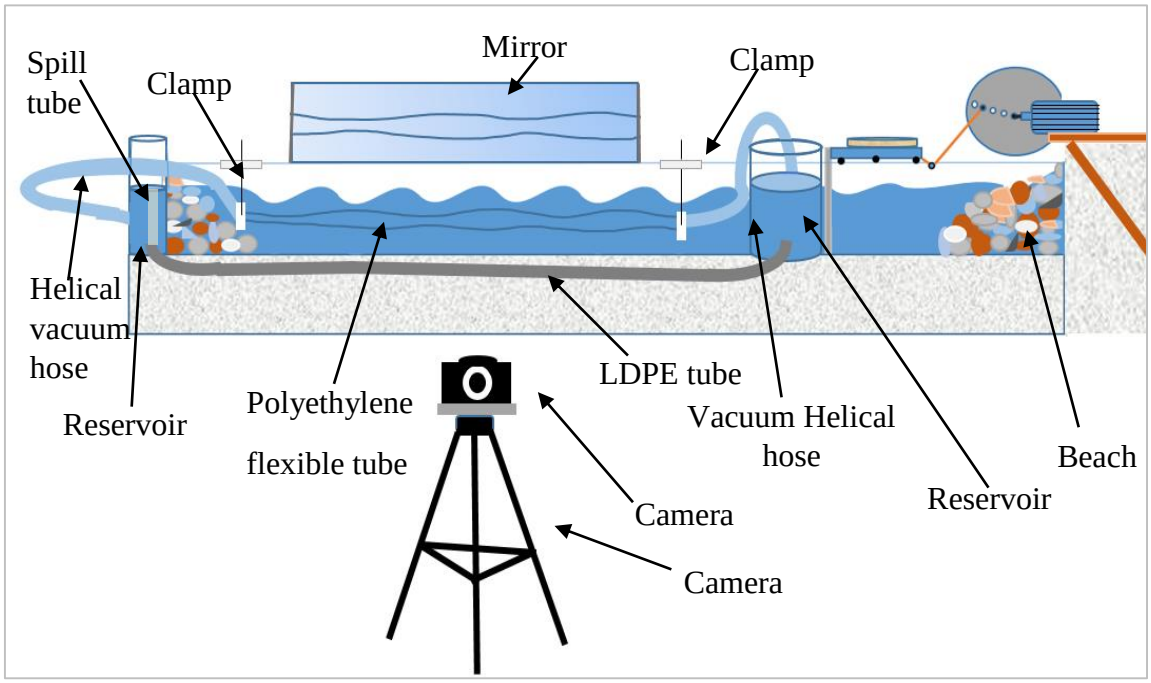

Figure 3-4 A sketch drawing of the full set of equipment (or system) used for the shape analysis of the flexible tube in water waves.

Two helical vacuum hoses were connected to the two ends of the flexible tube. The advantages of using the helical hoses are that they can bend without changing their diameter and that they are rigid enough for the purpose of this experiment. Figure 3-5 shows one of the helical vacuum hoses used for the experiments.

Two cylindrical reservoirs of diameters 90mm and 180mm and height of 300mm were connected to each other by a transparent low-density polyethylene (LDPE) tube with a diameter of 32mm and to the flexible tube by the helical vacuum hoses. A mirror was

tilted at an angle of 45° to project an image of the top (plan) view of the flexible tube. Without the mirror, only the side view of the flexible tube could be observed.

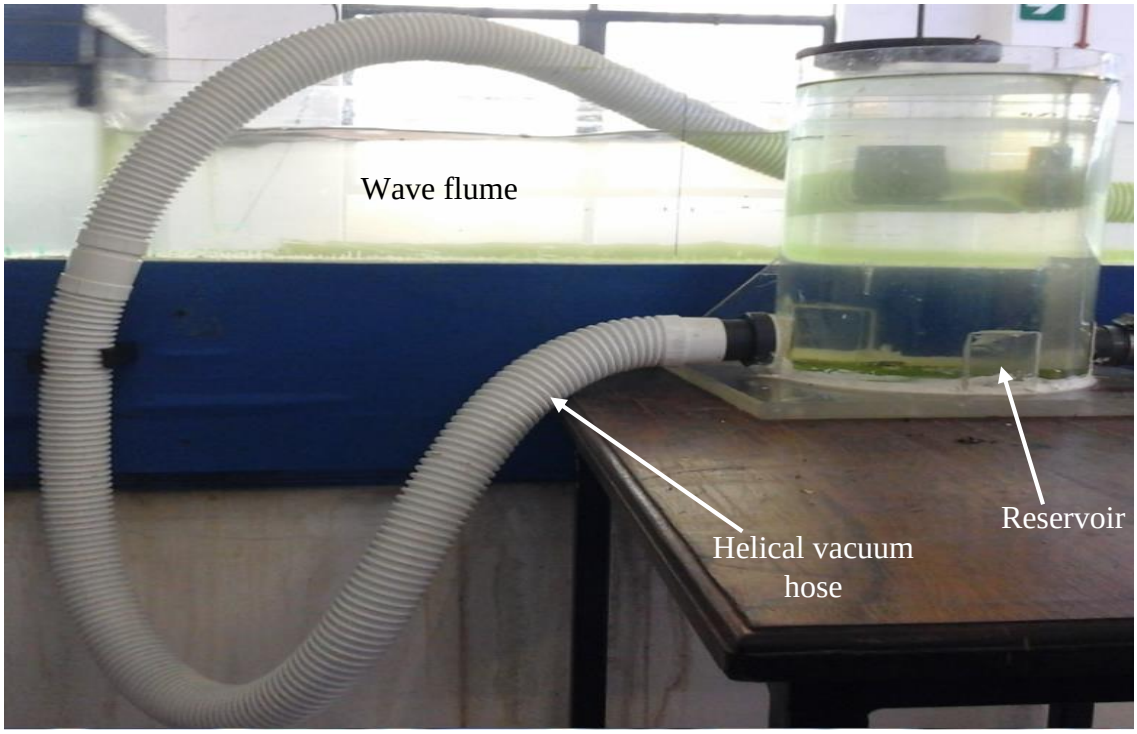

Figure 3-5 The rigid helical hose with ends connected to a reservoir and the flexible tube for the shape analysis experiments.

A Nikon digital camera was used to record videos of the tube deformations under various wave characteristics. The camera was mounted on a tripod stand in order to avoid blurred images in case the camera shakes (see e.g. Tellen et al. 2007).

All air bubbles were removed from the pipe system before running the experiments. The tube deformations were measured as the ratio of tube's instantaneous horizontal and vertical dimensions to the undeformed diameter D i.e. D_y/D and D_Z/D.

D_y and D_z are the vertical and horizontal cross-sectional dimensions of an approximate ellipse. The tube becomes circular in shape when both D_y and D_z are equal to D. Figure 3-6 is a schematic representation of the cross-section of a flexible tube showing the vertical and horizontal dimensions D_y and D_z respectively.

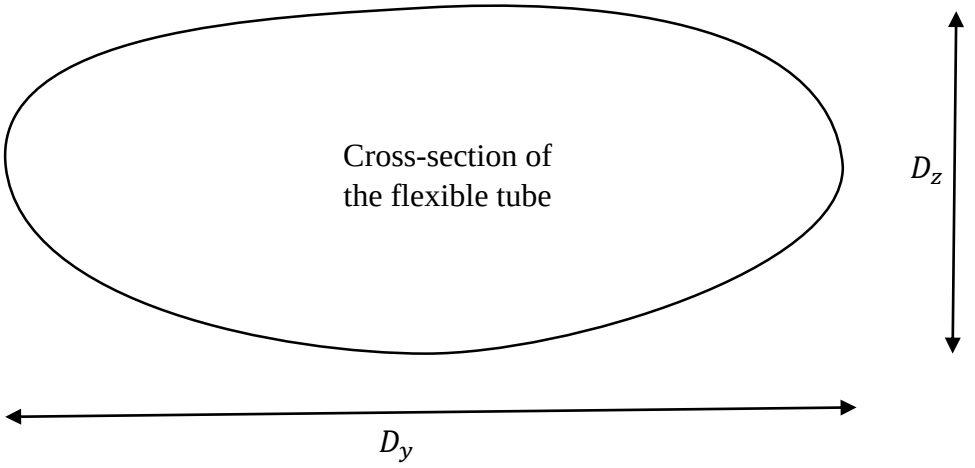

Figure 3-6 A schematic representation of the cross-section of a flexible tube showing the vertical and horizontal dimensions D_y and D_z respectively.

The vertical dimensions D_y were measured from still image frames converted from recorded videos. The dimensions D_z could not be measured directly from the mirror without introducing errors due to refraction effects of the waves in the wave tank so they were inferred by assuming an ellipsoidal deformed shape and applying Sykora's formula for the conserved perimeter as:

$$S(a,b) = 4\,\frac{\mu ab+(a-b)^2}{a+b} + \lambda\frac{ab}{a+b}\left[\frac{(a-b)^2}{(a+b)^2+\pi ab}\right] \qquad (3\text{-}1)$$

where

$\lambda = -\frac{1}{2}$, $\mu = \pi$,

$a = D_z$, $b = D_y$,

$S(a,b)$ is the perimeter of an ellipse with dimensions a and b as shown in Figure 3-7.

If the tube remains inextensible, then the perimeter of an ellipse remains constant when a flexible tube is deformed even though its cross-sectional area changes. If one of the dimensions a or b is known, the other dimension can be calculated using the formula. For this research, the Sykora's formula was used to approximate dimension D_z.

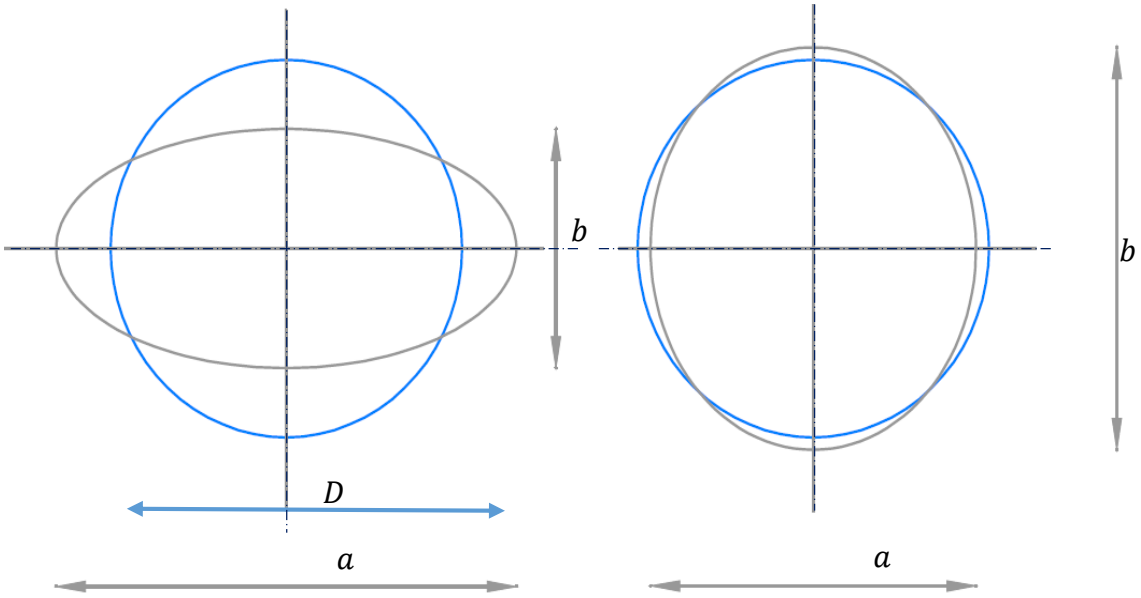

Figure 3-7 *A schematic representation of vertical and horizontal dimensions a and b used in the Sykora's formula where* $a = D_Z$, $b = D_y$ *and D is the diameter of the undistorted circular tube. The dashed lines are centre lines of the cross-sections.*

The deformations can also be measured in terms of area changes (A/A_c) where A and A_c are the instantaneous and circular cross-sectional areas respectively.

All videos of these experiments were recorded at 24 frames per second (fps) at varying shutter speeds. Each video file was converted into successive image frames using Matlab software.

Figure 3-8 shows an image frame extracted from one of the recorded videos by the software. The image shows the wave profile, the flexible tube filled with water coloured with a blue dye to improve its visibility and measuring tapes. The waves were propagating from right to left. A wave crest was taken as a reference travelling point with x being any distance measured from a stationary starting point (Eulerian motion) to the crest. The wave moves a distance Δx i.e. $L/(the\ number\ of\ frames\ in\ 1\ wavelength)$ in every successive image frame.

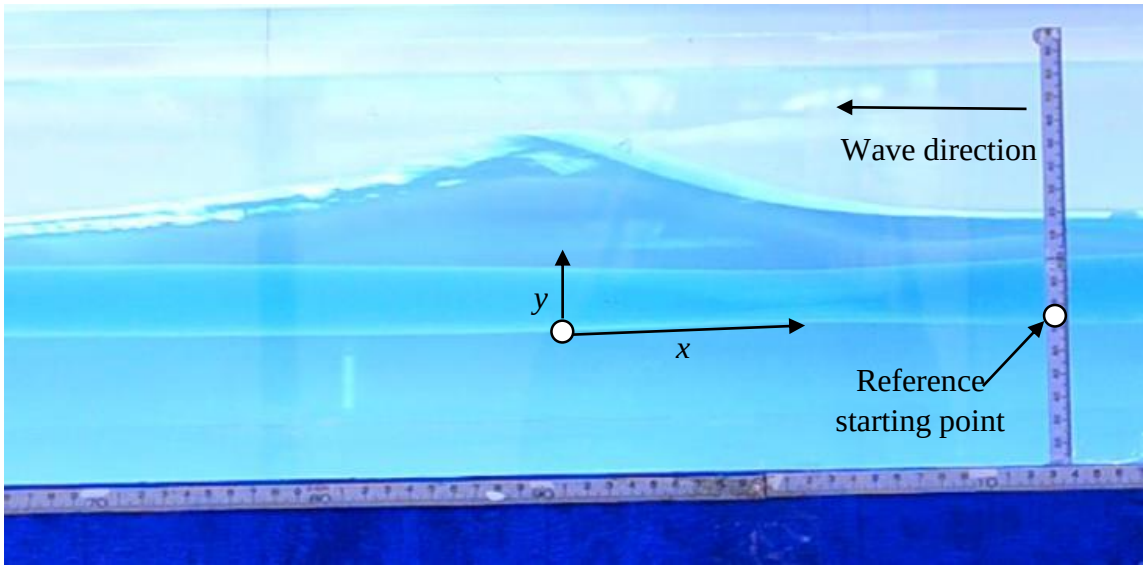

Figure 3-8 *An image frame converted from a video file using Matlab. Vertical tube deformations D_y were measured with reference to the wave crest for each time step. The waves were progressing from right to left.*

3.3 Measuring the average flow rate of the water through flexible tube

The wave frequency f, wave height H, stroke S, internal pressure head Δp, the still water depth h and the tube level relative to the free surface of the waves have effects on the generated waves as well as the flow rates through the system. This section gives the method that was used to measure the associated flow rates for the tube deformations.

The equipment used for measuring flow rates is the same as used for the shape analysis experiments. Figure 3-9 is a schematic representation of the one end of the wave flume showing the helical hose and a clear LDPE tube connected to a reservoir. A clear LDPE spill tube worked as a one-way valve and is vital in monitoring pressure heads when measuring flow rates. A valve on the LDPE tube was used to control the flow of water from the reservoir. The average flow rates were measured by (1) shutting the valve first, (2) withdrawing fluid from the reservoir, (3) measuring the time taken to refill the reservoir and (4) calculating the flow rate as the volume removed over time taken to replace the volume.

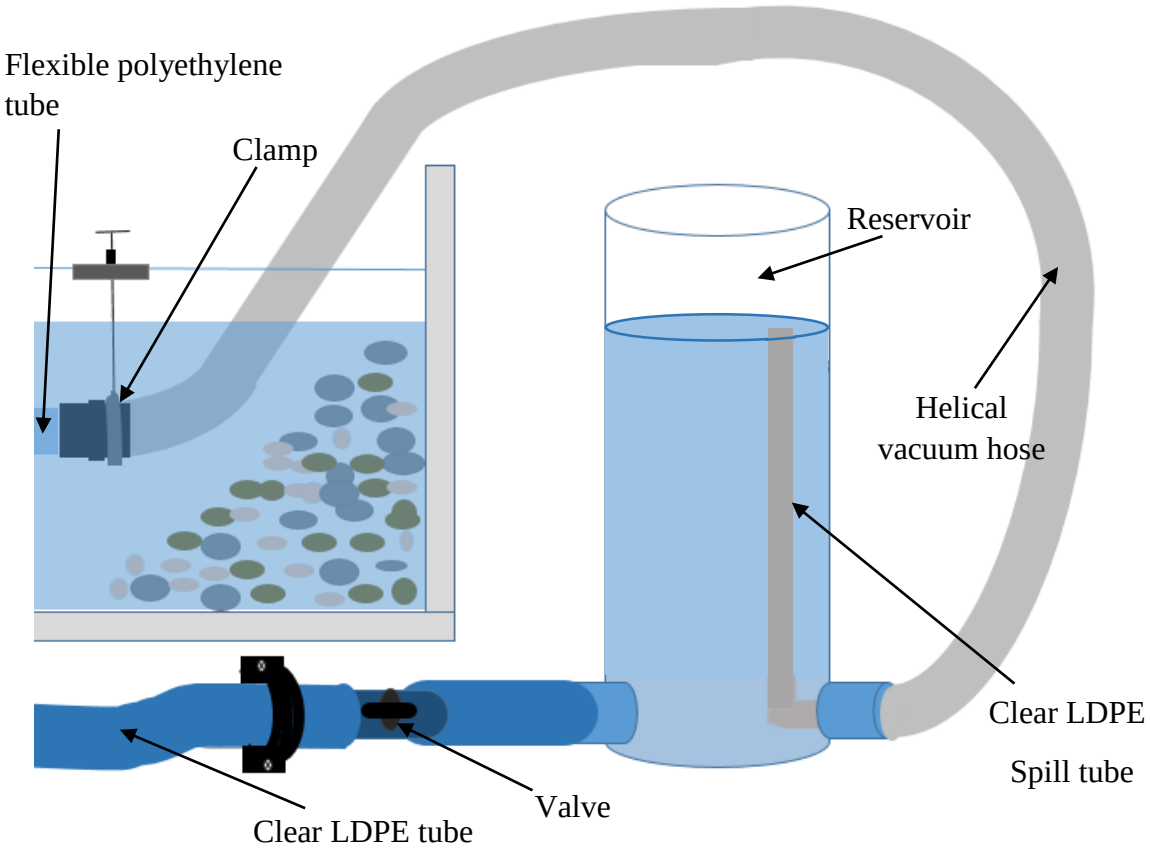

Figure 3-9 *The equipment for measuring the flow rate of the fluid through the system influenced by progressive waves. The tanks and the pipes continue in the left direction.*

3.4 Particle analysis

The previous section describes how overall flow rates of the water through the flexible tube were measured but average flows do not give much information about the fluid particle motion. The flow of the water in the flexible tubes under the influence of progressive waves of area change is peristaltic. The peristaltic flow can be analysed from the motion of neutrally buoyant spherical polystyrene particles seeded in the fluid. This section gives a method of preparing the polystyrene particles to make them neutrally buoyant so that they follow the flow and can therefore be used to characterise the flow fields in the flexible tube.

The diameters of the polystyrene particles were measured using a computer software (NIS-elements) and a Nikon inverted microscope system. The diameters of random 25 particles are shown in Table A-1 in the Appendix. The inverted microscope system has a camera which captures images at frame rates of choice and exporting them to the NIS-elements software in real time for analysis and storage. The mass of an adequate known number the polystyrene particles was measured using a digital scale. The average mass of 1 particle was then deduced from the total mass of particles. The densities of the particles were then calculated. The densities of the particles were compared to the density of water. The settling velocities of particles in still water were calculated. The particles were expanded by heating them in a water bath for a certain period of time to increase their volumes and by so doing reducing their densities until they had acceptable settling velocities.

3.5 Particle motion analysis using PTV

The overall flow rates of water in the flexible tube do not give much details about the motion of the individual water particles. The main objective of this experiment was to obtain the velocity fields of water particles in the flexible tubes. Simplified narrow-band ocean waves were simulated in a laboratory wave flume. The motion of neutrally buoyant polystyrene particles was recorded by a video camera from a fixed point for PTV analysis. This is an example of Eulerian motion where the velocities of fluid particles are measured by an observer from a fixed point (see e.g. Dean and Dalrymple, 2010). To increase their visibility in water, the particles were illuminated by 50 Kilo-Watt florescent lamps.

A Matlab code was used to convert the recorded video files into successive image frames suitable for the PTV analysis. Naming of the images was important in case there was a need to refer to a certain image frame. The images were named in their successive order, each having an image number and an extension ‘jpg’ e.g. the first image was named img001.jpg, the second img002.jpg etc.

The default size of each image frame was 1920 x1080 pixels. The location of a particle in an image is given by its pixel value in the form of (x, y) coordinates, for example, the top left corner of each image has the coordinates (0, 0) while the bottom, right corner has the coordinates (1920, 1080).

Figure 3-10 is an image of particles in a flexible tube produced by the Matlab showing the pixel information of a particular point in the image. The pixel information consists of the coordinates as well as the red, green and blue values of that particular pixel.

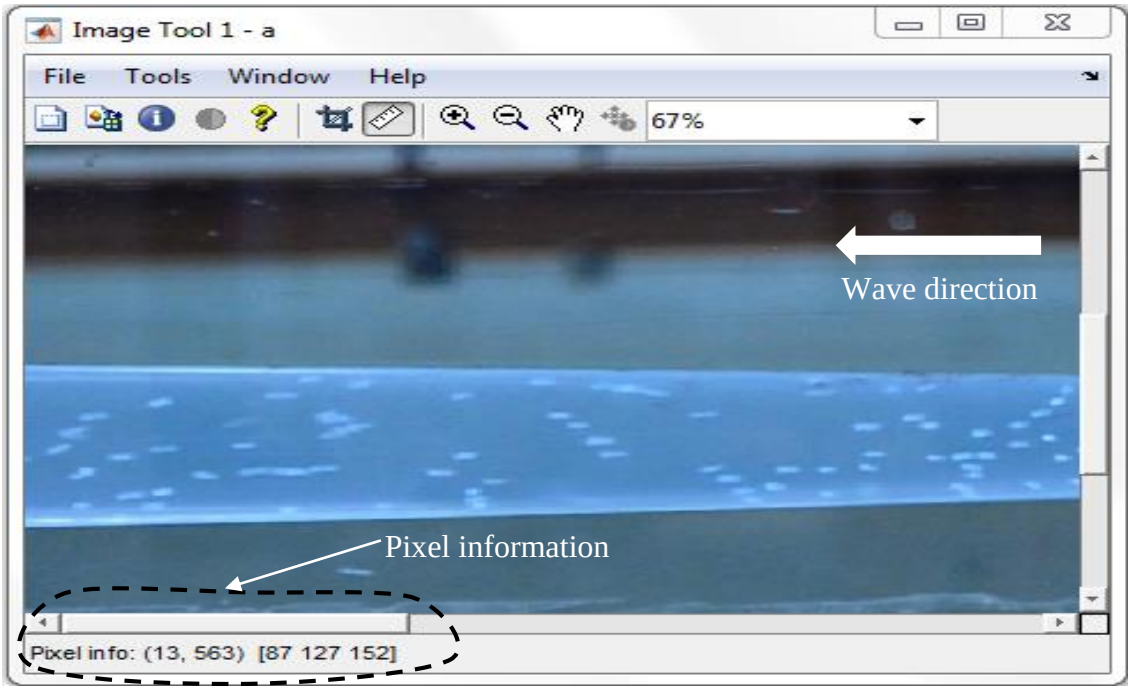

Figure 3-10 An image showing pixel information of a point in the image. (13, 563) are the (x, y) coordinates of the point while [87 127 152] are its red, green and blue pixel values.

Two successive image frames are used to track the motion of the individual particles. The displacement of each particle was calculated from the pixel coordinates of the particle in successive frames. A particle can be lost during tracking i.e. when it goes out of the field of view of the successive image. A pattern is usually noticed when a group of particles is moving together as shown in Figure 3-11. This helps in the manual tracking of the individual particles in successive images. The images can be zoomed to get the accurate pixel values of the particles.

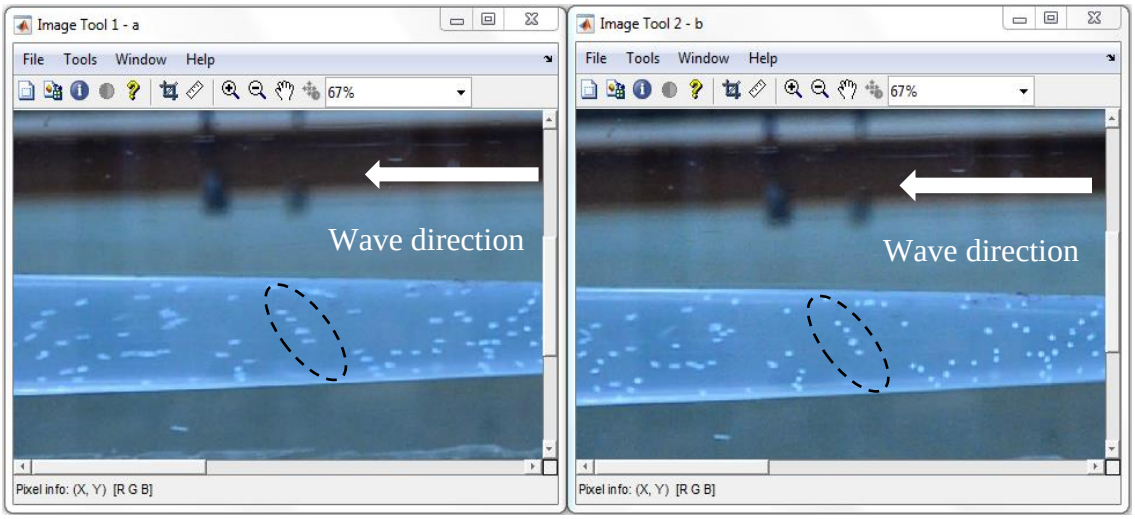

Figure 3-11 Two successive images used for tracking particle motion. The particles enclosed in the dashed ellipses in the left frame are the same particles in the right frame.

The velocities of particles were measured in two components, the horizontal and vertical components. The displacements of the particles in pixel coordinates were then calculated as follows:

$x_2 - x_1$ or $y_2 - y_1$

where

x_1 and x_2 are the initial and final particle's horizontal coordinates respectively while y_1 and y_2 are the initial and final vertical coordinates respectively in two successive image frames. A coordinate system was established such that when $x_2 - x_1 > 1$, then the particle is moving in the direction of the waves and opposite the wave direction when $x_2 - x_1 < 1$. A particle is stationary when $x_2 - x_1 = 0$. For vertical displacements, when $y_2 - y_1 > 0$, the particle is moving upwards. A downward motion is when $y_2 - y_1 < 0$. There is no change in vertical displacement when $y_2 - y_1 = 0$.

The length of the tube equal to one wavelength was segmented in 14 control volumes as depicted in Figure 3-12. A sample of at least 90 particles was analysed in each control volume. The control volumes were of different sizes because the particles motions/flow fields varied distinctly along the tube so more attention was given to turbulent zones.

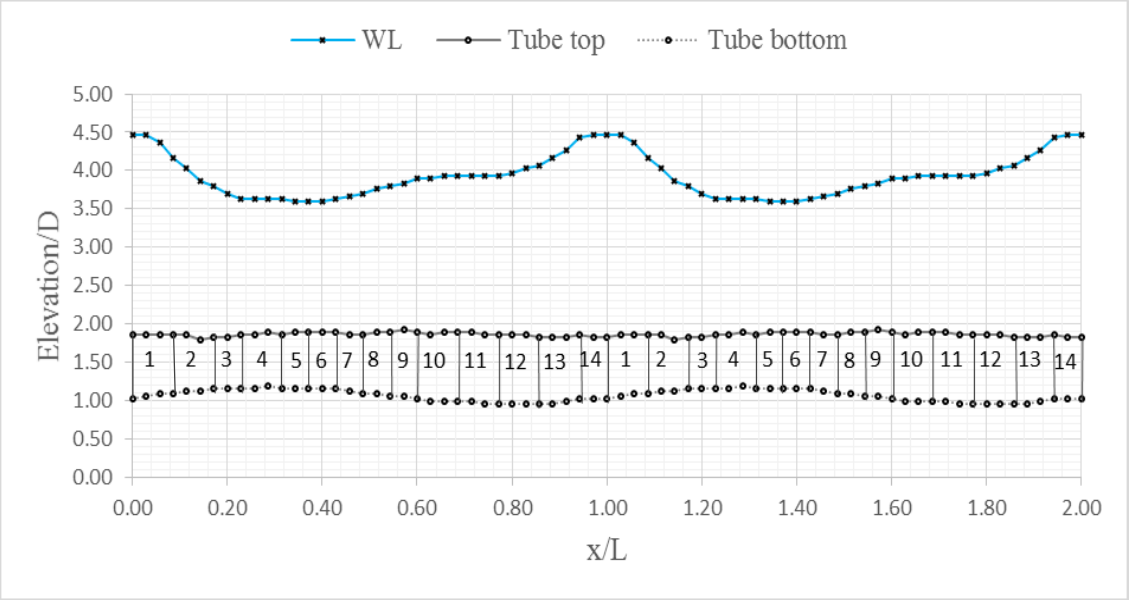

Figure 3-12 An image showing the 14 control volumes used for the average particles velocities analysis along 2 wavelengths of the flexible, floating tube being acted upon by progressive waves produced in a wave flume. Waves moving right to left.

The local velocities of the individual polystyrene particles and the average velocity of the particles in each control volume were calculated. The vector fields of the polystyrene particles together with the standard deviations, Reynolds stresses and the histograms of velocities of the particles in each control volume will be presented in the next chapter.

CHAPTER 4 : RESULTS AND DISCUSSION

The previous chapter is the methodology on how the experiments for this research were conducted. The results from the experiments are presented in this chapter together with discussion of the findings.

The experiments performed were the following:

1. *Testing the wave generator and the associated wave characteristics*
2. *Measuring average flow rates through flexible tubes deployed in progressive water waves*
3. *Shape analysis of the polyethylene flexible tube in simplified narrow branded, water waves created by a piston wave generator in a wave flume*
4. *Preparing tracer particles to make them neutrally buoyant so that they follow the flow and can therefore be used to characterise the flow field in the FTPBR*
5. *Particle tracking velocimetry (PTV) to obtain the particles' mean velocities and turbulence of the flow in the FTPBR*

4.1 Testing the wave generator

Since most of the experiments of this research were performed using a paddle-type piston wave generator, it was necessary to test if it was 'fit for purpose'. The wave generator was used to simulate simplified (narrow-band) ocean swell waves by varying the frequency f, the paddle stroke S and the water depth h. S and h have the most effect on the wave height H which depends strongly on the volume of fluid displaced by the piston paddle (see e.g. Dean and Dalrymple, 2010). As discussed earlier, this was first reviewed by Biesel and Suquet (1951). The summarised results are in Dean Dalrymple (2010).

The present experimental results of the wave generator were compared with previous results summarized by Dean and Dalrymple (2010) who showed that the ratio (H/S) / $K_p h$ (where the wave number $K_p = 2\pi/L$ with L the wavelength) is approximately equal to 1 for shallow water waves. The results of the present experiments are presented in Figure

4-1 whereas the results summarised by Dean and Dalrymple (2010) are shown in Figure 4-2.

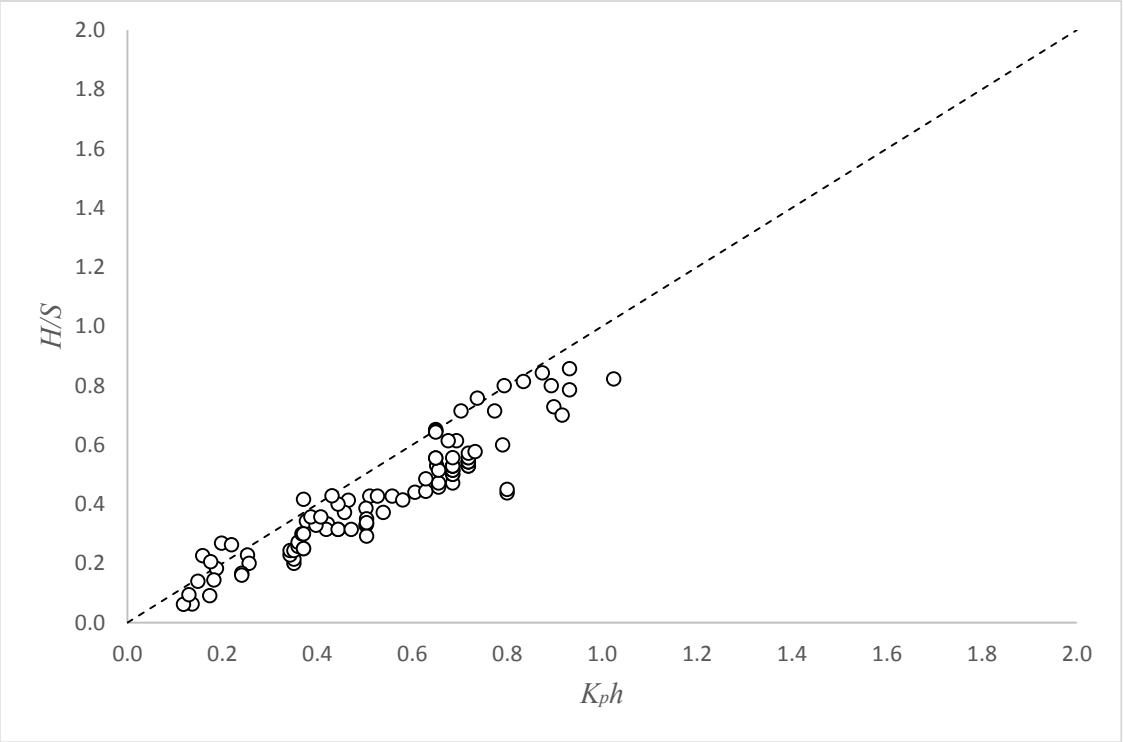

Figure 4-1 *The relationship between H/S and $K_p h$ for the generated water waves for the piston wave generator for the present experiments. The straight line is a linear relationship with a slope of 1 as suggested by Biesel and Suquet (1951).*

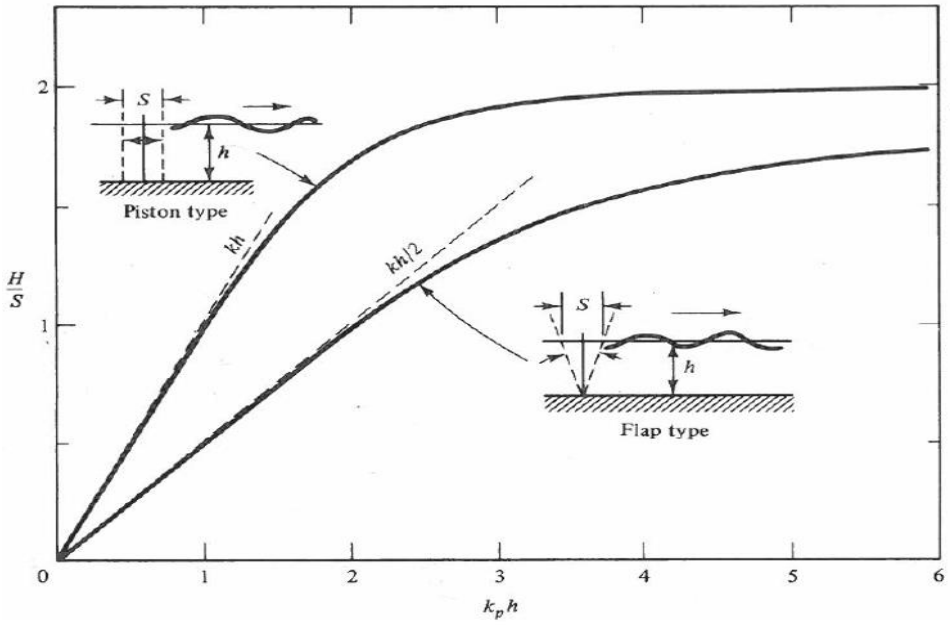

Figure 4-2 The relationship between H/S and $K_p h$ summarised by Dean and Dalrymple (2010) from Biesel and Suquet (1951). The straight lines show linear relationships for shallow water waves.

The ratios *(H/S)* / $K_p h$ for a piston type wave generator were below 1 for most of the data points due to leakages of water around the sides and the bottom of the piston paddle as suggested by Madsen (1970). Since $\frac{H}{S} = \frac{4sinh^2 kh}{\sinh 2kh + 2kh}$ (see e.g. Hughes, 1993), the piston stroke length for a given wave with known wave height and $K_p h$ can be calculated. The *H/S* and $K_p h$ for the present experiments (Figure 4-1) were limited to 1.2 due to the limitations in the available wave generator and the depth of the wave flume. The maximum frequency f of the wave generator was 1Hz and to produce a wider range of *H/S* and $K_p h$ needed a generator with maximum frequency $>$ 1Hz. The main focus was on shallow to intermediate water waves since it is cheaper to deploy the FTPBR systems in this regime which is also closer to the shore rather than in deep water waves. It is evident from Figure 4-1 that there is a linear relationship between *H/S* and $K_p h$ so the present results are consistent with the results in Dean and Dalrymple (2010). Besides the errors in measurements, the wave generator performed well and was considered 'fit for purpose' and consistent with the shallow water wave theory.

The independent variables for this experiment are the water depth *h*, wave frequency *f* and the paddle stroke *S.* The results of the experiment show that wave height *H* increases with water depth *h.* Figure 4-3 is a non-dimensional plot of *h/L* versus *H/L* when the

piston stroke S and the frequency f were kept constant. The data points are joined by a line for clarity.

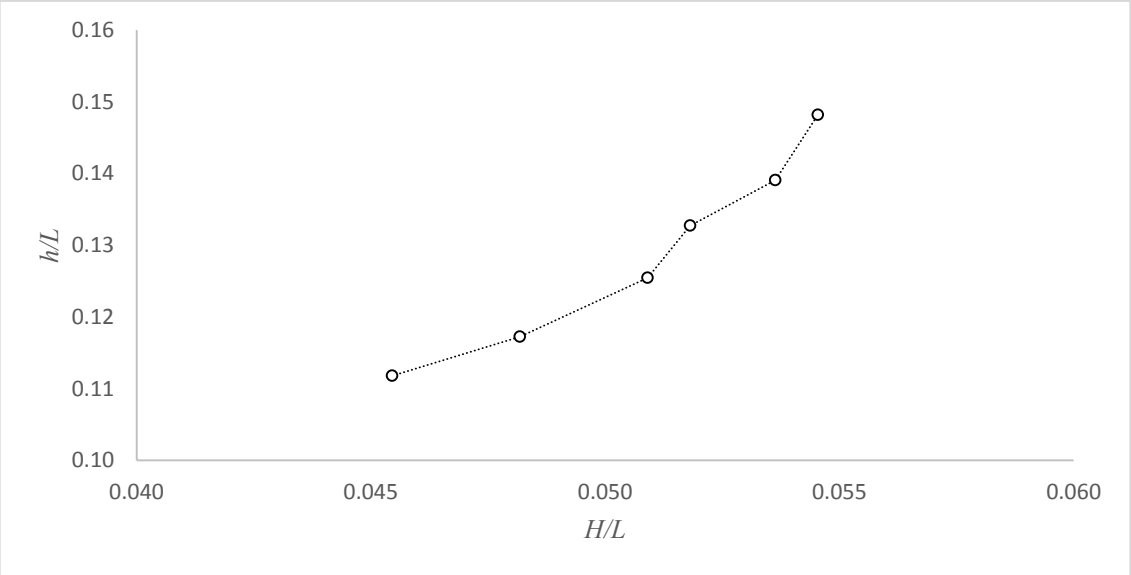

Figure 4-3 The relationship between water depth h and wave height H for the generated waves non-dimensionalised by the wavelengths L.

The wavelength L and frequency f of the waves are inversely proportional since $c = fL$ where c is the wave celerity. The wave height H is mainly affected by the paddle stroke S. Increasing S while keeping the frequency f and water depth h constant results in an increase in H as shown in Figure 4-4. This is derived from the Biesel and Suquet (1951) shallow water wave theory.

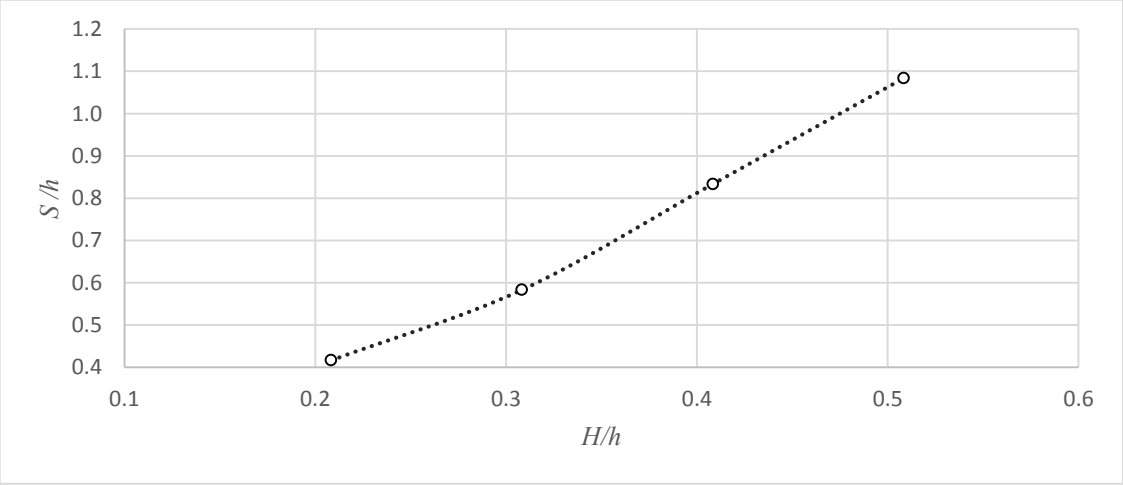

Figure 4-4 The wave generator stroke S versus wavelength H non-dimensionalised by water depth h. The dotted lines joining the data points for clarity.

The wave generator created both sinusoidal and cnoidal waves depending on the frequency f and the water depth h of progressive waves in the flume. Cnoidal waves occur when water depth h is less than a tenth of the wavelength L (Wiegel, 1959). Sinusoidal waves have troughs equal to crests while cnoidal waves have troughs shallower and longer than the crests. Sinusoidal waves have amplitude = 0.5 H but amplitude varies for cnoidal waves since they have longer and shallower troughs as compared to their crests. The energy of the wave is proportional to the square of its amplitude (see e.g. Dean and Dalrymple, 2010).

Waves create repetitive vertical as well as horizontal (oscillatory) motion of the water particles (Chappell, 1969). The influence of the waves on the water particles decreases as water depth increases. Waves are often classified according to their L/h and H/L ratios. These ratios are useful in establishing geometric comparisons between the laboratory waves and the naturally occurring ocean waves. Water waves tend to be shallow when $L/h \geq 20$ (see e.g. Chappell, 1969). However, waves do not suddenly become shallow when $L/h = 20$ but it is a gradual process where the limiting conditions become more accurate towards this value so a large number of the waves for the present experiments are close to following the shallow water wave theory. Figure 4-5 shows the *L/h* ratios for the generated waves obtained while testing the performance of the wave generator.

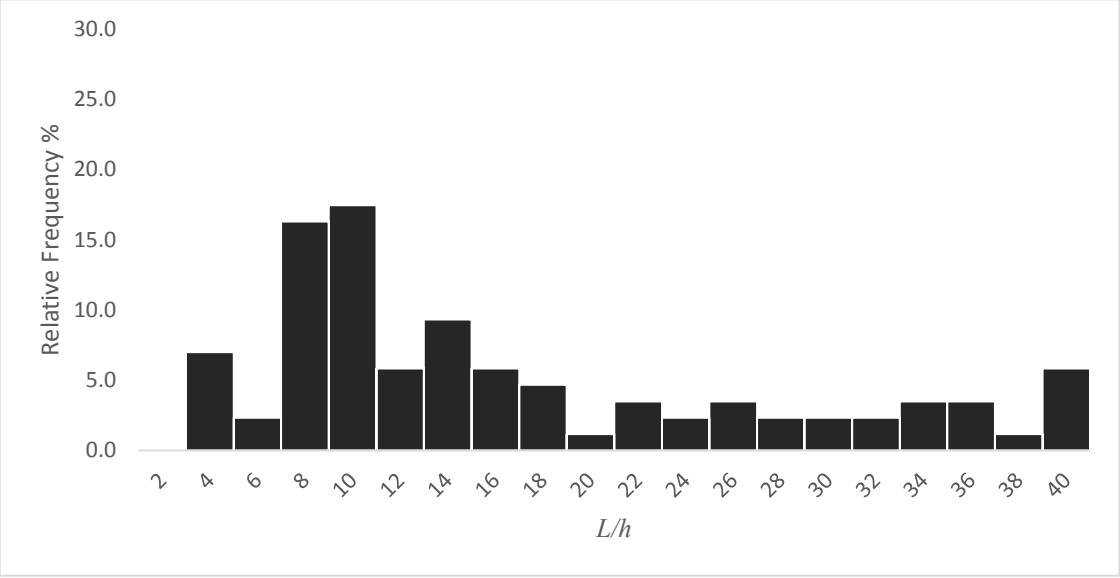

Figure 4-5 L/h and frequency of the waves produced in the wave tank while testing the performance of the wave generator.

The celerity c ($c = fL$) of a wave is an important property of waves and for shallow water waves is approximated by $c = \sqrt{gh}$, where g is the gravitational acceleration and h is the still water depth (Chappell, 1969). The relative celerities of the waves produced in the wave flume are shown in Figure 4-6 ranging from 0.86 to 1.25 with most waves having celerity between 1.0 and 1.1. The histogram shows relative frequencies (occurance) of $c/\sqrt{gh}$ for the present experiments. The water depth h is the main factor affecting celerity for shallow water waves. The wave tank had a maximum depth h of 200mm but it was only filled up to a water depth of 170mm to avoid splashing of the water out of the tank. This limited the range of celerities and waveform of the generated waves.

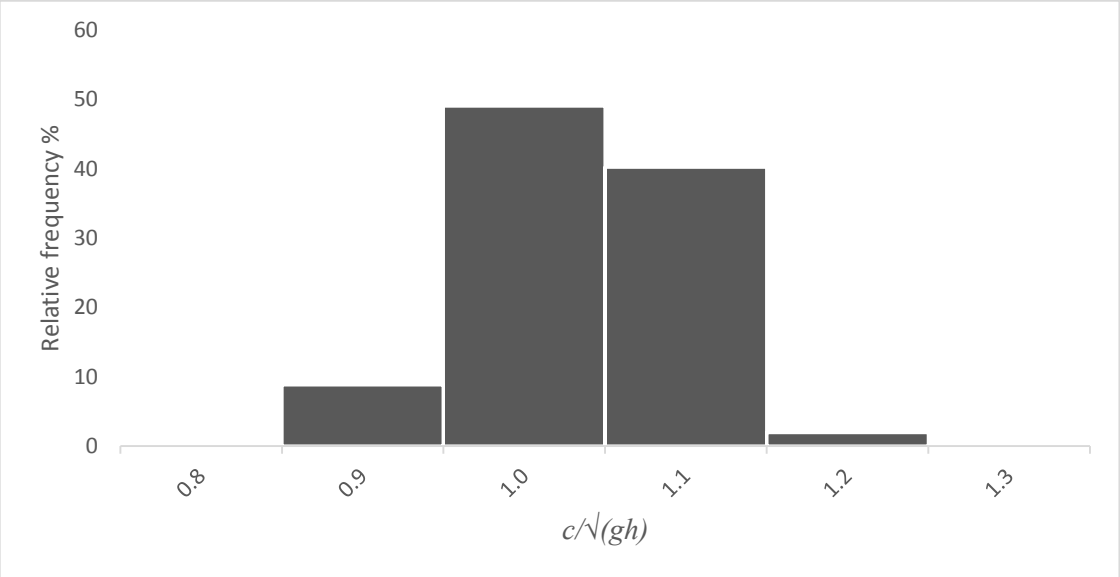

Figure 4-6 The relative celerities of the waves produced in the wave tank and their frequencies measured while testing the performance of the wave generator.

This section has presented information about the waves generated in the wave flume for the present experiments. It also indicates the limitations of the wave generator such as frequency f. However, experiments showed that the wave generator was 'fit for purpose' and consistent with the shallow water wave theory. The characteristics of the waves together with their effects on flexible tubes will be discussed in the subsequent sections of this chapter.

4.2 Effects of flexible tubes on waves

The presence of flexible tubes in water waves has an effect on the generated waves. Two experiments were performed, one in which a flexible tube filled with water was deployed in the wave tank and the other one without the tube. The wave characteristics were kept constant for the two experiments. The interference of the flexible tube with the progressive waves had an effect on the wave height resulting in wave-energy losses.

The wave heights along the flume were measured at 15 cm intervals. The wave energy for the experiment with the tube reduced from 100 % to 8.6 % as shown in Figure 4-7. The wave energy decreased to 81.3% for the experiment without the tube. Even though there was attenuation of waves in both experiments, it was more significant when the tube was in the flume. The interaction of the waves with the walls of the flume also contributed to the attenuation of waves. The flume was made up of 3 segments with rough joints therefore causing energy losses which resulted in further reduction of wave heights. If the walls of the wave flume were far apart, the wall friction was going to be of lesser effect.

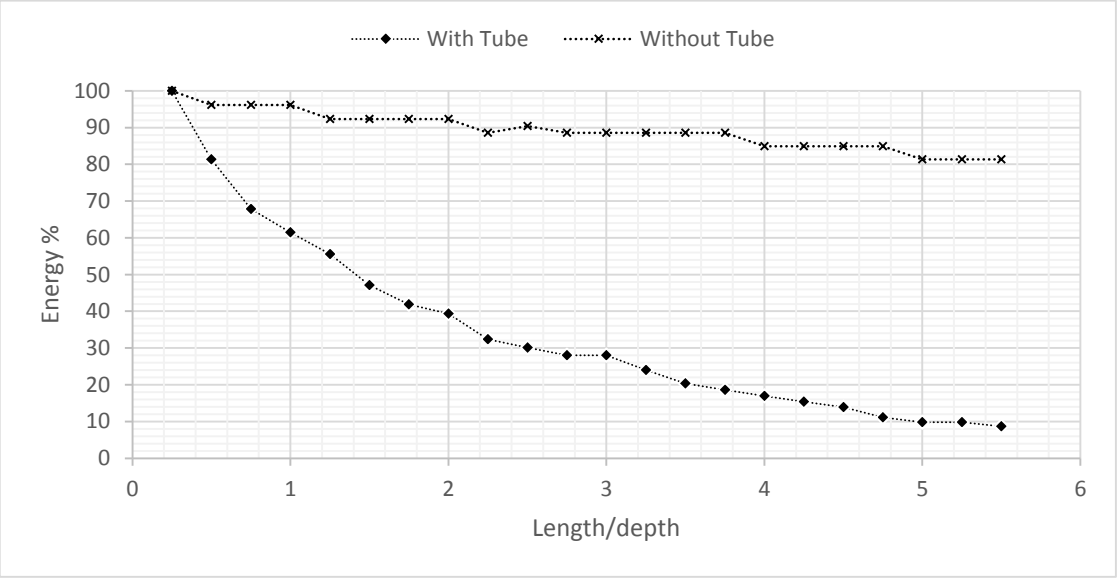

Figure 4-7 Wave energy losses due to the damping effect of the flexible tube on the wave height along the wave tank.

The attenuation of the waves due to the interference of the tube with the waves is expected to reduce with increase in tube's vertical distance from the free surface of the waves since the influence of the waves decreases with increase in water depth.

4.3 Effects of wave characteristics, internal pressure and tube position on the flow rates

The flow rates of water through the FTPBR depend on the geometric distortions of the flexible tube as discussed in the previous section. The flow rates vary with changes in wave parameters such as wave height as well as internal pressure in the tubes and the tube position relative to the surface of the waves. The effects of these parameters are discussed in the subsequent sub-sections.

4.3.1 Effect of wave height and frequency on the flow rates

Progressive waves deform flexible tubes while driving a flow of water through the tube. The flow rate through the flexible tube is mainly affected by wave heights of the progressive waves. The effect of wave frequency on the flow rates will also be discussed in this subsection. As discussed earlier, the wave energy E is directly proportional to the square of its displacement i.e. $E \propto A^2$ where A is the amplitude of the waves (Kane and Sternheim, 1983; Dean and Dalrymple, 2010). Since $A \propto H$, the wave energy E is related to its wave height H as follows:

$$E \propto kH^2 \qquad (4\text{-}1)$$

where k is a constant of proportionality. As discussed in Chapter 2, progressive waves in the wave flume create dynamic pressures along a flexible tube which deform it in a manner analogous to the peristalsis of substances in vascular systems in the human body. Both dynamic and hydrostatic pressures increase with wave height /amplitude. This will be discussed in section 4.4. Three experiments were conducted to investigate how the flow rates are affected by wave heights and frequencies of progressive waves. In the first experiment, the wave frequency f was varied while keeping the wave stroke S and water depth h constant. However, wave frequency has an effect on the wave height i.e. wave height increases with frequency as shown in Figure 4-8. The main aim of the second and third experiments was to keep either f or H constant while varying either of the two e.g. f was kept at 0.8 Hz while changing H by varying the wave stroke S. The flow rate increased even though the frequency was constant. However, keeping H constant while

varying frequency has little effect on the flow rates. The effects of frequency on the wave heights must also be considered.

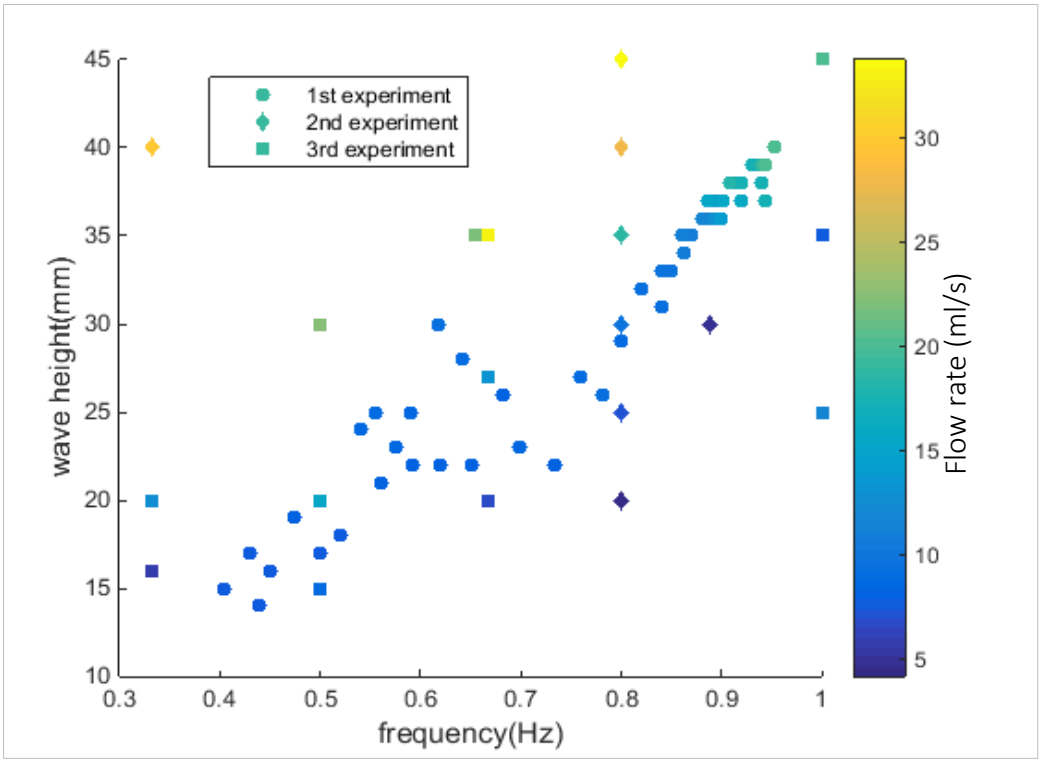

Figure 4-8 Results of the relationship between wave height and frequency and their effects on flow rates.

For shallow water waves, the wave celerity $c \approx \sqrt{gh}$ which is constant for a constant water depth h and also $c = fL$ where L is wave length so increasing f reduces L but the celerity remains the same. Lower frequencies produce larger pulses of flow whereas higher frequencies produce smaller but more pulses of flow in the same time τ at constant H. In other words, approximately the same volume of water is pumped at constant H and time τ but the size of the pulses depends on the wave frequency.

Flow rate increased gradually for wave heights up to 33*mm* then exponentially afterwards. This is when H becomes significantly greater than the tube diameter (i.e. $D = 30mm$). Figure 4-9 is a plot of flow rates against *H/D*.

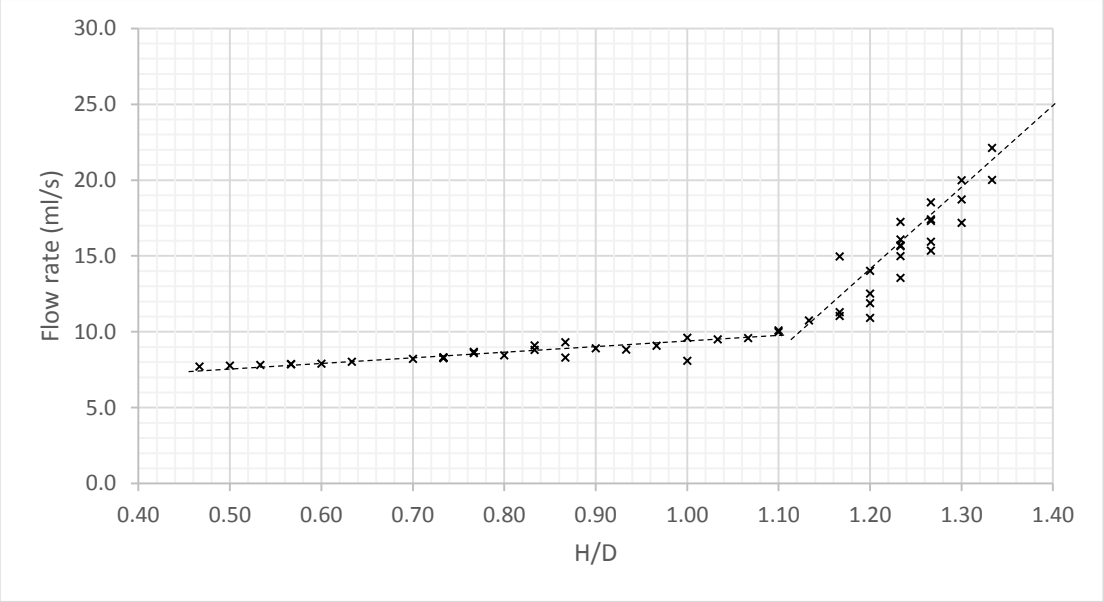

Figure 4-9 Flow rate versus H/D where H is the wave height and D is the tube diameter. The straight lines distinguish the gradual increase from a rapid increase in flow rate.

The wave heights for the experiments were mainly controlled by the stroke length *S*. Figure 4-10 shows that the wave height and flow rate increase with *S*. The increase in wave height due to increase in stroke length *S* has been presented earlier in section 4.1.

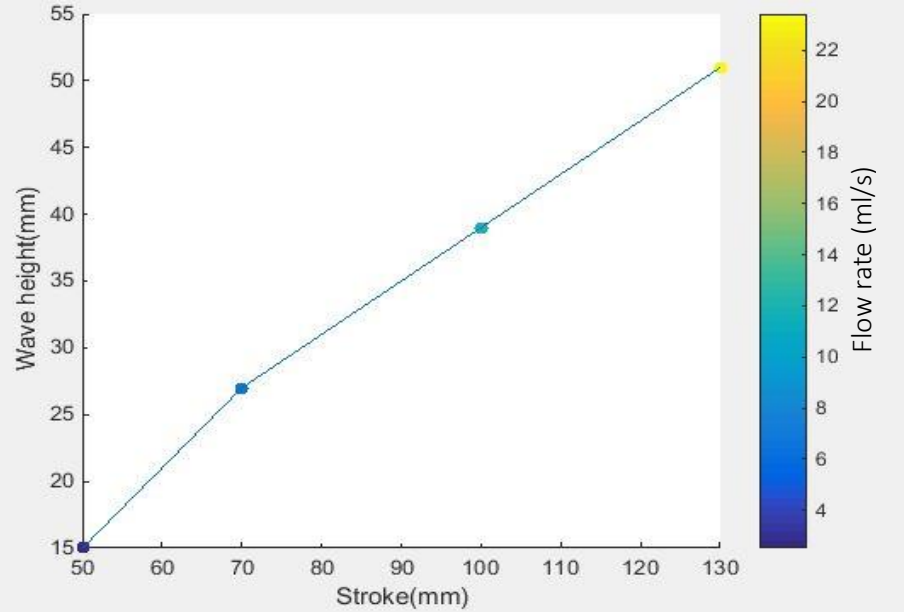

Figure 4-10 Effect of stroke length on the wave height and flow rate

4.3.2 Effects of pressure on the flow rate

This section discusses the effects of tube's internal pressure Δp on the flow rates. This research focuses only on positive pressure heads which are more stable to work with rather than negative pressure heads. Figure 4-11 shows that flow rate decreases with increase in internal pressure head. The initial pressure head Δp was $0mm$ and the external pressures were kept constant. There was a gradual decrease in flow rate as Δp was increased from $0mm$ to $+8mm$. A significant reduction in flow rate occurred beyond $\Delta p = +8mm$ until $\Delta p = +12mm$. This is when the tube's internal pressure became significantly larger than the external pressures. As the pressure head was increased, it became harder for external pressures to deform the flexible tube which resulted in lower flow rates through the tube. Further increase in Δp will eventually result in no flow through the tube.

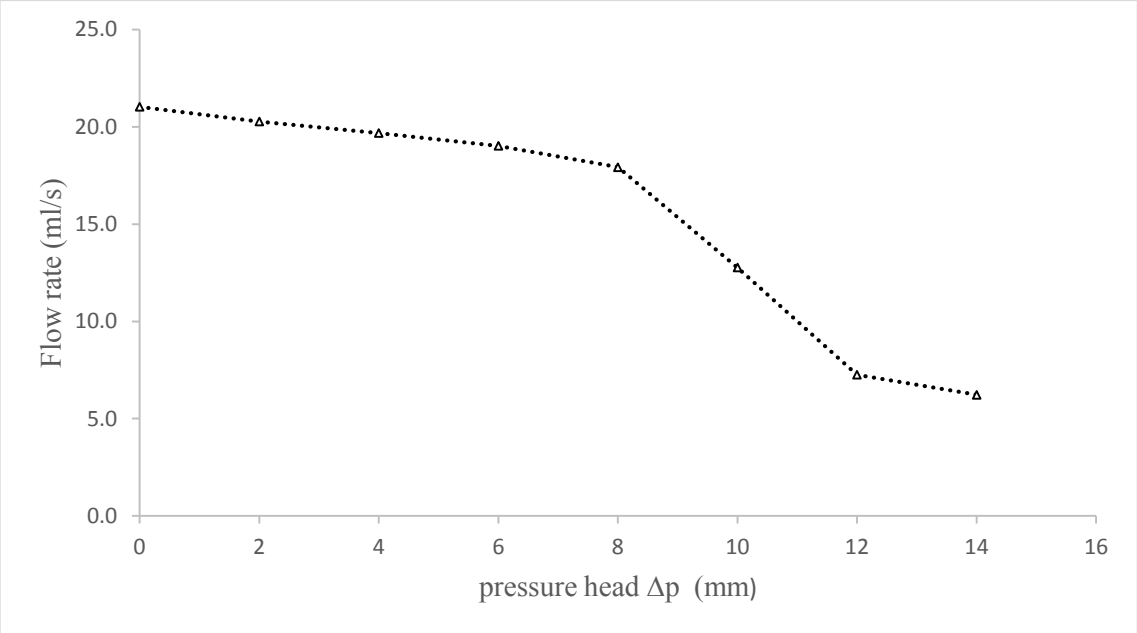

Figure 4-11 The effect of internal pressure head on the average flow rate of the water through the flexible tube. The data points are joined by straight lines for clarity.

4.3.3 Effects of the tube position on the flow rate

The effects of the tube's position relative to the free surface of the waves on the flow rates are discussed in this sub-section. The results of the experiments are presented in Figure 4-12.

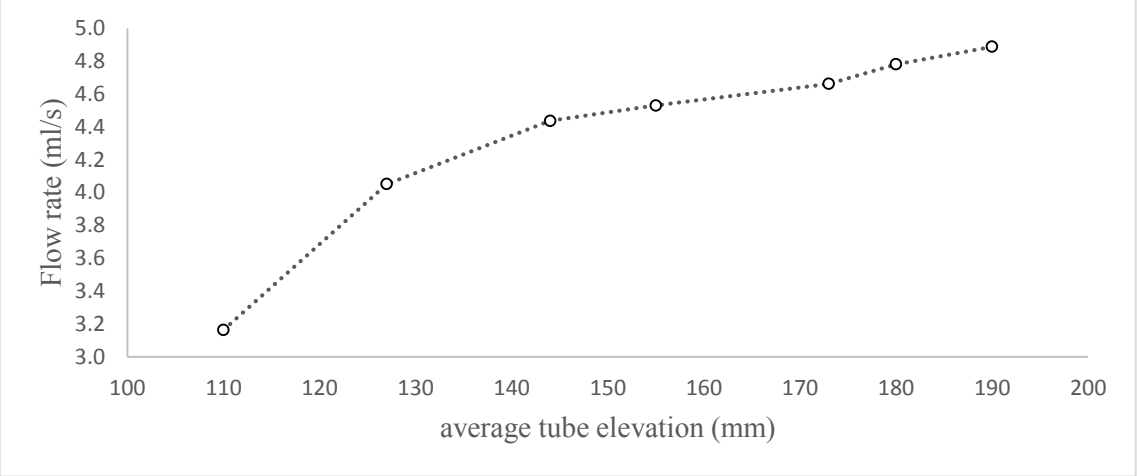

Figure 4-12 The effects of the tube elevation from the surface of the waves on the flow rates. The data points are joined by straight lines for clarity.

Flow rates increase with tube's position from the surface of the waves. This is because the total pressure (dynamic + hydrostatic) increases with water depth h. There is a limit to this effect since the influence of the waves reduces with increases in h. Most importantly, the choice of depth of the tubes must be done considering that microalgae cells need sunlight for photosynthesis. The intensity of sunlight is maximum at the surface of the waves and reduces with increase in water depth h.

4.4 Geometric distortion of the flexible tube by progressive waves

4.4.1 Introduction to the distortion of the flexible tubes by progressive waves

In this section, the effects of wave parameters such as frequency and wave height as well as the tube position (elevation) relative to the free surface of waves and the internal pressure of the flexible tube containing water on the geometric distortion of the tube will

be presented. These parameters affect the deformation of flexible tubes containing water, hence their effects are important in this research. The flow rate of the water in the tube is dependent on the rate and magnitudes of these deformations.

It is important to note that the tubes were not deformed when there were no waves propagating in the flume. When a flexible tube containing a fluid is deployed in a wave tank, the wave-induced pressures deform it non-uniformly along its length. The wave-induced pressures increase with wave height so the pressures under a wave crest are greater than the pressures under troughs (see e.g. Dean and Dalrymple, 2010) as discussed in chapter 2. Dynamic pressures are created due to the propagation of the waves. The wave-induced pressure perturbations also decay with depth below the free surface (see e.g. Chappell, 1969) but this was not verified since the depth of the wave flume was limited to 200*mm*.

Since there are internal and external pressures acting on the tube, the tube is deformed when the internal pressures of water in the tube are less than the external wave-induced pressures (see e.g. Jensen, 2013). The higher the external pressure on the tube, the greater the tube distortions. The water in the flexible tube has inertia and has to be moved to allow the tube to deform. The points of maximum deformations were not directly below the crests but lagged behind the crests of the propagating waves as shown in Figure 4-13. The deformations travelled along the flume at the same celerity as the waves. Although two wavelengths are shown, only one wavelength was analysed and the second one is a duplicate of the other.

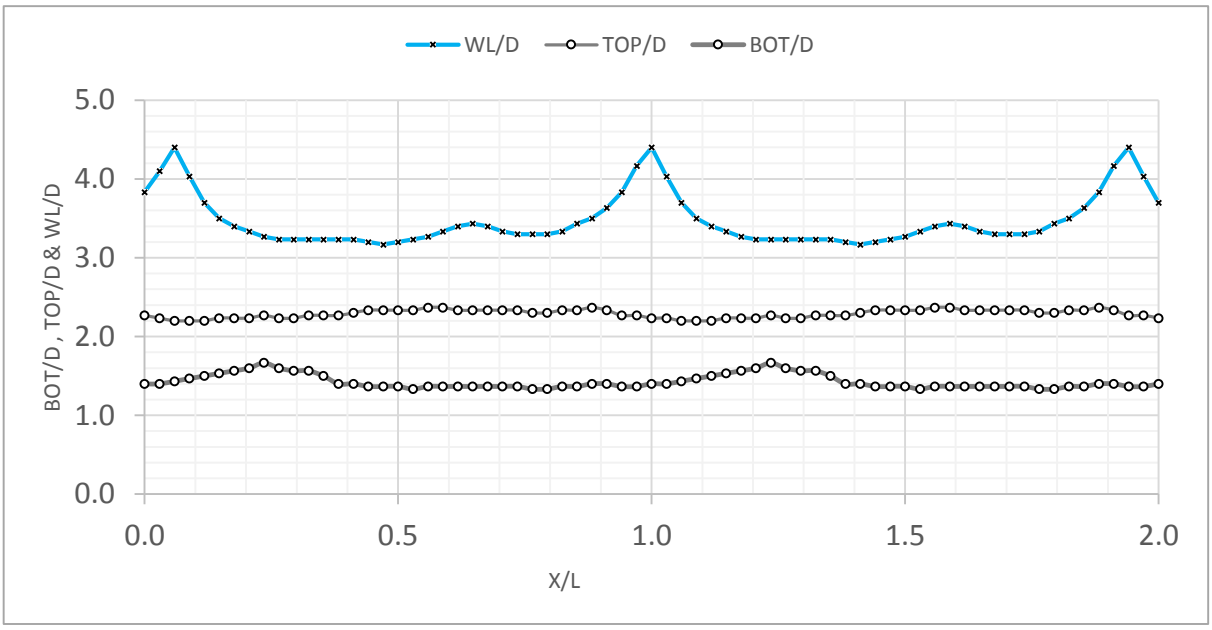

Figure 4-13 Non-dimensionalised tube deformations (TOP/D and BOT/D) with respect to water levels (WL/D) for a progressive cnoidal wave. D is the diameter of the undistorted tube and TOP and BOT are the tube's top and bottom elevations respectively. The waves were moving right to left.

The tube deformations were measured as ratios D_Y/D and D_z/D as described in the research methodology. D_Y/D is a measure of deformations in the vertical direction while D_z/D is for horizontal deformations. The tube is not deformed when the two ratios are equal to each other i.e. when $D_Y/D = D_z/D = 1$. This occurs on the 'no deformation line' (NDL) when the cross-section of the flexible tube is circular in shape (see Figure 4-14). Where deformations occur, the cross-section of the tube changes from circular to elliptical (or a non-circular shape).

Figure 4-14 shows the tube deformations at a frequency of $0.95Hz$ and internal pressure head of $0mm$. The deformations shown are for a portion of the tube with length equal to $2L$.

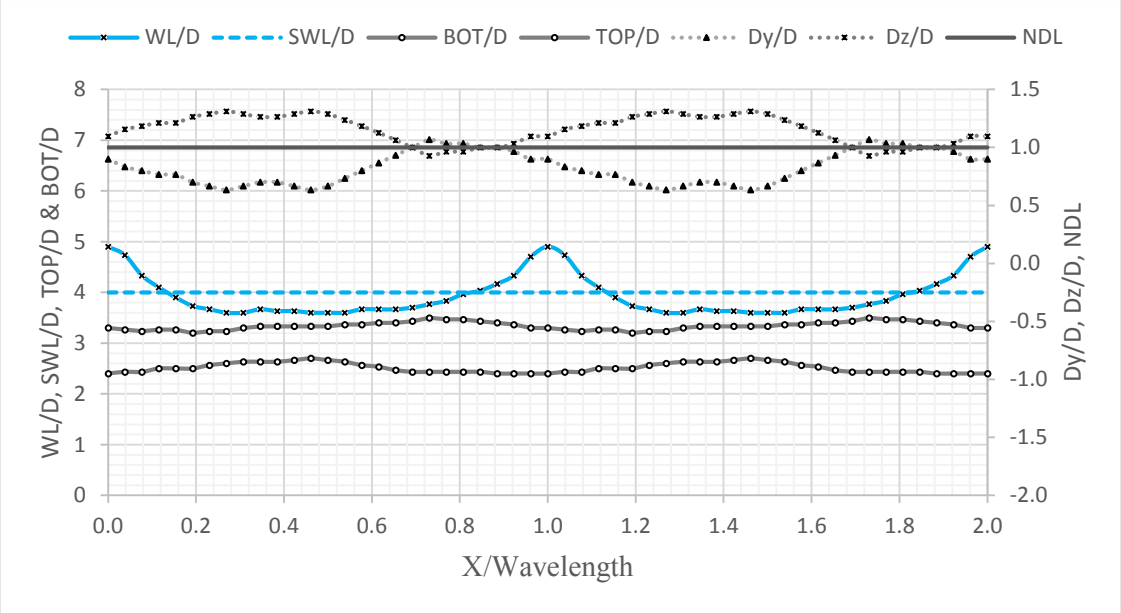

Figure 4-14 Tube deformation along the flume as the ratios D_y/D and D_z/D for vertical and horizontal deformations respectively at a frequency of 0.95Hz, wave height of 39mm and pressure head of 0mm. SWL and NDL are the 'still water level' and 'no deformation line' respectively. BOT/D and TOP/D are the relative bottom and top elevations respectively. Waves were moving right to left.

D_y/D and D_z/D are symmetrical about the NDL. The tube deformed more in the vertical direction than in the horizontal direction since the D_y/D ratio along the tube was less than D_z/D most of the times. This suggests that the deformations are mainly due to the wave- induced pressures on the tube acting in the vertical direction.

The measurements of D_y were obtained from still images as described in the methodology. Measuring D_z manually resulted in errors due to the refraction effects of waves so D_z had to be inferred from D_y on the assumption of an elliptical shaped distortion using the Sykora's formula as described in the previous chapter. The formula assumes that the perimeter of the tube's cross-section remains constant when cross-sectional areas change when the tube is deformed.

The deformations were also measured in terms of relative area changes A/A_c as shown in Figure 4-15 where A is the instantaneous cross-sectional area of the tube at any point x/L while A_c is the circular cross-sectional area of the tube with diameter D. A_c is also the maximum cross-sectional area of the tube since the tube was inextensible. The tube is

deformed whenever A/A_c is less than 100%. These deformations are analogous to peristalsis in vascular systems in the human body. The peristaltic flow arises from progressive waves of area change travelling within the flexible tube (see e.g. Muthu et al. 2001). The waves were moving right to left.

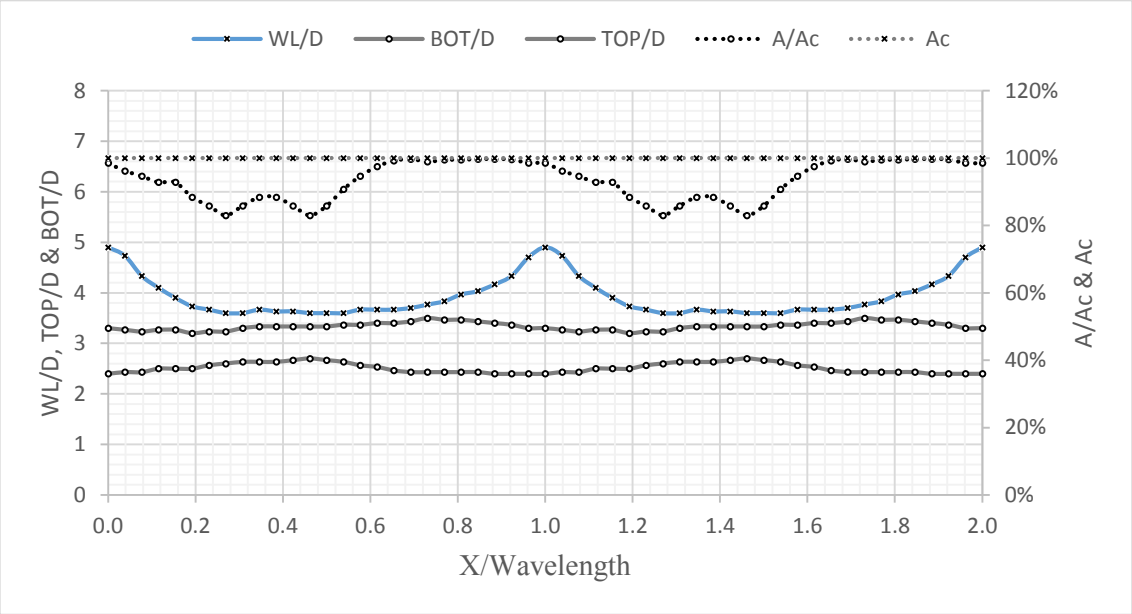

Figure 4-15 Relative area change (A/A_c) along the flexible tube for a wave propagating from right to left. A_c is the circular cross-sectional area of an undistorted tube. SWL and NDL are the 'still water level' and 'no deformation line' respectively. BOT/D and TOP/D are the relative bottom and top elevations respectively.

The subsequent sub-sections discuss the effects of frequency, tube's internal pressure, tube's position and wave height on the distortions and displacements of the flexible tube.

4.4.2 Effects of wave height and frequency on the distortions and displacements of the flexible tube

This section discusses effects of wave frequency and wave height on the geometric distortions and displacements of the flexible tubes in water waves. As discussed in section 4.3.1, the flow rates are mainly determined by wave heights i.e. flow rate increases with wave height. As discussed in the literature review, the wave energy is directly

proportional to the wave amplitude squared. Since wave energy is the driving force of the whole system, then wave heights play an important role in distorting the flexible tube. The number of distortions on the flexible tube in time τ is proportional to the frequency of the waves. Since frequency has minor effect on the flow rate at constant wave height, higher frequencies produce smaller pulses of flow through the tube whereas lower frequencies produce bigger pulses but the overall flow rate is approximately the same.

Wave heights *H* have an effect on the tube's average position/elevation. The flexible tube was clamped on both ends to keep them at fixed positions but was free to move vertically between the clamps and the displacements of the tube depend on the tension in the tube. The distance between the clamps was kept constant to maintain the same tension in the tube. The vertical displacement of the tube increases with *H* as shown in Figure 4-16. The elevations were non-dimensionalised by the tube diameter *D.* The tube's displacements were measured at the middle of the wave tank i.e. also the middle of the flexible tube.

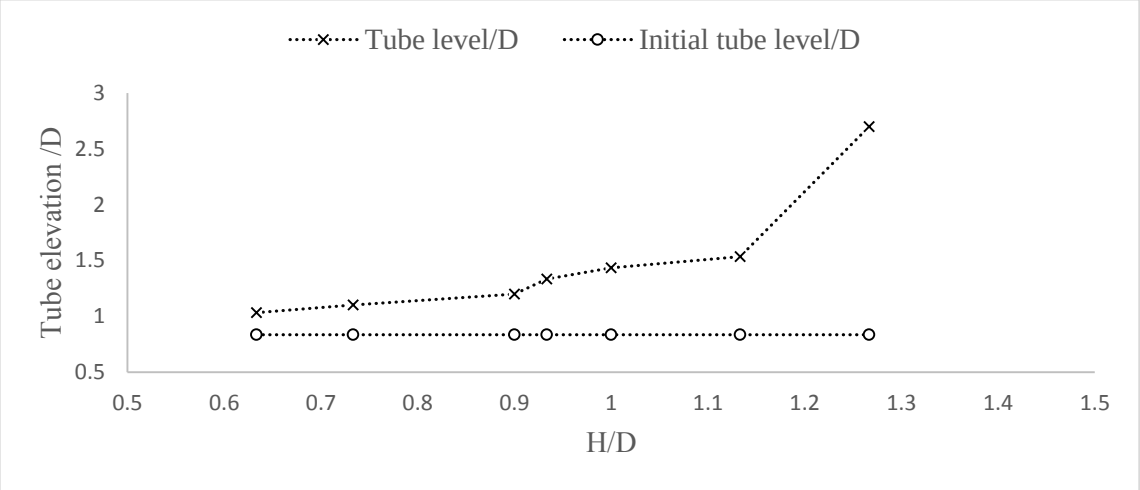

Figure 4-16 The effect of wave height on the tube level, the displacements of the tube from the initial tube level.

The initial tube level was kept constant at 25*mm* from the bottom of the flume. A maximum tube displacement of 56*mm* (81*mm*-initial tube level) occurred at a wave height of 40*mm*.

Figure 4-17 is a schematic representation of the vertical displacement of the flexible tube from the initial tube level at the wave height of 40*mm*. The maximum displacements occur at the middle section of the tube.

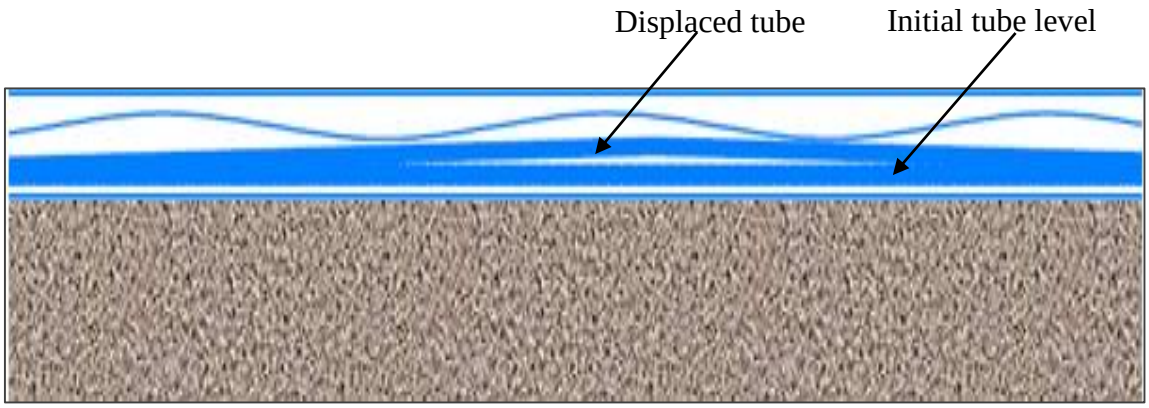

Figure 4-17 A schematic representation of the vertical displacement of the tube from its initial position.

The upward displacement resulted from net wave-induced forces acting upwards which increased wave height. Figure 4-18 shows that the tube deformations were unsymmetrical i.e. the tube was deformed more from the bottom than from the top.

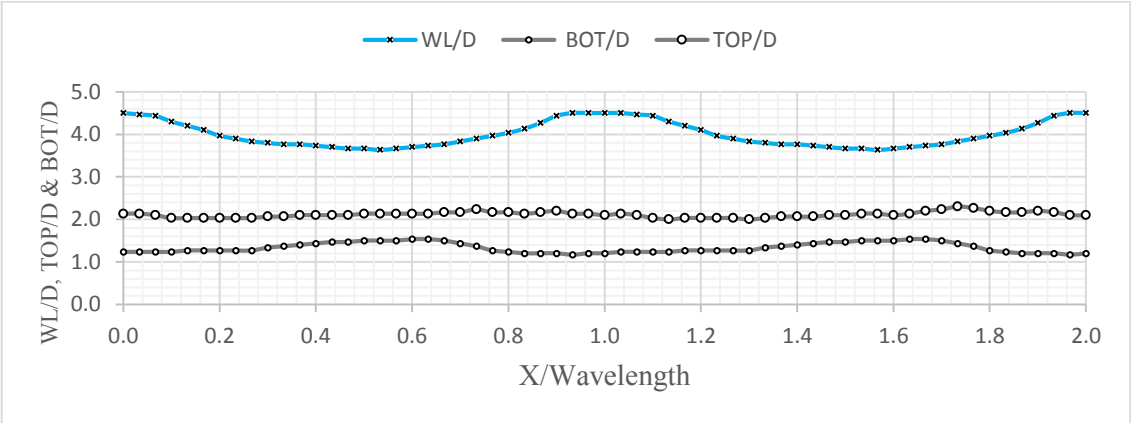

Figure 4-18 The unsymmetrical deformations of the flexible tube that caused a net upward displacement of the tube. BOT/D and TOP/D are the relative bottom and top elevations respectively. WL/D are the relative water levels while D is the tube diameter.

Further results on the effects of frequency f and wave height H on the geometric distortions of the flexible tube are also shown in Figures B-1, B-2, B-3, B-4, B-5, B-6 and B-7 in Appendix B. The Figures show that the tube's average level increases with wave height and frequency. The form of the waves changes with wave height.

4.4.3 Effect of the tube position on the distortions

The effects of tube positions on the geometric distortions cannot be easily quantified by just measuring the distortions. However, tube position has a significant impact on the flow rates. The effects of wave-induced pressures on the flexible tube decrease with water depth but the hydrostatic pressures increase with depth as discussed in section 4.3.3. Figures 4-19, 4-20 and 4-21 show the tube deformations at average tube levels of 100*mm*, 85*mm* and 45*mm* from the surface of the waves respectively.

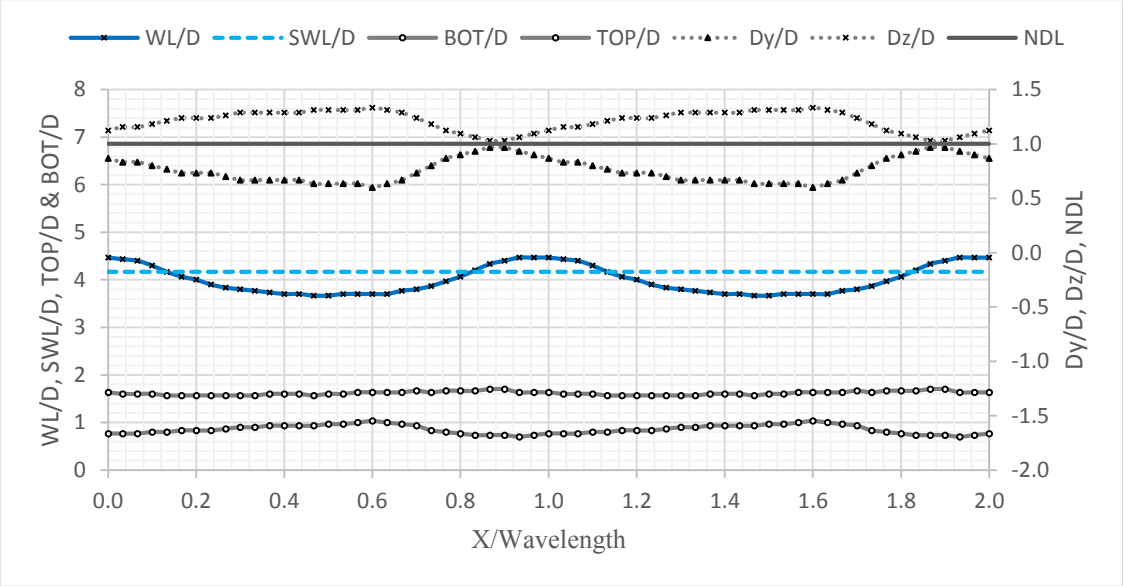

Figure 4-19 *The distortions of the tube at an average elevation of 100mm from the surface of the waves. D_y/D and D_z/D are vertical and horizontal deformations respectively. SWL and NDL are the 'still water level' and 'no deformation line' respectively. BOT/D and TOP/D are the relative bottom and top elevations of the tube respectively.*

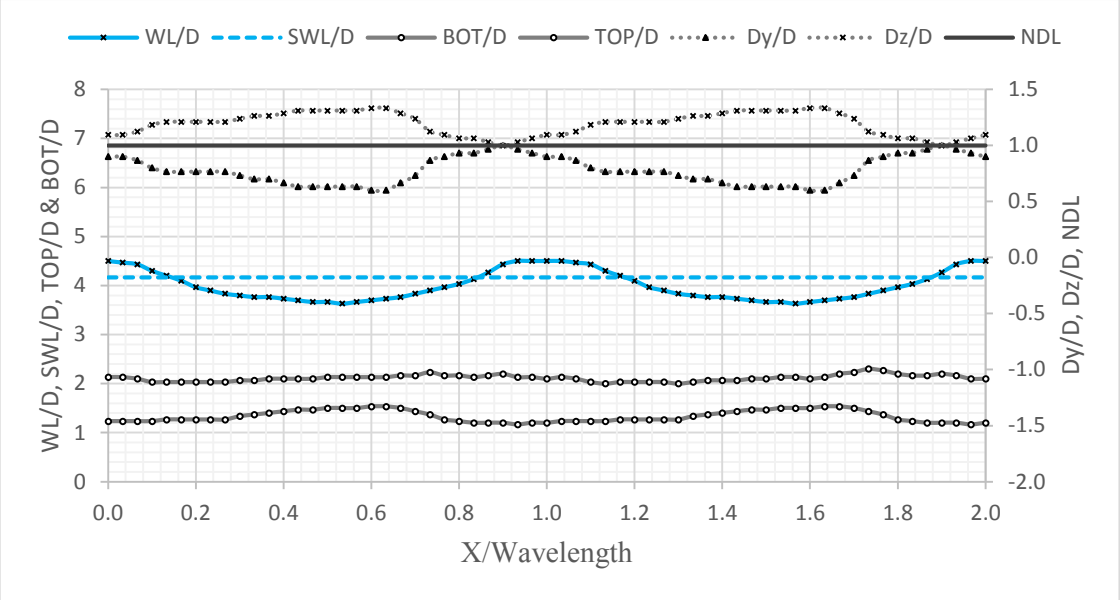

Figure 4-20 *The distortions of the tube at an average elevation of 85mm from the surface of the waves. D_y/D and D_z/D are vertical and horizontal deformations respectively. SWL and NDL are the 'still water level' and 'no deformation line' respectively. BOT/D and TOP/D are the relative bottom and top elevations of the tube respectively.*

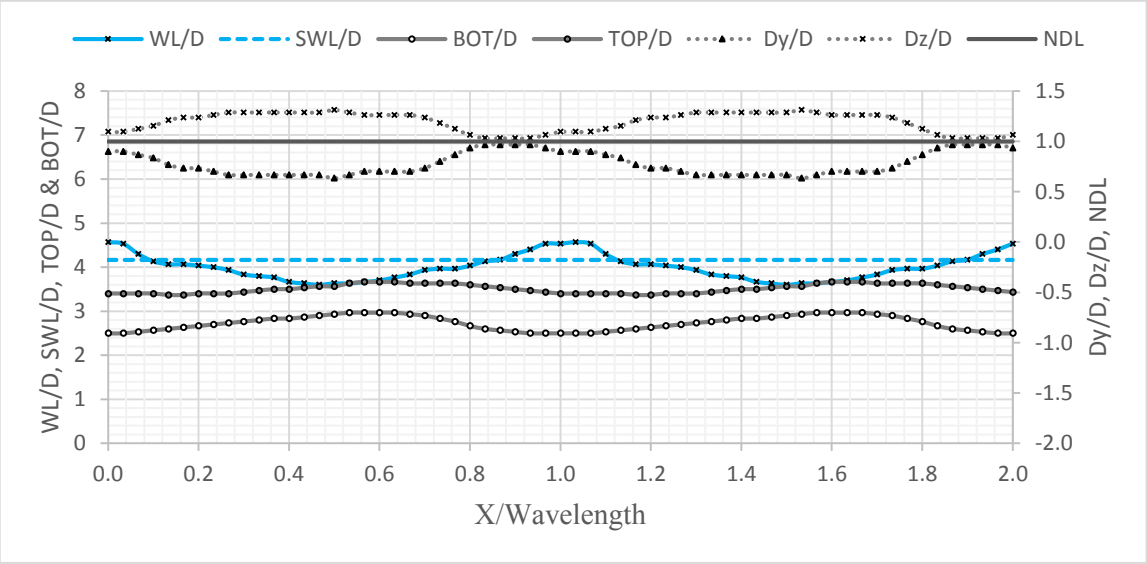

Figure 4-21 *The distortions of the tube at an average elevation of 45mm from the surface of the waves. D_y/D and D_z/D are vertical and horizontal deformations respectively. SWL and NDL are the 'still water level' and 'no deformation line' respectively. BOT/D and TOP/D are the relative bottom and top elevations of the tube respectively.*

The shape of the deformed tube did not change much in Figures 4-19 and 4-20 when the flexible tube was not interfering with the wave surface but in Figure 4-21, the tube was interfering with the waveform causing an increase in wave dissipation and this resulted in a significant reduction in the average flow rates through the tube.

4.4.4 Effects of internal pressure of the tube on the distortions

The wave characteristics were kept constant while the tube's internal pressure was increased by increasing the pressure head Δp as described in chapter 3. The effects of the internal pressure on the tube deformations is shown in Figures 4-22, 4-23 and 4-24 at Δp of +0mm, +4mm and +8mm respectively. The resultant average flow rates were 21*ml/s*, 19.7*ml/s* and 17.9 *ml/s* respectively.

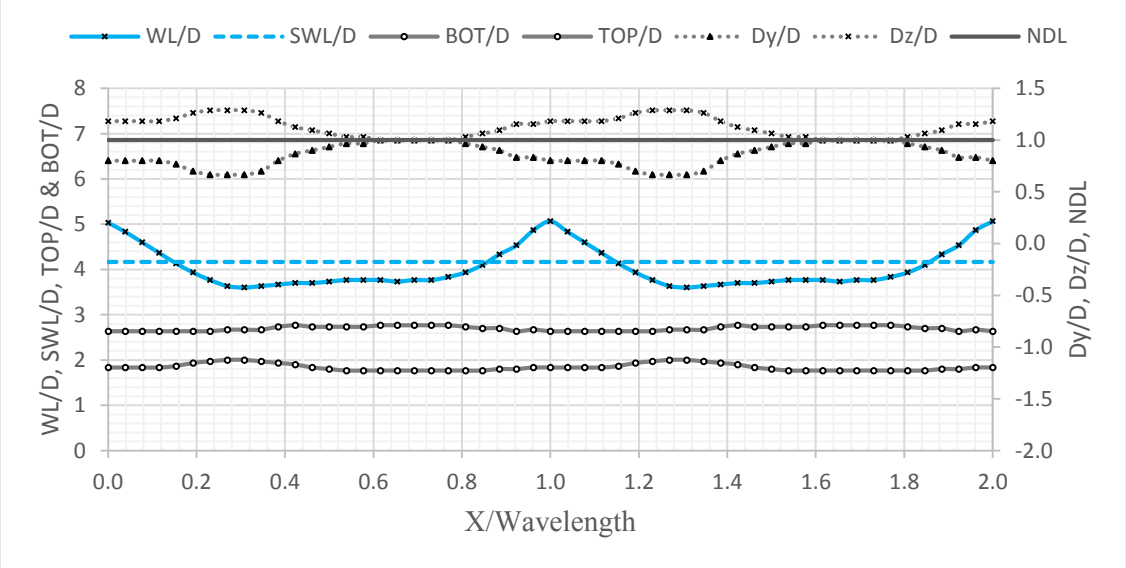

Figure 4-22 *The graphs showing the shape of the flexible tube in progressive waves at a pressure head of 0mm. D_y/D and D_z/D are vertical and horizontal deformations respectively. SWL and NDL are the 'still water level' and 'no deformation line' respectively. BOT/D and TOP/D are the relative bottom and top elevations of the tube respectively.*

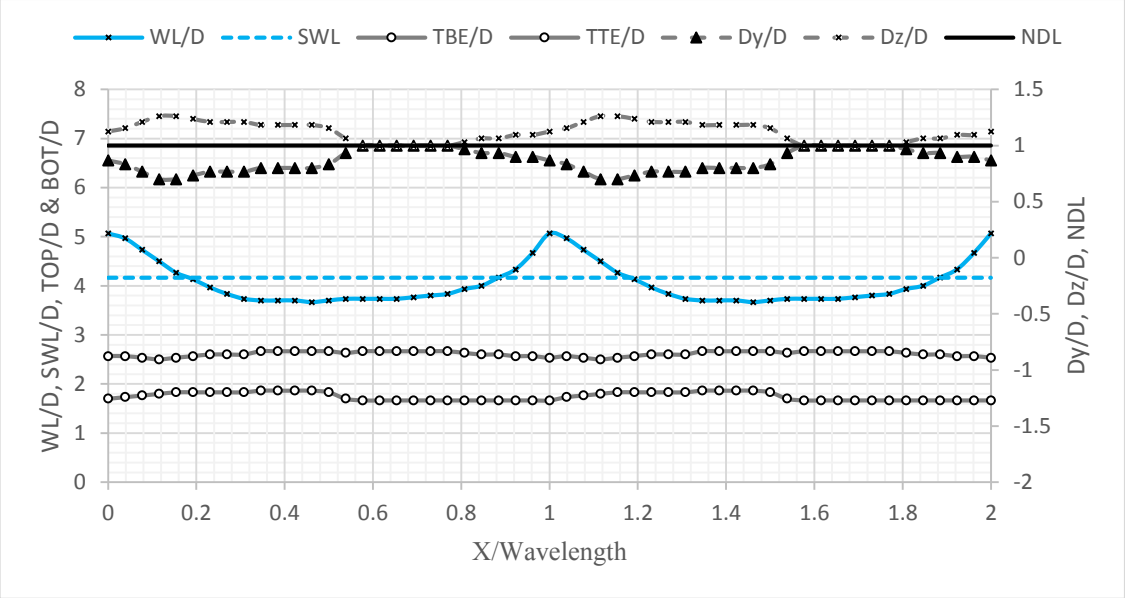

Figure 4-23 *The graphs showing the shape of the flexible tube in progressive waves at a pressure head of +4mm. D_y/D and D_z/D are vertical and horizontal deformations respectively. SWL and NDL are the 'still water level' and 'no deformation line' respectively. TBE/D and TTE/D are the relative bottom and top elevations of the tube respectively.*

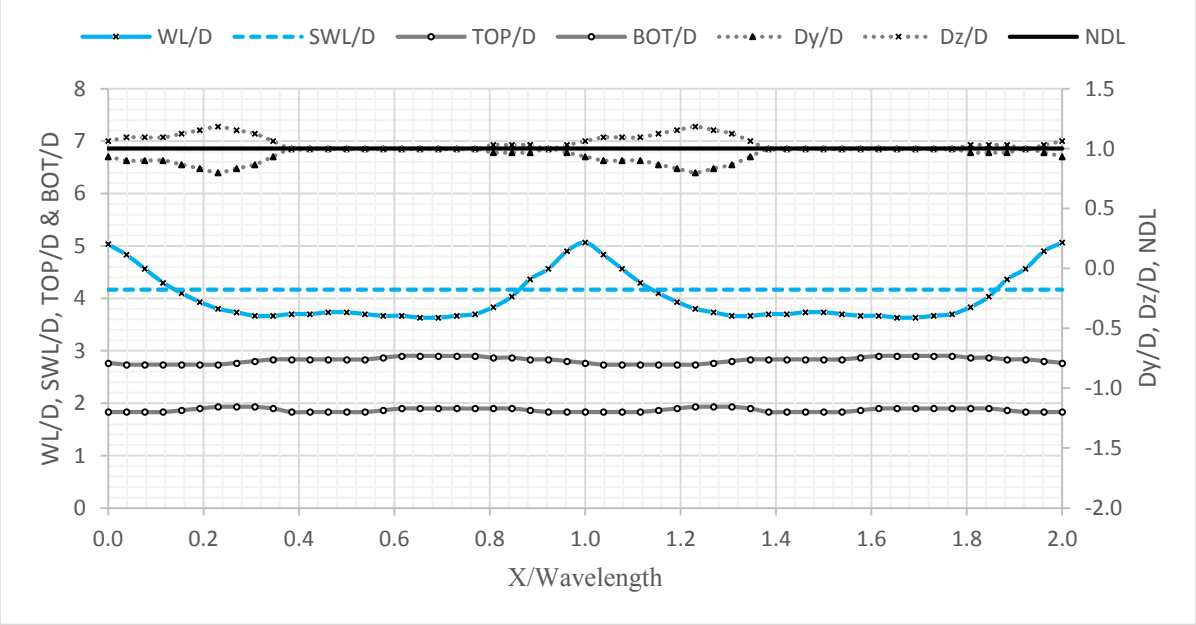

Figure 4-24 *The graphs showing the shape of the flexible tube in progressive waves at a pressure head of +8mm. D_y/D and D_z/D are vertical and horizontal deformations respectively. SWL and NDL are the 'still water level' and 'no deformation line' respectively. BOT/D and TOP/D are the relative bottom and top elevations of the tube respectively.*

Increasing the pressure head results in a decrease in flow rate as well as the magnitudes of the deformations as shown by D_y/D and D_z/D. The tube deformations were significant at $\Delta p = 0mm$ and Δp =+4mm (see Figures 4-22 and 4-23) but there were lesser deformations as Δp was further increased to +8mm (Figure 4-24). Also in Figure 4-24, most the data points D_y/D and D_z/D lied along the NDL (i.e. the '*no deformation line'*) as compared to Figures 4-22 and 4-23. Increasing the tube's internal pressure results in the tube being stiffer i.e. harder for wave- induced pressures to deform the tube. These pressures varied along the tube since they are progressive waves.

4.5 Residence time in the flexible, floating tube

Generally, residence time is defined as the average time a substance spend in a specific location (Shen and Haas, 2004). In this research, residence time is the average time fluid particles spend in the flexible tube. The residence time is important in microalgae cultivation in determining how much time is required for the microalgae cells to travel in the flexible tubes before they can be harvested. However, the actual cultivation of microalgae in FTPBR is beyond the scope of this research. The total volume of water in the flexible tube used for this experiment was 4.4 litres. The residence time increases with decrease in flow rate as shown in Figure 4-25. Froude numbers can be used to establish a geometric similarity between laboratory model and full- scale prototype. In this research, it is useful in estimating residence time for different diameters of flexible tubes. This will be discussed in section 4.8.

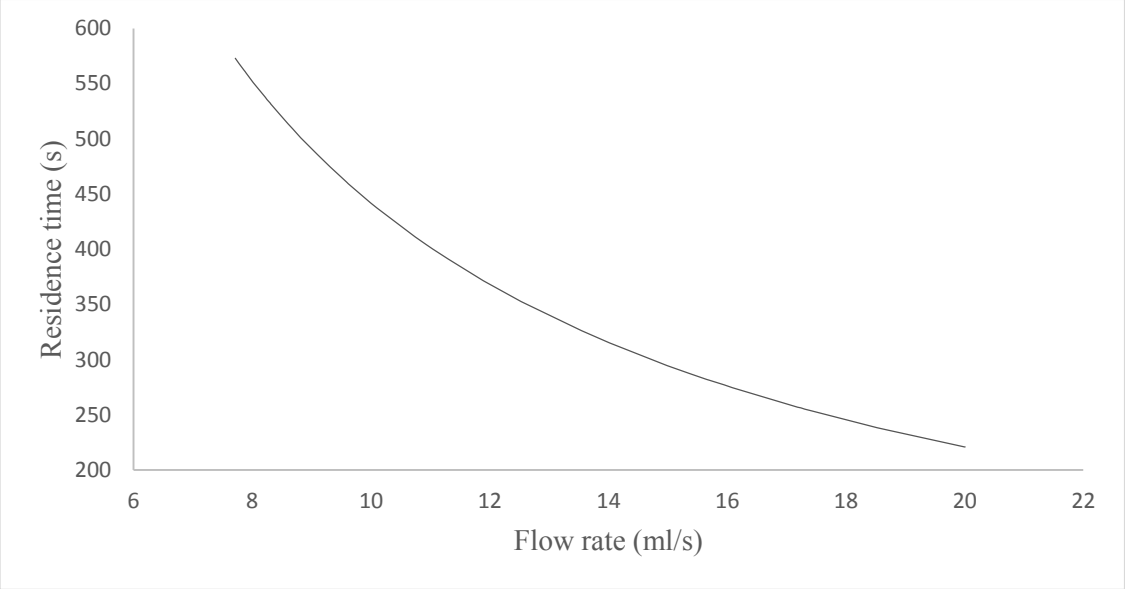

Figure 4-25 Relationship between residence time and flow rate for the experiments conducted.

4.6 Particle analysis in the flexible tube

White polystyrene particles were seeded in the FTPBR system in order to characterise the flow fields of water particles in the flexible tube. The tracer particles were illuminated by fluorescent lamps to improve their visibility in the fluid. The number of particles was limited to minimise their interaction with each other to avoid altering the properties of flow as discussed in chapter 2. This is necessary in order to avoid bias in the flow measurements. Experiments to determine the flow fields were performed, the results and discussion are presented in subsequent subsections.

Particle tracking velocimetry (PTV) was used for the analysis of the flow fields. PTV evaluates the velocities of water particles by capturing image positions of tracer particles at successive time steps (Umeyama et al. 2010). The velocities of the tracer particles are then calculated from their displacements and the exposure time between successive image frames. The motion of particles in the flexible polyethylene tube was observed from a fixed field of view. This is an example of Eulerian motion where the velocities of fluid particles are measured by the observer at a fixed point (see e.g. Dean and Dalrymple, 2010). Due to the limited supply and short lifespan of the flexible polyethylene tubes, only flow measurements for one wave characteristic were completed. The wave height

was 36*mm* and the average flow rate was 11.9*ml/s*. The shutter speed (exposure time) and the frame rate for the camera were 1/30 *s* and 24 fps respectively.

4.6.1 Settling velocities of tracer particles

Settling velocities of particles were measured in still water. The settling velocities of particles in still water differ from the settling velocities of the same particles in turbulent flows because of the bias due to the particle inertia (Wang and Maxey, 1993). Figure 4-26 shows the probability distribution of the particles' settling velocities v_{ts} relative to the average fluid velocity v for the conducted experiments. The v_{ts}/v were less than 1 for 98% of the particles which means that most of the particles' average velocities were less than the average fluid velocity so the polystyrene particles were reasonably a good representative of the fluid particles.

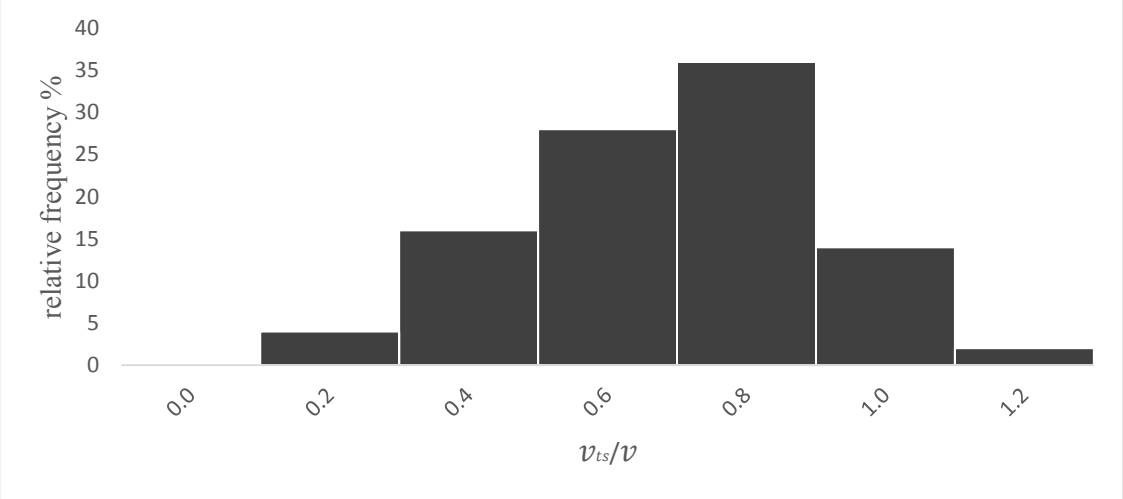

Figure 4-26 Relative settling velocities of the tracer polystyrene particles

The settling velocities v_{ts} of the particles were calculated using equation 4.1:

$$v_{ts} = \sqrt{\frac{4}{3}\frac{(\rho_s - \rho_f)}{\rho_f}\frac{Dg}{C_D}} \qquad (4\text{-}2)$$

where ρ_s and ρ_f are particle and fluid densities respectively, D is the diameter of a particle, g is the gravitational acceleration and C_D is a drag coefficient.

4.6.2 Particle motion in the flexible tube using PTV

Figure 4-27 shows the water levels (WL) and the flexible tube elevation relative to the wave profile along the tube. Waves were moving from right to left. The length of the tube equivalent to 1 wavelength was divided into 14 segments (control volumes) in order to simplify the analysis since the flow fields varied along the tube.

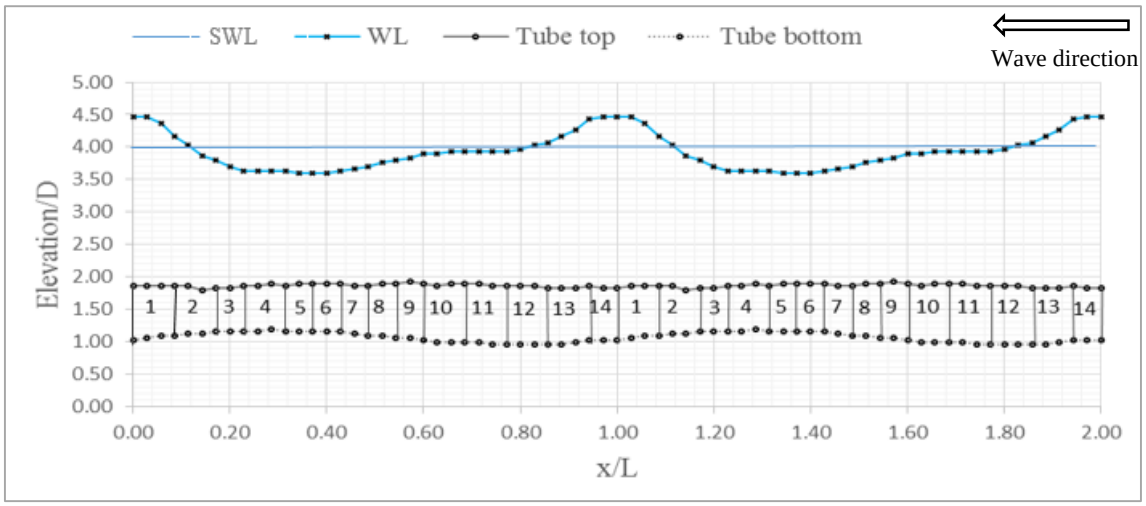

Figure 4-27 *The water levels (WL) and the tube levels for 2 wavelengths L of the generated waves. SWL is the still water level. The length of the tube equivalent to 1 wavelength was segmented into 14 control volumes. X is the distance of a reference crest from a stationary starting point. The waves were moving right to left.*

The direction of motion and the relative displacements of the particles in each of the control volumes are presented in Figures 4-28 to 4-41. The figures show the displacements of the particles in a flexible tube in two successive frames. The displacements were measured in pixels where 100 pixels represent particle velocity v of 540mm/s or relative velocity v/c = 0.5, with c being the celerity of the waves. This subsection presents a qualitative analysis of the particle motion in each of the control volumes along the flexible tube. A detailed quantitative analysis of the particles motion will be presented in subsequent subsections.

Figure 4-28 shows the particle displacement in control volume 1 which is directly under the wave crest as shown by the legend. Most particles were moving in the wave direction which is also the forward direction of pumping.

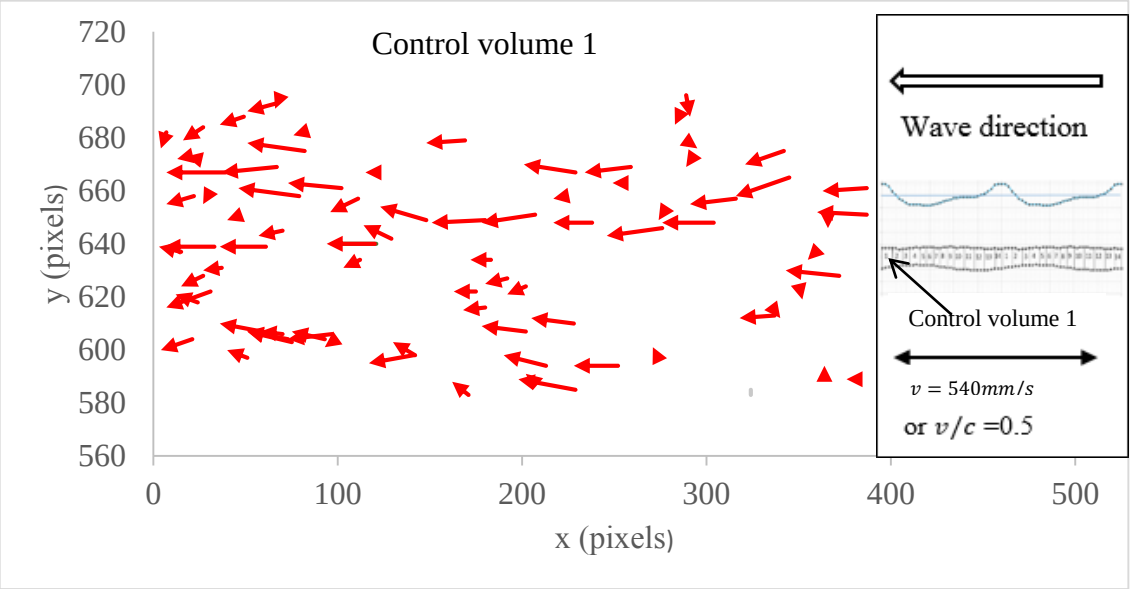

Figure 4-28 Polystyrene particles motions and relative velocity magnitudes in control volume 1 (i.e. from x/L =0 to 0.17).

Figure 4-29 shows that the particles in control volume 2 (i.e from x/L = 0.09 to 0.17) suddenly changed the direction of motion from moving in the wave direction as in control volume 1 to opposite the wave direction due to the approaching constriction in the flexible tube which tends to suck the particles in the reverse direction. A constriction in the tube pushes most of the fluid ahead of it but allows the fluid immediately ahead or within it to pass through it in the opposite direction. The relative displacements were also higher than those in control volume 1 due to the rapid change in the direction of motion as shown by the increase in the sizes of the arrows.

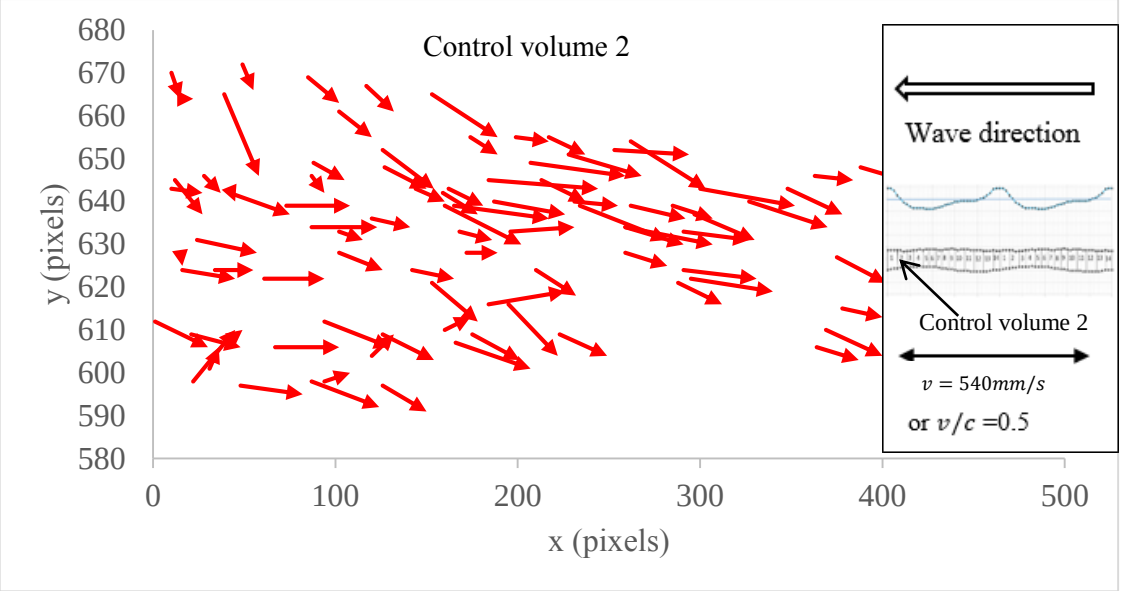

Figure 4-29 Polystyrene particles motions and relative velocity magnitudes in control volume 2 (i.e. from x/L =0.09 to 0.17).

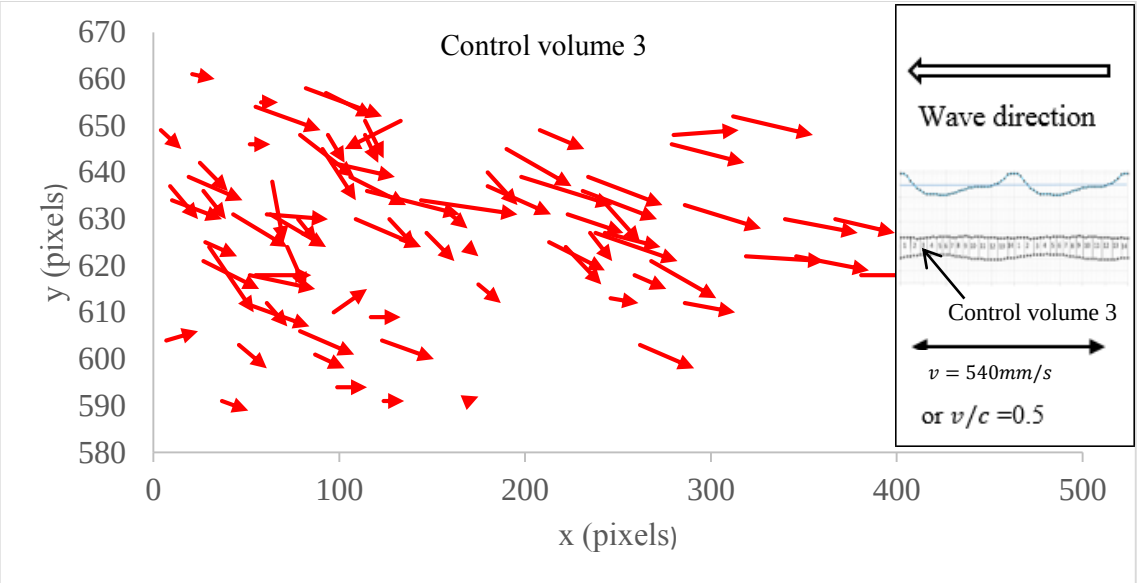

Figure 4-30 Polystyrene particles motions and relative velocity magnitudes in control volume 3 (i.e. from x/L =0.17 to 0.23).

The particles continued in the direction opposite to the wave in control volume 3 (i.e. from x/L = 0.17 to 0.23) which was also in the constriction as shown in Figure 4-30.

In control volume 4 (i.e. x/L = 0.23 to 0.31), the particles were still moving opposite the wave direction but the displacement magnitudes had decreased (see Figure 4-31).

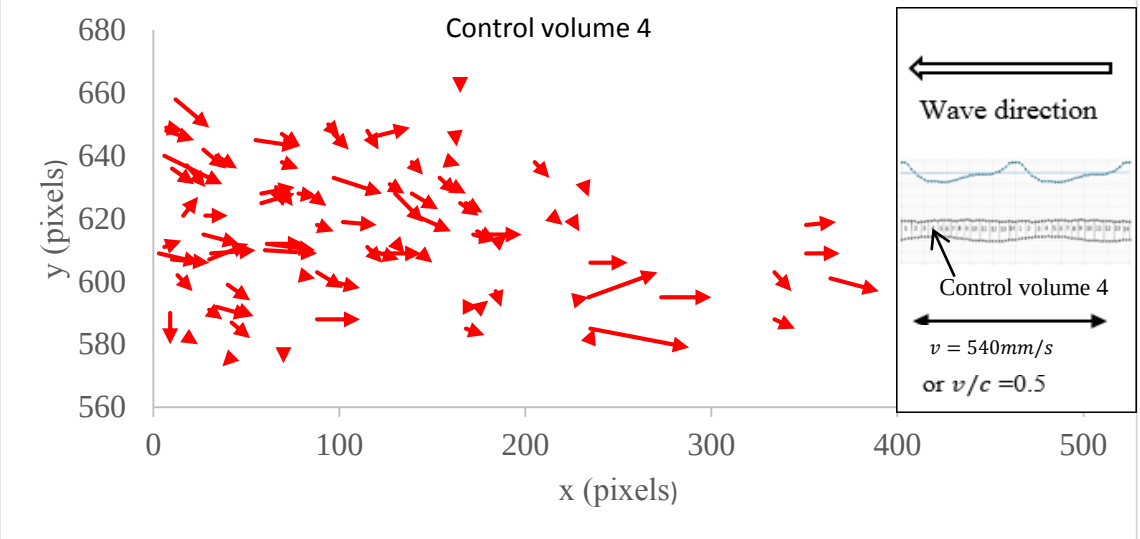

Figure 4-31 Polystyrene particles motions and relative velocity magnitudes in control volume 4 (i.e. from x/L =0.23 to 0.31).

In control volume 5 (i.e. from x/L = 0.31 to 0.37), there was an increase in the relative average displacements of the particles as compared to the previous control volume. The displacements were still in the opposite direction of the waves as shown in Figure 4-32.

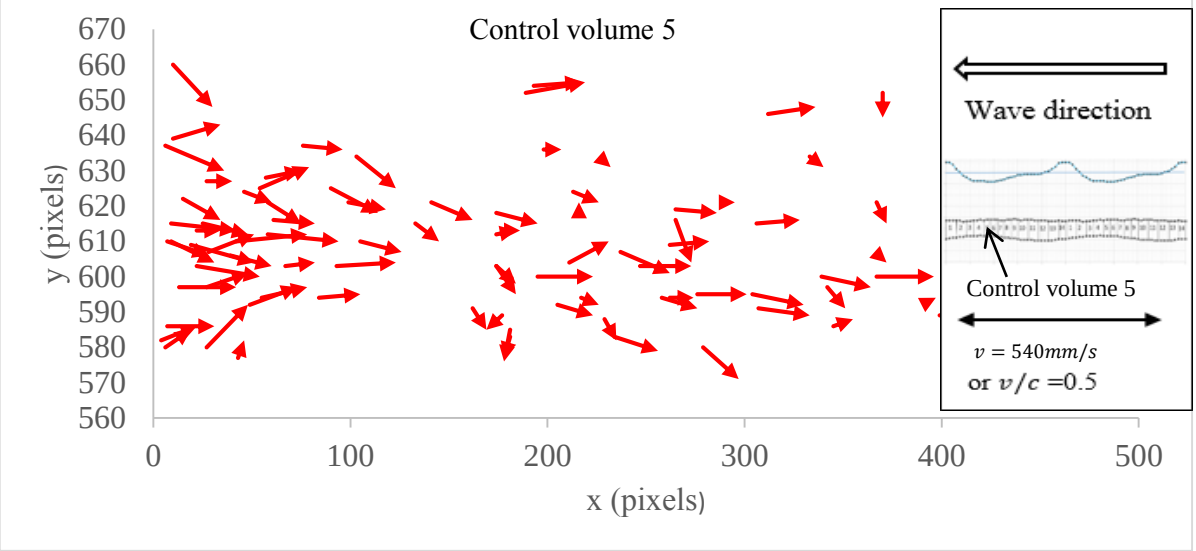

Figure 4-32 Polystyrene particles motions and relative velocity magnitudes in control volume 5 (i.e. from x/L =0.31 to 0.37).

Figure 4-33 shows the particles' displacements in control volume 6 (from x/L = 0.37 to 0.43). The particles were moving in all directions and there was an increase in vertical motion. This indicates a sudden burst of turbulence within the tube since the particles were initially moving opposite to the wave direction. The turbulence was due to the

sudden expansion of the fluid flow which resulted in rapid deceleration of the particles at the end of the tube's constriction. The turbulence is vital for the mixing process in the microalgae cultivation as it enhances the availabity of nutrients to the microalgae cells as discussed in chapter 2.

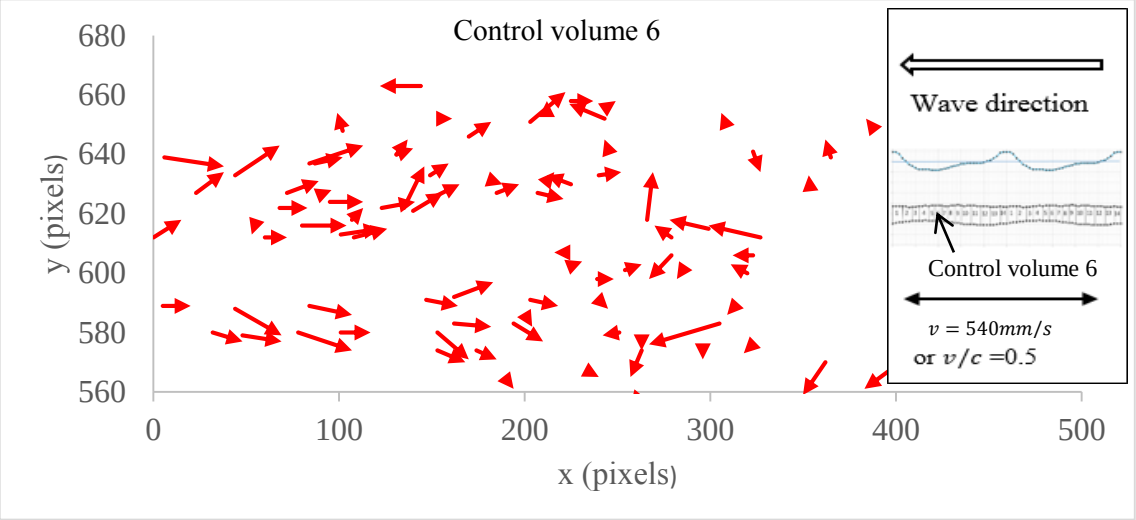

Figure 4-33 Polystyrene particles motions and relative velocity magnitudes in control volume 6 (i.e. from x/L =0.37 to 0.43).

The particles' displacements in control volume 7 (from x/L = 0.43 to 0.49) are shown in Figure 4-34. The velocity magnitudes of the particles were relatively lower than those in the previous control volume. The particles were still moving in all directions due to the burst of turbulence.

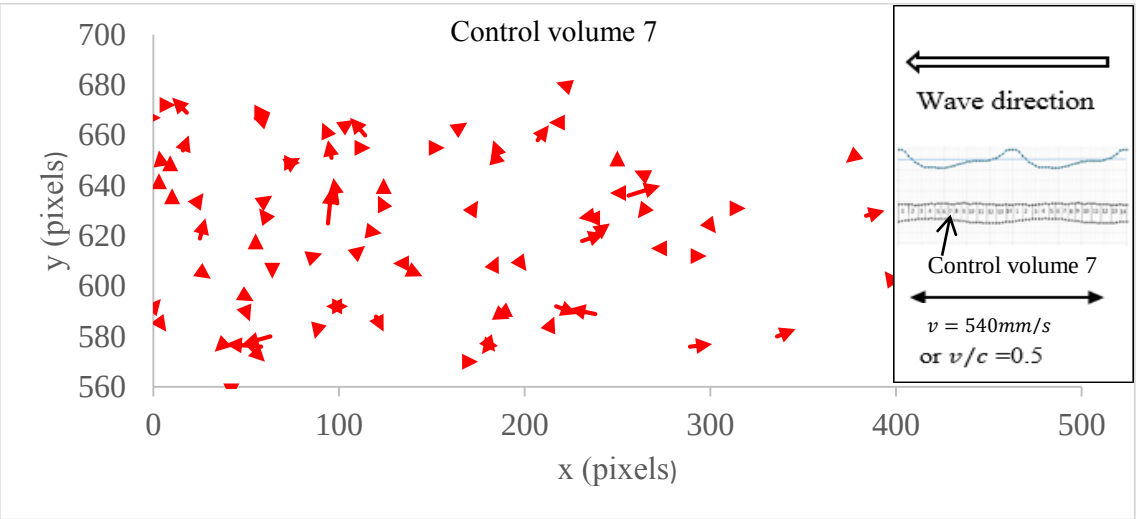

Figure 4-34 Polystyrene particles motions and relative velocity magnitudes in control volume 7 (i.e. from x/L =0.43 to 0.49).

In control volume 8 (i.e. from x/L = 0.49 to 0.54), most particles started to move in the wave direction as shown in Figure 4-35. The movement of the particles in the wave direction was due to the fluid pumping caused by a successive constriction in the tube which was about half a wavelength away from this control volume. The particles were less turbulent in this control volume. The average displacements of the particles increased as compared to the previous control volume.

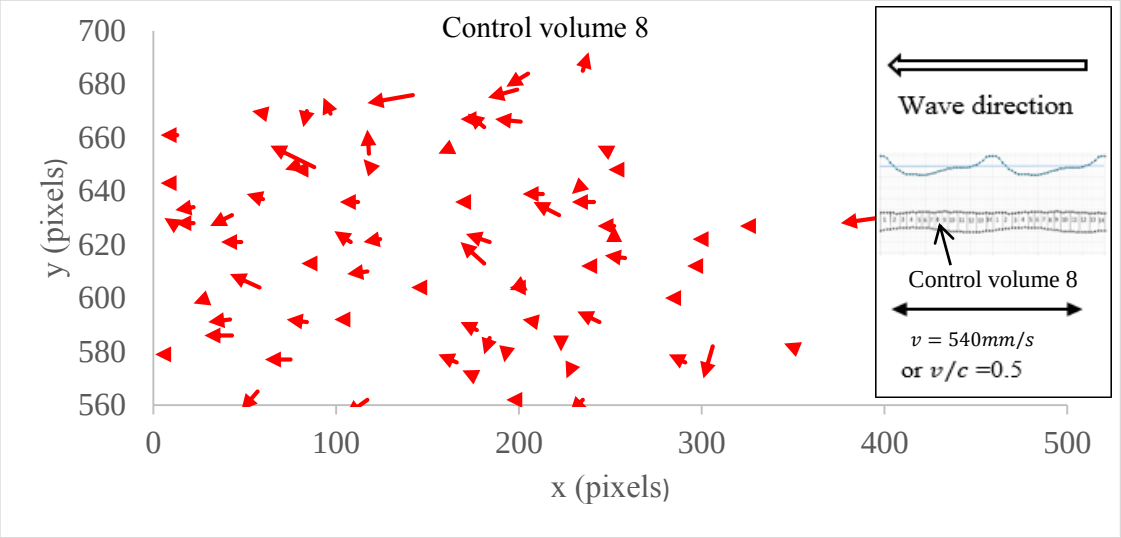

Figure 4-35 Polystyrene particles motions and relative velocity magnitudes in control volume 8 (i.e. from x/L =0.49 to 0.54).

There was a significant increase in displacements of the particles in control volume 9 (i.e. from x/L = 0.54 to 0.60) as shown in Figure 4-36. There were less vertical movements of particles which marks the end of the turbulence in the tube in this wavelength. Most particles were moving in the wave direction.

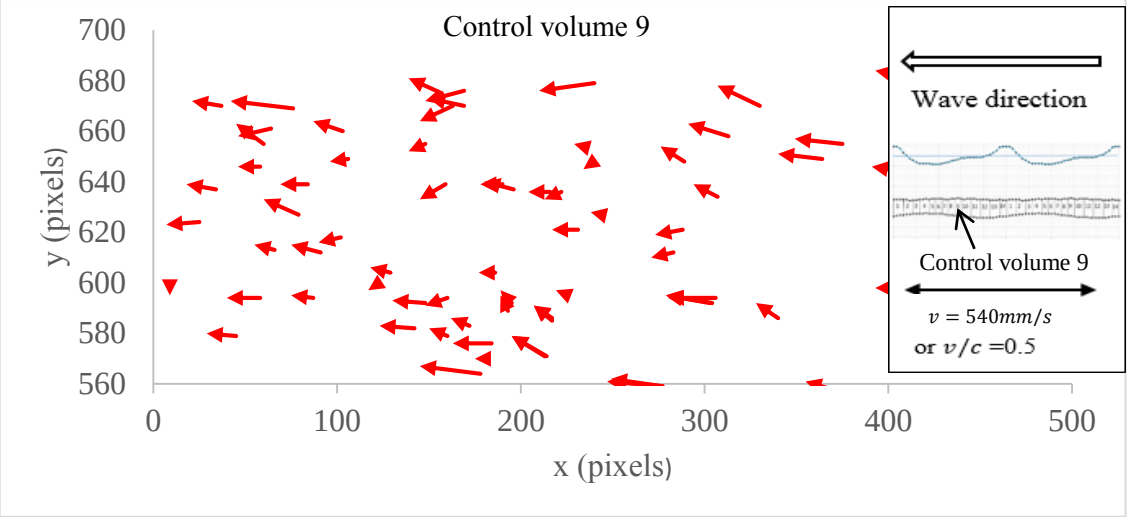

Figure 4-36 Polystyrene particles motions and relative velocity magnitudes in control volume 9 (i.e. from x/L =0.54 to 0.60).

The particles continued to move in the wave direction in control volume 10 (i.e. from x/L = 0.60 to 0.69). There was an increase in the average displacements of the particles as compared to the previous control volume as the constriction approaches. The displacements of particles in control volume 10 are shown in Figure 4-37.

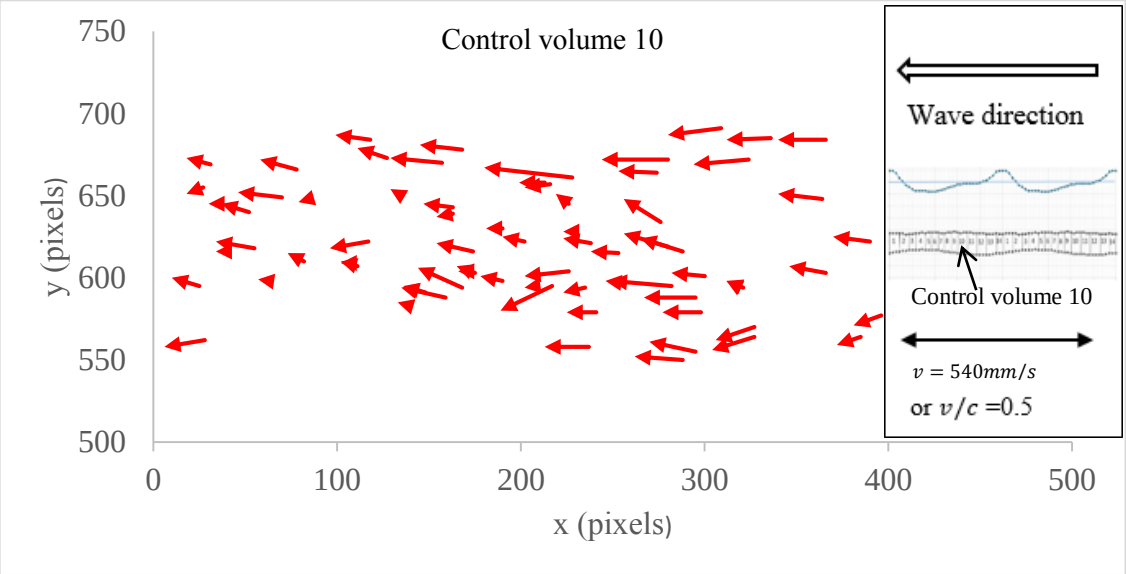

Figure 4-37 Polystyrene particles motions and relative velocity magnitudes in control volume 10 (i.e. from x/L =0.60 to 0.69).

The particles continued to move in the wave direction in control volume 11 (i.e. from x/L = 0.69 to 0.77) as shown in Figure 4-38.

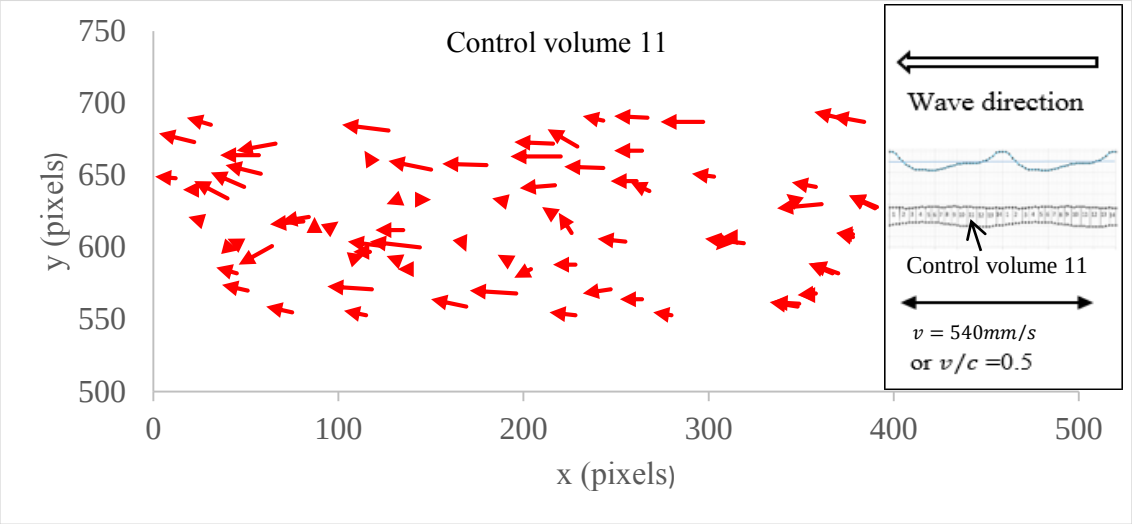

Figure 4-38 Polystyrene particles motions and relative velocity magnitudes in control volume 11 (i.e. from x/L =0.69 to 0.77).

Figure 4-39 shows the displacement of particles in control volume 12 (i.e. from x/L = 0.77 to 0.86). Particles were moving in the wave direction with increased average displacements as compared to the previous control volume.

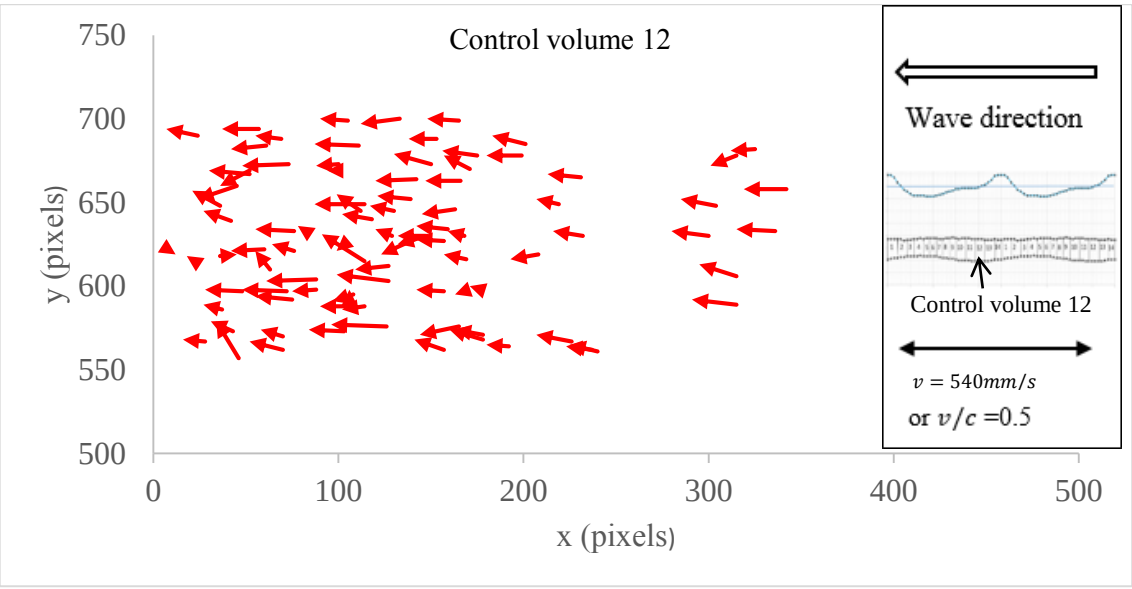

Figure 4-39 Polystyrene particles motions and relative velocity magnitudes in control volume 12 (i.e. from x/L =0.77 to 0.86).

The particles continued to move in the wave direction in control volume 13 (from x/L = 0.86 to 0.94). The displacement vector fields of the particles in control volume 13 are shown in Figure 4-40.

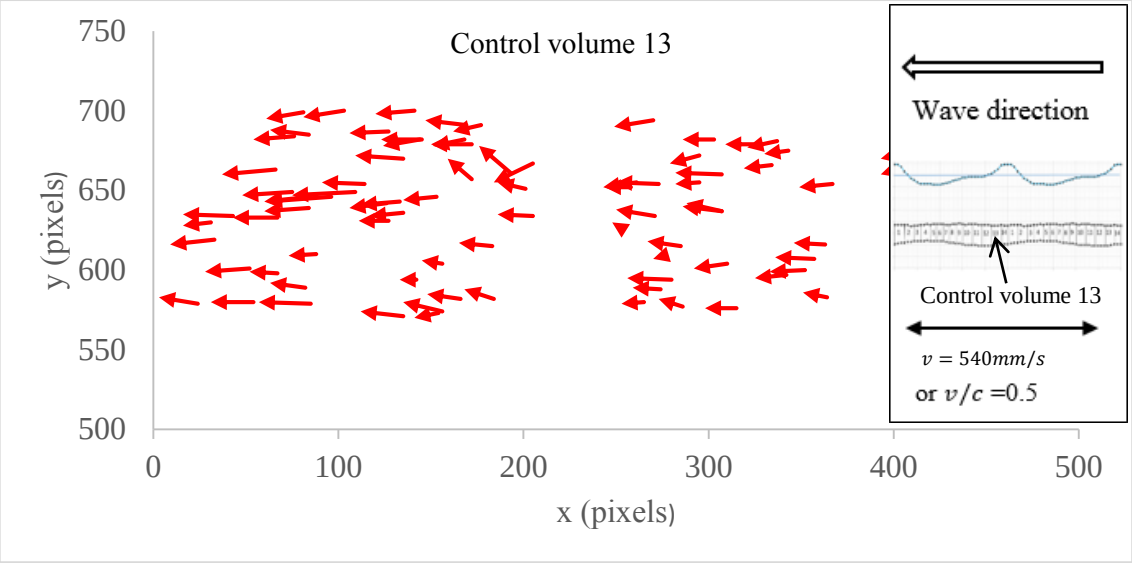

Figure 4-40 Polystyrene particles motions and relative velocity magnitudes in control volume 13 (i.e. from x/L =0.86 to 0.94).

Control volume 14 (i.e. from x/L = 0.94 to 1.00) is just before a successive wave crest. The particles were moving in the wave direction as shown in Figure 4-41.

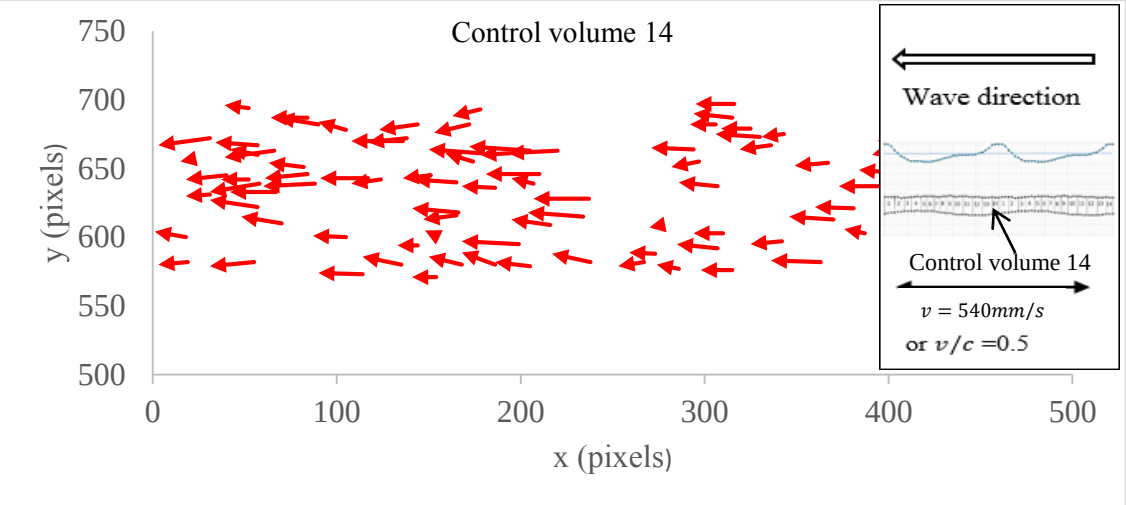

Figure 4-41 Polystyrene particles motions and relative velocity magnitudes in control volume 14 (i.e. from x/L =0.94 to 1.00).

The constrictions in the tube play an important role in the pumping of the fluid. The presence of the constrictions creates progressive waves of area change which pump the fluid in a manner analogous to the peristalsis of substances in the vascular systems. The constrictions push the fluid ahead of them in the wave direction but allowing the fluid immediately ahead of them or within them to pass through in the opposite direction so

the particles motion was oscillatory. Presented in the subsequent sub-sections are the quantitative analyses of the particle flow in each of the control volumes.

4.6.3 Mean relative velocities of the particles along the flexible tube

The mean velocities $\bar{u}$ and $\bar{v}$ i.e. horizontal and vertical components respectively of velocities relative to the wave celerity c for the 14 control volumes are presented in this sub-section. These are shown in Table 4-1 and in Figure 4-42. In this research, the magnitudes of horizontal velocities in the wave direction have a positive sign (+) while horizontal velocities against the wave direction are given a negative sign (-). An upward vertical velocity have a positive sign (+) while a downward vertical velocity have a negative sign (-).

Table 4-1 The mean relative velocities $\bar{u}/c$ and $\bar{v}/c$ (horizontal and vertical respectively) of the particles in each of the 14 control volumes.

Control volume	$\bar{u}/c$	$\bar{v}/c$
1	+0.071	+0.003
2	-0.129	+0.017
3	-0.129	+0.023
4	-0.052	+0.012
5	-0.084	+0.009
6	-0.025	+0.001
7	-0.005	-0.006
8	+0.046	-0.003
9	+0.088	-0.007
10	+0.087	-0.007
11	+0.062	-0.011
12	+0.077	-0.009
13	+0.093	+0.001
14	+0.098	-0.002

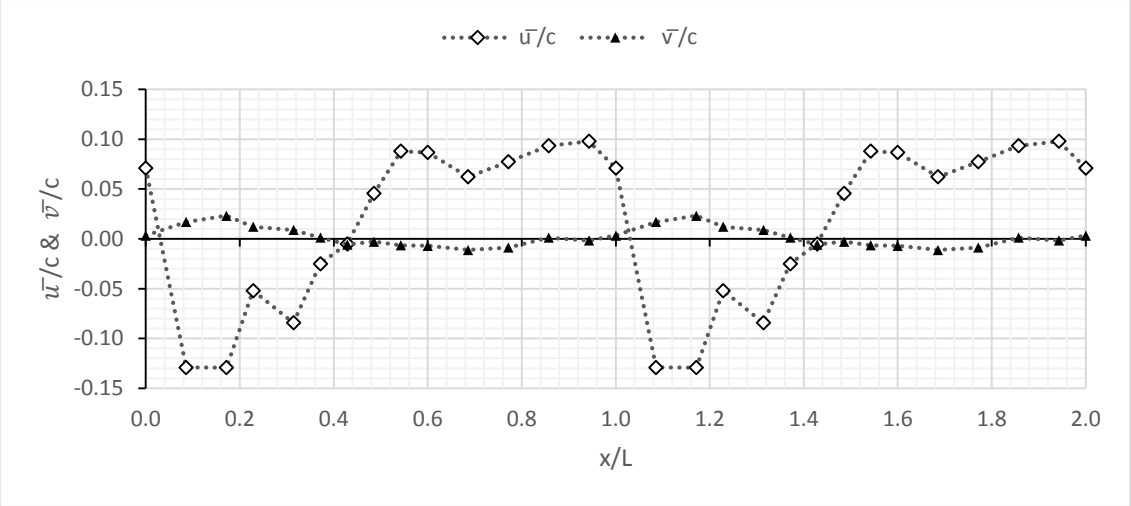

Figure 4-42 The relative mean velocities $\bar{u}/c$ and $\bar{v}/c$ (horizontal and vertical respectively) of the particles in each of the 14 control volumes for 2 wavelengths of the wave. The data points are joined by dotted lines for clarity. Positive velocities represent forward or upward motion of the particles.

At crests (i.e. at x/L = 0, 1 or 2), the mean relative horizontal velocity of the particles was + 0.071 in the direction of the wave (right to left). Immediately after the crest, the particles suddenly travelled in the reverse direction (opposite to wave direction) at an average relative horizontal velocity of -0.129. The particles were moving relatively upwards. The mean relative vertical velocities increased from +0.003 in control volume 1 to +0.017 in control volume 2 (x/L =0.09 to 0.17). The particles reached their maximum average relative vertical velocity of +0.023 in control volume 3 (x/L = 0.17 to 0.23). The particles continued moving upwards until they reached control volume 7 (x/L = 0.37 to 0.43) where they started to move relatively downwards. The particles travelled at an average relative horizontal velocity of -0.129 in control volume 3 (x/L =0.17 to 0.23). The average relative horizontal velocities reduced from -0.129 to -0.052 in control volume 4 (x/L = 0.23 to 0.31) then increased to -0.084 in control volume 5 (x/L =0.31 to 0.37). These fluctuations in horizontal velocities were caused by pressure variations due to the deformations of the flexible tube. The mean relative horizontal velocity reduced from -0.084 to -0.025 in control volume 6 (x/L =0.37 to 0.43). A burst of turbulence occurred in control volume 6 due to rapid decelerations of particles associated with a sudden expansion of the flow. Figure 4-43 shows the maximum vertical constriction of the tube and the burst of

turbulence immediately after the constriction. Figure 4-44 is a close-up image showing the particles in the flexible tube, the wave profile and the maximum vertical constriction.

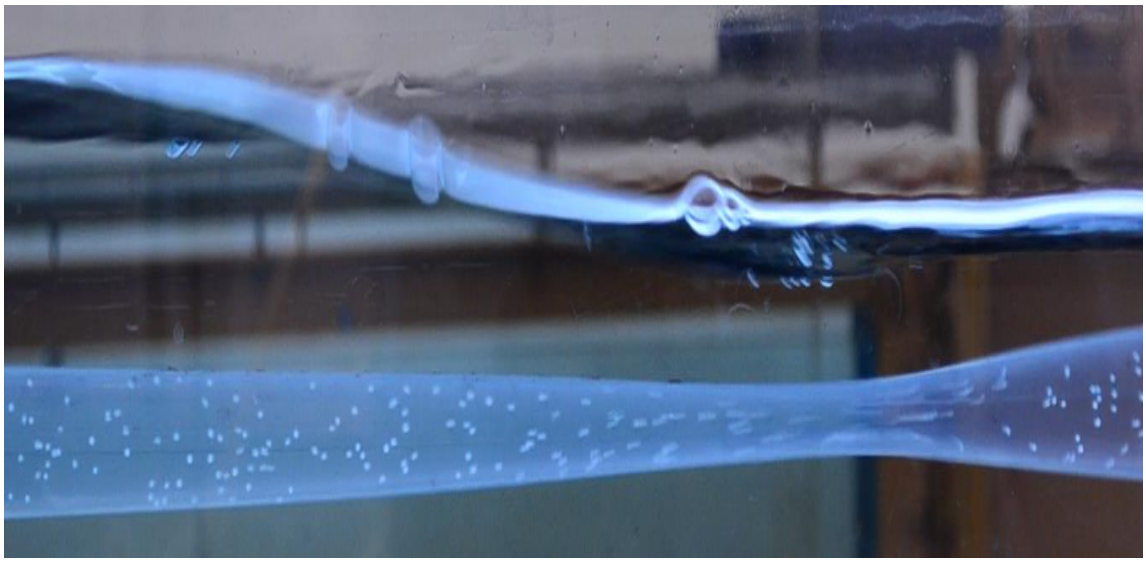

Figure 4-43 Maximum constriction of the flexible tube in control volume 6 (x/L =0.37 to 0.43) and the resulting turbulence.

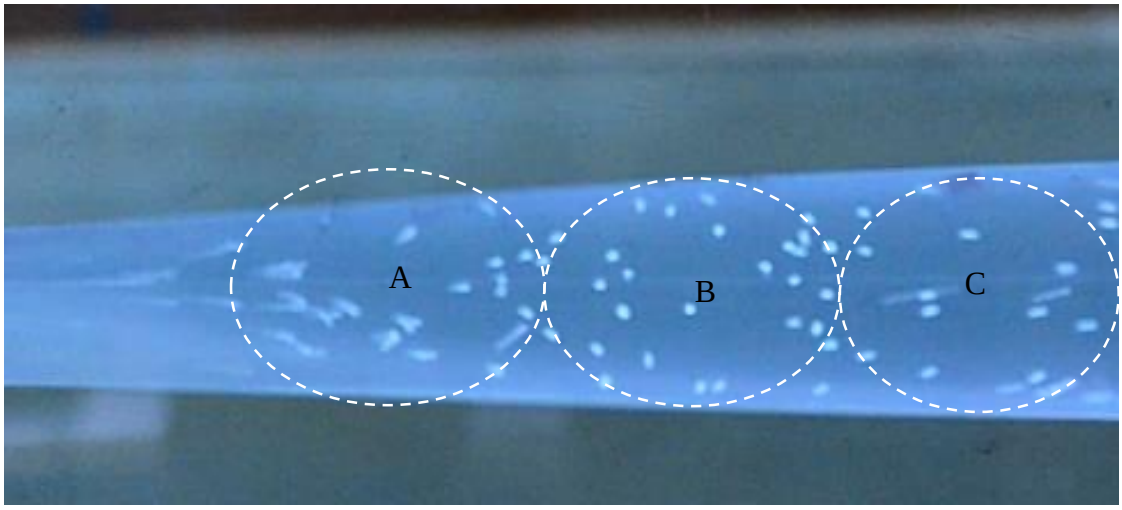

Figure 4-44 The burst of turbulence enclosed in A that occurred in control volume 6 (x/L =0.37 to 0.43). The particles were stationary in B (x/L = 0.43 to 0.46) and then started to move right to left in C (x/L = 0.46 to 0.49).

The region A is immedately after the constriction and it shows turbulence of the particles as indicated by vertical movements of the particles. Particles in B appear to be less turbulent with lower velocities. In C which is part of control volume 7, the particles were

moving at average relative velocities of -0.005 and -0.006 (horizontal and vertical motions respectively). The particles then accelerated in the wave direction to an average relative horizontal velocity of +0.046 in control volume 8 (x/L = 0.49 to 0.54). The change in direction of motion occurs due to the pumping of the successive constriction. The average horizontal velocities remained positive from control volume 8 to control volume 14 and the corresponding average velocities were negative except for the control volume 13. The negative relative vertical velocities are due to the gravitational accelaration of the particles. A schematic representation of the velocity fields of the particles along the flexible tube is shown in Figure 4-45.

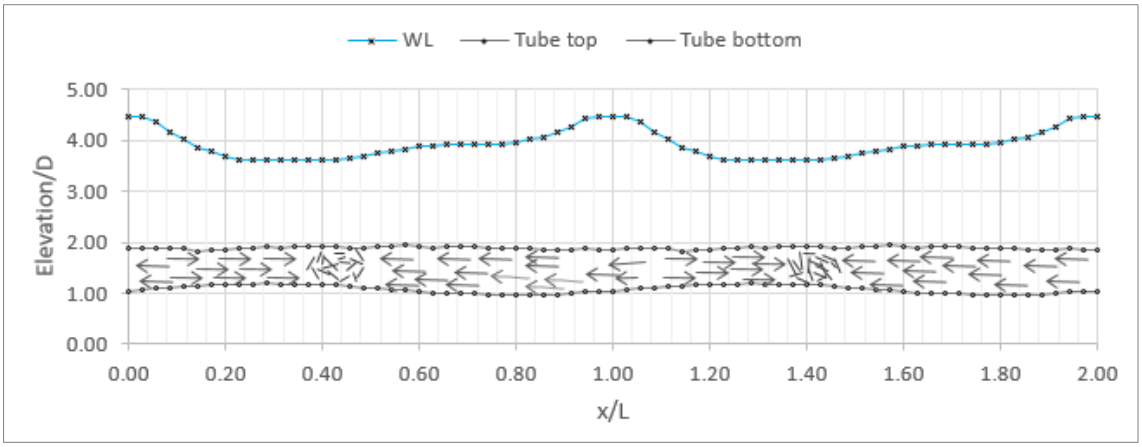

Figure 4-45 A schematic representation of the velocity field of the particles along the flexible floating tube. The arrows show the direction of the particles. Wave direction is right to left. WL is the wave surface profile, Tube top and Tube bottom are the top and bottom levels of the tube respectively.

4.6.4 The standard deviations of the root mean squares of the horizontal and vertical velocities

The standard deviations s of the root mean squares of the velocities of the particles are used (in this case) to indicate where turbulence of the particles occurs along the flexible tube. The formula for calculating s of the root mean squares of relative horizontal velocities is as follows:

$$s = \sqrt{\sum_{i=1}^{N} \frac{(u_i - \bar{u})^2}{N}} \qquad (4\text{-}3)$$

where s is the standard deviation, N is the number of particles, u_i is the velocity of a particle in the horizontal direction and $\bar{u}$ is the average horizontal velocity. Where the burst of turbulence occurrs is noticed by a rapid increase in s as shown in Figure 4-46. The standard deviations were at peak for both vertical and horizontal velocity components in the region where a burst of turbulence occurred. The standard deviations of the root mean squares of vertical velocities is calculated using the same formula but substuting u for v.

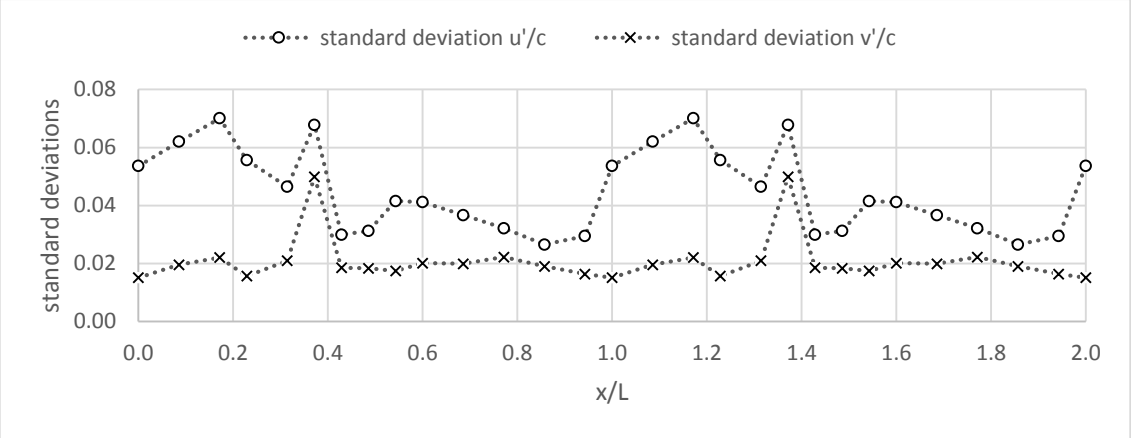

Figure 4-46 The standard deviations of the root mean squares of the horizontal (u') and vertical (v') velocities relative to the celerity of the waves. The data points were joined by dotted lines for clarity.

Peaks in standard deviations occur at positions x/L = 0.17, x/L = 0.37 and x/L = 0.54 (i.e. when one wavelength is considered). The points x/L = 0.17 and x/L = 0.37 were located just before and just after tube constrictions respectively. The point x/L = 0.54 was in the region of maximum horizontal constriction (deformation in the horizontal direction). As discussed in section 4.4.1, both vertical and horizontal deformations occur along the flexible tube. There was a rapid rise in standard deviation between x/L = 0.94 and x/L = 1.17. Between these points, occurs a gradual vertical constriction in the tube. Peak standard deviations occur at beginning and end of contrictions. No turbulence occurred in the LDPE pipes since they were not susceptible to the deformations.

4.6.5 Reynolds stresses for the velocities

The Reynolds stresses of the particles' velocities in each control volume are shown in Figure 4-47. The Reynolds stresses indicate where turbulence occurs in a fluid flow. A

peak positive Reynolds stress is noticed at x/L = 0.37 (or 1.37) i.e. exactly where the burst of turbulence occurred. This is the same location where peak standard deviation of the root mean square velocities of the particles occurred. Peak negative Reynolds stresses occurred at crests where there were the average horizontal velocities of the particles suddenly changed from positive to negative.

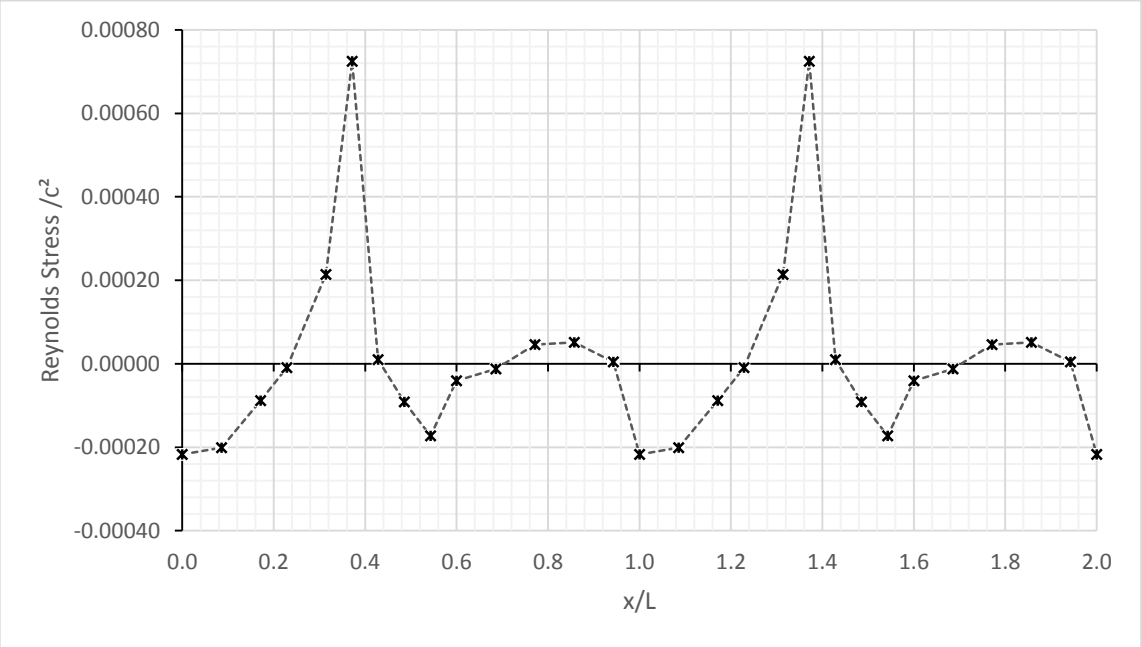

Figure 4-47 Reynolds stresses along the flexible tube (2 wave lengths). The points are joined by straight lines for clarity.

The Reynolds stresses *R* were calculated as follows:

$$R = (u - \bar{u})^*(v - \bar{v}) \qquad (4\text{-}4)$$

where u and v are the measured horizontal and vertical velocities respectively, while $\bar{u}$ and $\bar{v}$ are the average horizontal and vertical velocities respectively. The fluid particles were most stressed at the end of vertical contractions where bursts of turbulence occurred.

4.6.6 Horizontal velocity probability distributions in control volumes

This subsection presents the relative horizontal velocity probability distribution of particles in each of the 14 control volumes. The horizontal velocities V_x of polystyrene particles relative to wave celerity c are plotted against relative frequencies of the velocities. In this research, positive relative horizontal velocities are assigned to particles travelling in the wave direction (i.e. right to left) while negative velocities are for reverse motion (left to right). The horizontal velocity probability distributions of particles in each of the 14 control volumes are shown in Figure 4-48. The relative average velocities were significantly less than c in all the control volumes. The maximum velocity of the particles was less than $0.4c$.

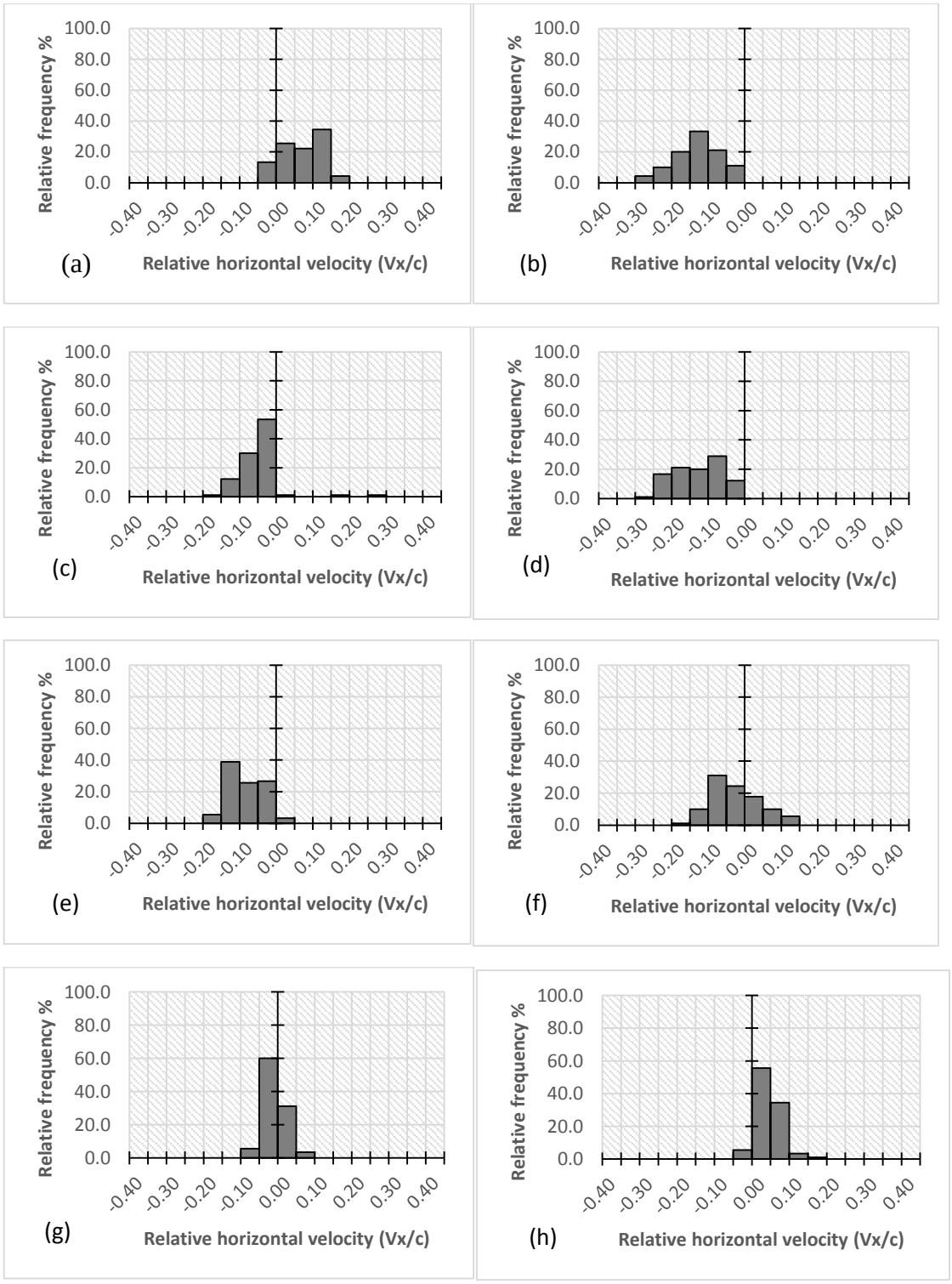

Figure 4-48 Relative horizontal velocity probability distributions of polystyrene particles in (a) control volume 1 (b) control volume 2 (c) control volume 3 (d) control volume 4 (e) control volume 5 (f) control volume 6 (g) control volume 7 (h) control volume 8.

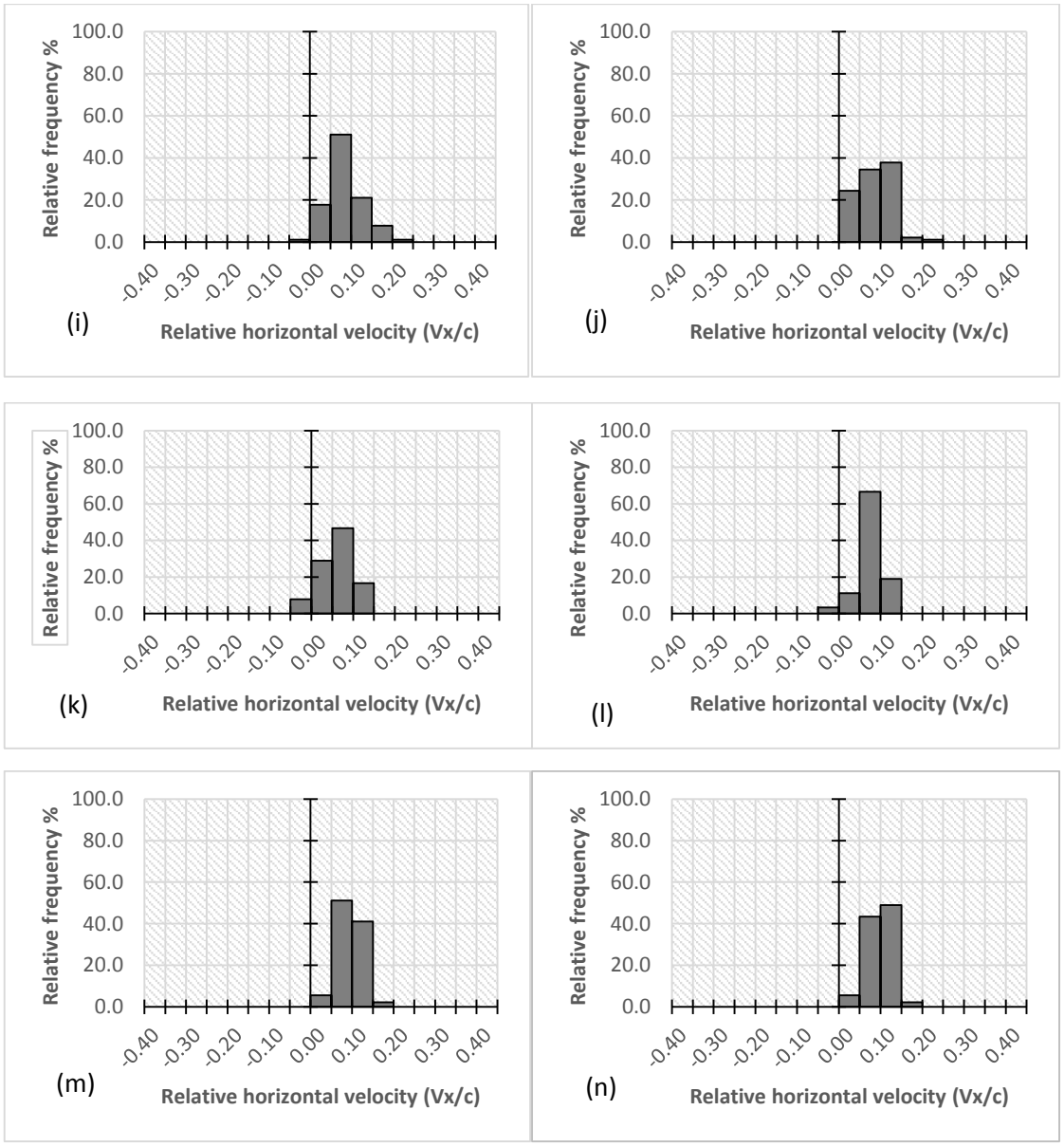

Figure 4-48(continued). Relative horizontal velocity probability distributions of polystyrene particles in (i) control volume 9 (j) control volume 10 (k) control volume 11 (l) control volume 12 (m) control volume 13 (n) control volume 14.

Figure 4-48(a) shows the probability distribution of the relative horizontal velocities of the particles in control volume 1 (i.e. from x/L = 0 to 0.09) which was located directly under the peak of the crests of the waves. In this control volume, 87 % of the particles were travelling from right to left at different velocities as shown by V_x/c and the rest were moving left to right i.e. opposite the wave direction. The average relative horizontal velocity for the particles was +0.071.

The probability distribution of relative horizontal velocities of the particles in control volume 2 (i.e. x/L = 0.09 to 0.17) is as shown in Figure 4-48(b). In this control volume, all the particles suddenly started moving left to right i.e. opposite to the wave direction. Significant vertical deformations of the tube in a wavelength were first noticed in this region. The average relative horizontal velocity was -0.129. The velocities in control volume 2 are close to a normal distribution as compared to those of control volume 1.

The probability distribution of relative horizontal velocities of the particles in control volume 3 (i.e. x/L = 0.17 to 0.23) is shown in Figure 4-48(c). All the particles were moving opposite the wave direction (i.e. left to right). The range of the relative horizontal velocities was the same as for control volume 2 but the shape of the histograms changed from a normal distribution to a ragged plateau. The average relative horizontal velocity remained at -0.129.

Figure 4-48(d) shows the velocity probability distribution of the particles in control volume 4 (i.e. x/L = 0.23 to 0.31). The mean relative horizontal velocities in control volume 3 reduced from -0.129 to -0.052 in control volume 4. About 3.3 % of the particles were moving in the wave direction. This is the region of maximum vertical constriction of the tube. The relative horizontal velocities histogram shape changed from the ragged plateau to negative-skewed.

Control volume 5 (x/L = 0.31 to 0.37) is the region within the tube's constriction just before the burst of turbulence. The average relative horizontal velocity increased from -0.052 in control volume 4 to -0.084 in control volume 5 which was due to an increase in vertical tube constriction (D_y/D). The shape of the histogram changed from negative-skewed to a ragged-plateau as shown in Figure 4-48(e).

Control volume 6 (i.e. x/L = 0.37 to 0.43) was located at the end of the tube's constriction. This is where the burst of turbulence occurred due to the sudden expansion of the flow which resulted in a rapid deceleration of the particles as mentioned earlier. There was a significant decrease in the average relative horizontal velocities of the particles from -0.084 (in control volume 5) to -0.025. Figure 4-48(f) shows a positive-skewed histogram of the relative horizontal velocities. About 33 % of the particles were moving in the wave direction. The previous control volume had only 3.3% of the particles moving in the wave direction. This was due to the turbulent flow.

A significant reduction in horizontal velocities was noticed in control volume 7 (x/L = 0.43 to 0.49) where V_x/c ranged from -0.10 to +0.10 as shown in Figure 4-48(g). Within the tube constriction, most of the particles were moving left to right i.e. opposite the wave direction but soon after the flow expansion, the number of particles travelling in the wave direction increased. The average relative horizontal velocity of particles was -0.005.

Figure 4-48(h) shows that 94 % of the particles were travelling in the wave direction in control volume 8 (x/L = 0.49 to 0.54). This is an increase from 34 % in control volume 7. Average relative horizontal velocities changed from negative to positive i.e. -0.005 (in control volume 7) to +0.046 (in control volume 8) due to the pumping of the successive constriction in the wave direction.

In control volume 9 (x/L = 0.54 to 0.60), there was a further increase in the number of particles moving in the wave direction. About 99 % of the particles were travelling in the wave direction as shown in Figure 4-48(i). The average relative horizontal velocity further increased from +0.046 to +0.088 indicating a net increase in flow in the wave direction.

Figure 4-48(j) shows the horizontal velocity distribution in control volume 10 (i.e. from x/L = 0.60 to 0.69). All the particles were moving in the wave direction. The average relative horizontal velocity was +0.087. The relative horizontal velocity probability distribution in control volume 11 (x/L = 0.69 to 0.77) is shown in Figure 4-48(k). About 8% of the particles were moving against the wave direction. The backward movement of the particles was due to a horizontal constriction in the tube. Maximum horizontal constriction occurred in this control volume. The average relative horizontal velocity further decreased from +0.087 to +0.062.

Figure 4-48(l) shows the relative horizontal velocity distribution in control volume 12 (x/L = 0.77 to 0.86). The percentage of particles moving against the wave direction decreased from 8% to 3%. The average relative horizontal velocity increased from +0.062 to +0.077. The horizontal velocity distribution for control volume 13 (x/L = 0.86 to 0.94) is shown in Figure 4-48(m). There were no particles moving against the direction of the wave. The tube's constriction in the horizontal direction ended in this control volume. The average relative horizontal velocity was +0.093.

Control volume 14 is the region just before a successive wave crest. All the particles were moving in the wave direction as shown in Figure 4-48(n). The average relative horizontal

velocity increased from +0.093 to +0.098 as the successive vertical constriction approaches. The beginning of each vertical tube constriction is associated with higher horizontal velocities.

The relative horizontal velocity distributions for all the 14 control volumes show that the motion of the particles was oscillatory but the net flow was in the forward direction i.e. the wave direction.

The average relative horizontal velocities vertically across the tube in the 14 control volumes are shown in Figure 4-49. Previously, the relative horizontal velocities V_x/c in each control volume were averaged but the velocities are not the same across the flexible tube due to shear stresses between the fluid particles and the tube and due to the changes in the direction of motion of the fluid. In uniform flows, fluid velocity is maximum at the middle of the tube and zero at the boundaries of the tube. This is not the case in peristaltic motion in flexible tube when the direction of fluid movement is changing.

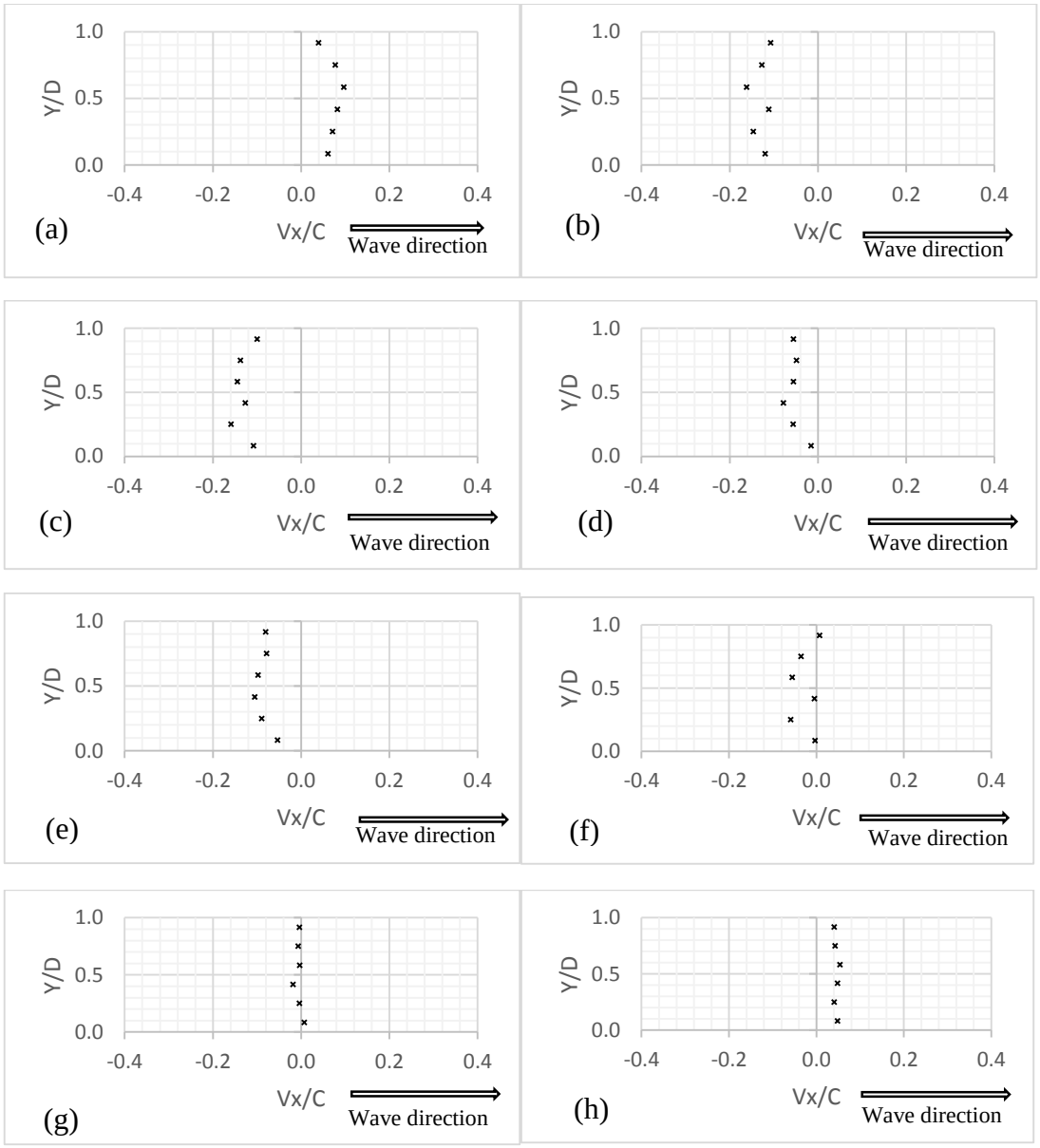

Figure 4-49 Probability distribution of horizontal velocities vertically across the flexible tube in (a) control volume 1 (b) control volume 2 (c) control volume 3 (d) control volume 4 (e) control volume 5 (f) control volume 6 (g) control volume 7 (h) control volume 8.

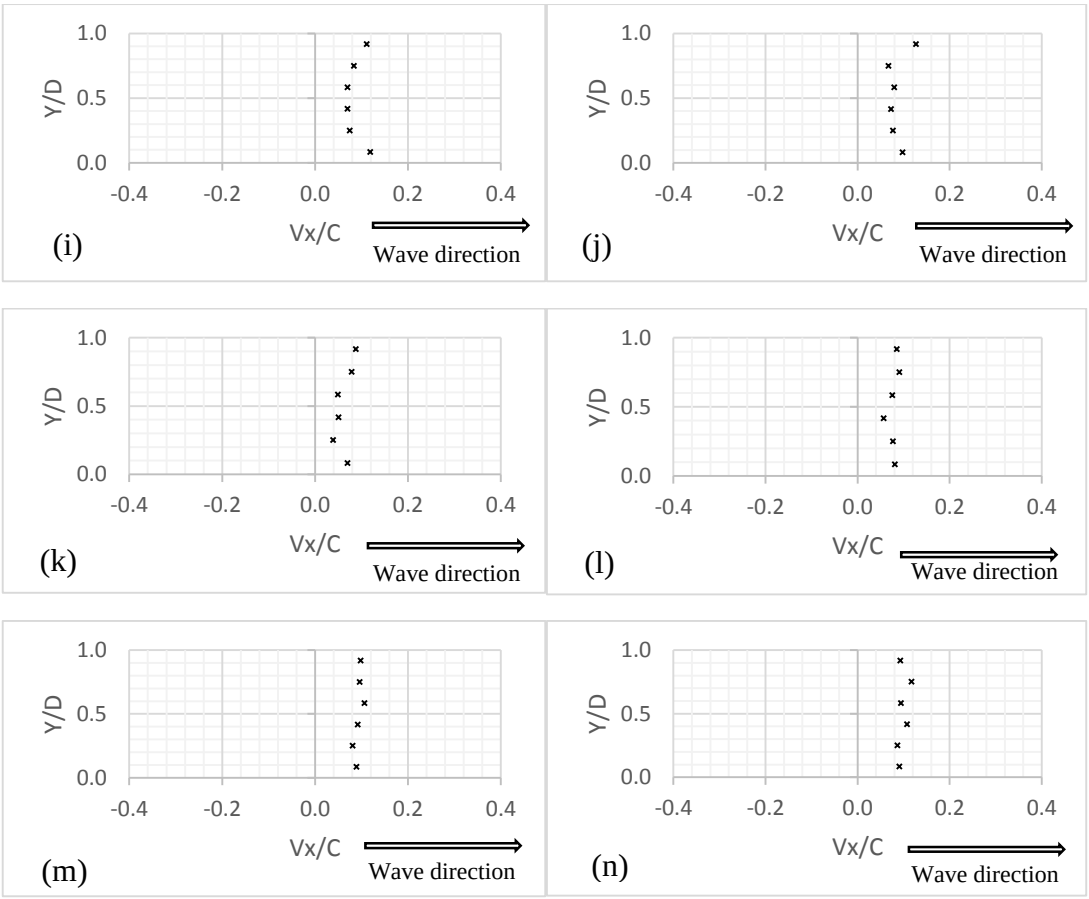

Figure 4-49(continued). Probability distribution of horizontal velocities vertically across the flexible tube in (i) control volume 9 (j) control volume 10 (k) control volume 11 (l) control volume 12 (m) control volume 13 (n) control volume 14.

4.6.7 Vertical velocity distribution in control volumes

The relative vertical velocities V_y/c in each of the 14 control volumes are presented in this sub-section. The V_y/c were plotted against the relative frequencies of the velocities. In this research, a (+) sign is for particles travelling upwards and a (-) sign for downward motion. The relative vertical velocities of the particles were significantly smaller than their corresponding relative horizontal velocities. The maximum measured vertical velocity was less than 20% of the celerity of the waves. The particles vertical velocities probability distribution in each of the 14 control volumes are presented in Figure 4-50.

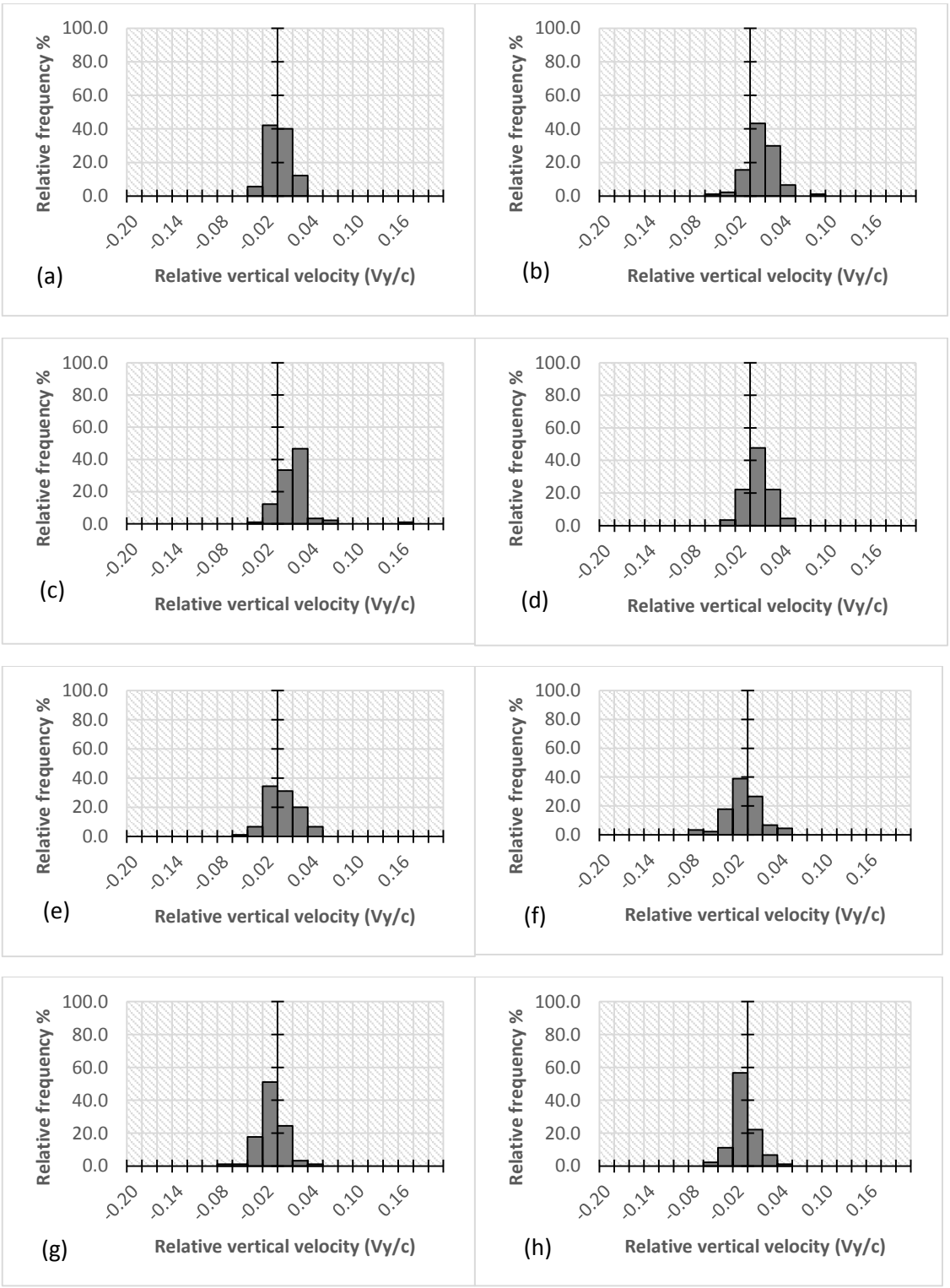

Figure 4-50 Probability distribution of relative vertical velocities of polystyrene particles in (a) control volume 1 (b) control volume 2 (c) control volume 3 (d) control volume 4 (e) control volume 5 (f) control volume 6 (g) control volume 7 (h) control volume 8.

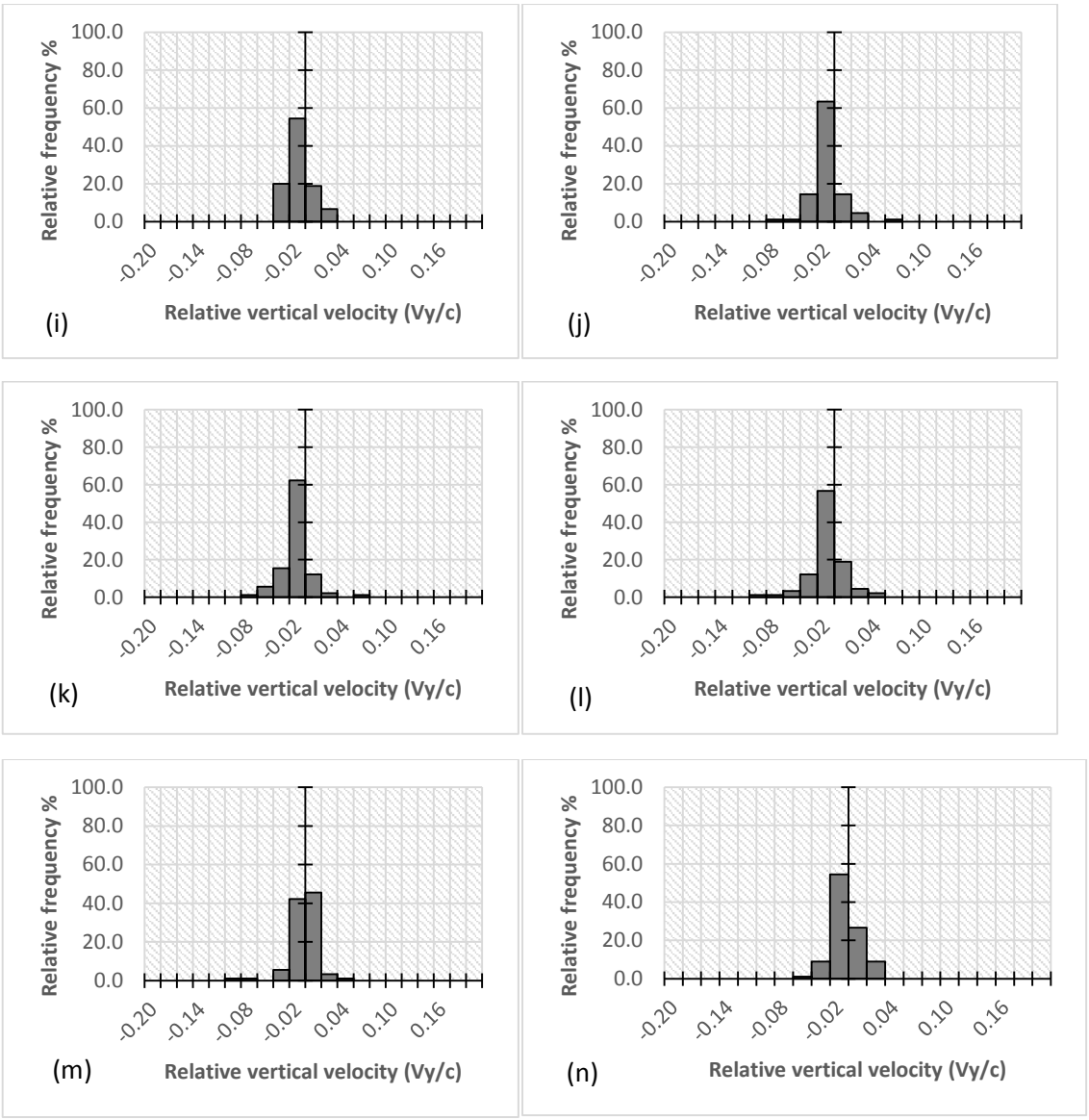

Figure 4-50(continued) Probability distribution of relative vertical velocities of polystyrene particles in (i) control volume 9 (j) control volume 10 (k) control volume 11 (l) control volume 12 (m) control volume 13 (n) control volume 14.

The probability distribution of V_y/c in control volume 1 (x/L =0.00 to 0.09) is shown in Figure 4-50(a). The particles were moving both upwards and downwards. About 48% of the particles were moving relatively downwards while the rest moving relatively upwards. The average relative vertical velocity V_y/c was +0.003. If the flow was uniform, then all the particles were expected to be moving relatively downwards due to gravity but tube distortions caused a non-uniform flow of the particles.

The relative vertical velocities in control volume 2 (x/L = 0.09 to 0.17) are shown in Figure 4-50(b). The number of particles moving upwards increased to 82%. The average relative vertical velocity also increased from +0.003 to +0.017. None of the particles were travelling at V_y/c between +0.06 and +0.08. This could have been caused by the limited number of particles used for the analysis or due to the presence of outlier particles.

In control volume 3 (i.e. from x/L = 0.17 to 0.23), 87% of particles were moving relatively upwards as shown in Figure 4-50(c). The average relative vertical velocity of the particles in control volume 3 was +0.023. Figure 4-50(d) shows the probability distribution of V_y/c of particles in control volume 4 (x/L = 0.23 to 0.31). The probability distribution is bell shaped but shifted to the right indicating that there are more particles (75%) moving upwards than downwards. Maximum vertical deformations of the tube occur in this region as discussed in the previous sub-section.

Figure 4-50(e) shows the probability distribution of the relative vertical velocities of the particles in control volume 5 (i.e. x/L = 0.31 to 0.37). About 42 % of the particles were moving relatively downwards while the rest were moving upwards. The probability distribution of the relative vertical velocities in control volume 6 (i.e. from x/L = 0.37 to 0.43) is shown in Figure 4-50(f) with 62% of the particles moving relatively downwards. About 65.5% of the particles were moving at relative velocities V_y/c between -0.02 and +0.02. This is the control volume where the tube's vertical constriction ended resulting in a sudden expansion in flow causing a burst of turbulence. The average relative vertical velocity of the particles was +0.001.

Turbulent motion of the particles also occurred in control volume 7 (x/L = 0.43 to 0.49). The relative vertical velocity distribution V_y/c in control volume 7 is shown in Figure 4-50(g). Seventy-one percent of the particles were moving relatively downwards resulting in negative average relative vertical velocity of the particles. The downward motion of the particles was due to gravity. The relative vertical velocities of the particles in control volume 8 (i.e. from x/L = 0.49 to 0.54) are shown in Figure 4-50(h). Seventy percent of the particles were moving downwards. The average relative vertical velocity decreased from -0.006 (control volume 7) to -0.003 due to the turbulent motion.

The relative vertical velocities of the particles in control volume 9 (x/L = 0.54 to 0.60) are shown in Figure 4-50(i). About 74 % of the particles were moving downwards and the average relative vertical velocity increased from -0.003 to -0.007. This is the control

volume when the seeded particles started moving in the wave direction. The flow was more uniform so the particles' motion was relatively downward due to the force of gravity. Tube constrictions often force some of the particles to move upwards. The relative vertical velocity probability distribution of the particles in control volume 10 (x/L = 0.60 to 0.69) is shown in Figure 4-50(j). There was a further increase in the number of particles moving relatively downwards from 74% to 80% as the flow gets more uniform. The average relative vertical velocity of the particles was -0.007 as the flow expanded. There was an increase in average relative vertical velocity (downwards) in control volume 11 (x/L = 0.69 to 0.77) from -0.007 to -0.011. There was also an increase in the number of particles moving relatively downwards from 80% to 85% in Figure 4-50(k).

The relative vertical velocity distribution in control volume 12 (i.e. x/L = 0.77 to 0.86) is shown in Figure 4-50(l). The average relative velocity decreased from -0.011 to -0.009. About 74% of the particles were moving in the downward direction. Figure 4-50(m) shows the relative vertical velocity distribution for control volume 13 (x/L = 0.86 to 0.94). About 50% of the particles were moving upwards and the average relative vertical velocity was +0.001. The increase in average upward velocity was due to horizontal constriction within the tube.

The percentage of particles moving relatively upwards decreased from 50% to 36% in control volume 14 (x/L = 0.94 to 1.00) since the flow was more uniform and gravity was the main force acting on the particles. The relative vertical velocity distribution for control volume 14 is shown in Figure 4-50(n). The average relative vertical velocity for particles in control volume 14 was -0.002. The results of the relative velocities of the particles in each of the 14 control volumes show that the tube deformations affect the velocities of the fluid particles along the flexible tube. In uniform flows, particles are expected to move forward and relatively downwards due to gravitational force but tube deformations and turbulence forced some of the fluid particles to move relatively upwards.

4.7 Measured flow compared to calculated flow

The average flow of the water in the tube was the same at any point since there were no water losses and water is effectively incompressible at low accelerations. This is the basis of continuity equation which is given as follows:

$$A_1 v_1 = A_2 v_2 \qquad (4\text{-}5)$$

where A_1 and A_2 are cross-sectional areas of fluid flow at any locations 1 and 2 respectively while v_1 and v_2 are the fluid velocities at the same locations 1 and 2 respectively. The area of an ellipse is $A = \pi \frac{D_y}{2} \frac{D_z}{2}$. When D_y and D_z are equal, the ellipse becomes a circle.

The calculations of flow rates are summarised in Table 4-2.

Table 4-2 Average flow calculations using continuity formula

Control volume	Average Area, $\bar{A}_i\ (mm^2)$	Δx_i *(mm)*	Average Velocity, $\bar{v}_i\ (mm/s)$	$\bar{v}_i \bar{A}_i \Delta x_i$ $(mm/s.\ mm^2)$
1	684.5	128.6	+76.8	+6758.9
2	704.1	128.6	-139.5	-12628.5
3	705.0	85.7	-139.6	-8435.8
4	704.3	128.6	-56.1	-5080.0
5	704.3	85.7	-91	-5493.5
6	704.3	85.7	-27	-1630.0
7	705.0	85.7	-5.4	-326.3
8	701.5	85.7	+49.3	+2964.3
9	696.2	85.7	+95.0	+5669.1
10	688.5	128.6	+93.6	+8285.6
11	696.2	128.6	+67.3	+6024.1
12	702.5	128.6	+83.7	+7559.9
13	703.8	128.6	+100.9	+9130.3
14	688.6	85.7	+105.8	+6244.6
			Average $\bar{Q}$*(ml/s)*	+12.7 *ml/s*

Average flow is given as follows:

$$\bar{Q} = \frac{1}{L} \sum_{i=1}^{N} \bar{v}_i \bar{A}_i \Delta x_i \qquad (4\text{-}6)$$

where N is the total number of control volumes and L is the wavelength which was 1500mm. In this experiment, the calculated average flow rate $\bar{Q}$ was +12.7ml/s. The measured average flow for this experiment was + 11.9 *ml/s* with a wave height *H* of 36*mm* (refer to Figure 4-9 at *H/D* = 1.2). The calculated flow differs by 6.7 % from the measured flow. Errors may have occurred due to the assumptions made in calculating the cross-sectional areas of the flexible tube using Sykora (2004)'s formula. The tube's cross-section was assumed to deform into an elliptical shape and this was to done to simplify the calculations.

4.8 Scaling analysis to deduce characteristics of full scale prototypes

Dimensional analysis is important in deducing the characteristics of full scale prototypes. All the testing is done on the model before a prototype can be built. Similarity formulae such as Froude numbers can be used for the dimensional analysis. In this case Froude number will be used for the model and prototype comparisons. Froude number is given as:

$$F = \frac{v}{\sqrt{gD}} \qquad (4\text{-}7)$$

where v is a velocity scale, D is a length scale and g is the gravitational acceleration. The subscripts 1 and 2 will be used for the model and prototype respectively.

F = $\frac{v_1}{\sqrt{gD_1}} = \frac{v_2}{\sqrt{gD_2}}$ which is equal for both the model and prototype. Squaring both side gives $\frac{v_1^2}{gD_1} = \frac{v_2^2}{gD_2}$ and rearranging gives:

$$\frac{D_1}{D_2} = \left(\frac{v_1}{v_2}\right)^2 \qquad (4\text{-}8)$$

The velocity scales can also be expressed in term of the length scales as follows:

$$\frac{v_1}{v_2} = \left(\frac{D_1}{D_2}\right)^{\frac{1}{2}} \qquad (4\text{-}9)$$

The ratio $\frac{T_1}{T_2}$ where T_1 and T_2 are the model and prototype time scales respectively is given as $\frac{T_1}{T_2} = \frac{D_1/v_1}{D_2/v_2}$ (since *T = displacement/velocity*). The ratio can also be written as:

$$\frac{T_1}{T_2} = \frac{D_1}{D_2} \, x \, \frac{v_2}{v_1} \qquad (4\text{-}10)$$

Substituting $\frac{v_1}{v_2}$ (in equation 4.9) into equation 4.10 gives $\frac{T_1}{T_2} = \frac{D_1}{D_2} \, x \, \left(\frac{D_2}{D_1}\right)^{\frac{1}{2}}$ which simplifies to $\frac{T_1}{T_2} = \left(\frac{D_1}{D_2}\right)^{\frac{1}{2}}$. The time scale ratio can be used to estimate residence time for the prototype. In order to calculate the time scale ratio, the length scale ratio must be known. For the experiment conducted the model wave height H_1 was = 36*mm.* Assuming an average ocean wave height H_2 of $1800mm$ gives a length scale ratio which is calculated as follows:

$\frac{H_1}{H_2} = \frac{36}{1800} = \frac{D_1}{D_2} = \frac{30}{1500} = \frac{1}{50}$. Therefore, the length scale ratio is taken as $\frac{1}{50}$. The residence time for the prototype T_2 is calculated using:

$$T_2 = T_1 * \left(\frac{D_2}{D_1}\right)^{\frac{1}{2}}. \qquad (4\text{-}11)$$

The residence time T_1 for the model is calculated using equation 4.12 as follows:

$$T_1 = \frac{V}{Q} \qquad (4\text{-}12)$$

where V is the volume of water in the flexible tube and Q is the average flow rate around the FTPBR system. The volume of water in the model flexible tube of length of 6250*mm* and diameter of 30*mm* was approximately equal to $\frac{\pi 30^2}{4} x 6250$ = 4.42x 10^6 mm^3. The average flow rate through the tube was 11.9 ml/s. Dividing the volume of water in the tube by the average flow rate gives the model residence time $T_1 \approx$ 371 seconds i.e. 6.2 minutes. T_2 was then found to be approximately 6.2 $x\sqrt{50}$ = 44 minutes. This is the estimated residence time of wastewater in a prototype FTPBR of diameter 1500*mm* and length 6.25*50 = 313*m*.

Flow rate through the system $Q = vA$ by continuity of flow. The ratio of model flow Q_1 to prototype flow Q_2 is given by $\frac{Q_1}{Q_2} = \frac{v_1 A_1}{v_2 A_2}$. Expressing v and A in terms of the length scale D gives $\frac{Q_1}{Q_2} = \left(\frac{D_1}{D_2}\right)^{\frac{1}{2}} \left(\frac{D_1}{D_2}\right)^2$ which simplifies to:

$$\frac{Q_1}{Q_2} = \left(\frac{D_1}{D_2}\right)^{\frac{5}{2}} \quad (4\text{-}13)$$

Q_2 can then be expressed in terms of Q_1 as:

$$Q_2 = \left(\frac{D_2}{D_1}\right)^{\frac{5}{2}} x\, Q_1 \quad (4\text{-}14)$$

Q_2 can be estimated by substituting $\frac{D_2}{D_1}$ with the length scale ratio as

$Q_2 = \left(\frac{50}{1}\right)^{\frac{5}{2}} * Q_1$ which gives $Q_2 \approx (50)^{\frac{5}{2}} * 11.9\, ml/s$ = 210*l/s* = 18.2 Ml/day. If a discharge for a coastal city is 150 Ml/day then the waste water treatment plant requires about 9 of these flexible tubes with diameters of 1500*mm* and length of 315*m.*

CHAPTER 5 : CONCLUSIONS AND RECOMMENDATIONS

5.1 Conclusions

The broad objective of this project was to contribute to developing a system for microalgae cultivation as a feedstock for biofuel production. A simple photo-bioreactor system consisting of a flexible tube (FTPBR) for algae cultivation was built. A piston paddle wave generator and a wave tank were the physical modelling tools for the laboratory experiments for this research. The results of the experiments gave both qualitative and quantitative structure of the fluid particles' flow fields in flexible tubes influenced by progressive waves of various characteristics (e.g. wave height, water depth, frequency etc.) together with the pumping characteristics of these wave- driven systems. Simplified progressive narrow-band ocean waves of different characteristics were simulated by varying wave frequency f, the paddle stroke S and the water depth h. Varying S and h have the most effect on the wave height H which depends on the volume of fluid displaced in 1 stroke of the piston paddle of the wave generator. The performance of the wave generator was consistent with the shallow water wave theory (Biesel and Suquet, 1951) and with the results summarised by Dean and Dalrymple (2010) who showed that the ratio (H/S) / $K_p h$ (where the wave number $K_p = 2\pi/L$ with L the wavelength) is approximately equal to 1 for shallow water waves. A linear relationship between H/S and $K_p h$ was obtained from the waves tested in the present experiments so the wave generator was therefore 'fit for purpose' i.e. suitable for simulating simplified waves in the regime of interest.

The generation of sinusoidal waves was limited by still water depth h of the wave flume which had a total height of 200mm and the maximum frequency of the available wave generator. Increasing frequency of the waves results in the waves changing gradually from cnoidal to sinusoidal if they are deep enough. Cnoidal waves are generated at water depth h less than a tenth of the wavelength L (Wiegel, 1959). The celerity c of shallow water waves is dependent on the water depth h.

Interference of the flexible tube with the waves causes attenuation of the waves which has negative effects on the wave energy and wave height. The interaction of the waves with the walls of the flume also contributed to the attenuation of waves. The attenuation

of the waves decreases with increase in depth of the tube from the surface of waves since the influence of the waves on the tube reduces with depth. Wave parameters as well as the average tube position and the internal pressure of polyethylene flexible tubes containing water affect the deformation of the tubes in progressive water waves. Wave-induced pressures deform flexible tubes non-uniformly along their length. Wave-induced pressures consist of two components i.e. hydrostatic and dynamic pressures. Hydrostatic pressures increase with water depth h while dynamic pressures are created due to the displacement of wave surface. Progressive waves create dynamic waves of area change along the flexible tube pumping fluid (water) in the wave direction. The flow is analogous to peristalsis of substances in vascular systems. Flow rate increases with wave height H since wave energy is directly proportional to wave amplitude squared (see e.g. Dean and Dalrymple, 2010). The wave height H increases with frequency f but flow rate increases with H at constant f. This implies that flows through flexible tubes are mainly influenced by H and that f has little effect on the flow rate. At constant celerity, lower frequencies produce larger pulses of flow whereas higher frequencies produce smaller but more pulses of flow in the same time τ at constant H. In other words, approximately the same volume of water flows at constant H and time τ but the size of the pulses depends on the wave frequency. Flow rate increases with depth of the flexible tube from the free surface of the waves, but there is a limit to this effect since the wave-induced pressure perturbations also decay with depth below the free surface.

Flexible tubes are deformed when the internal pressures of water are less than the external wave-induced pressures. The tube deformations decrease with increase in internal pressure of the tube as the waves require more energy to deform the tube. The residence time of fluid particles increases with decrease in flow rate. Residence time in this research is the average amount of time a fluid particle spends in the flexible tube. The residence time is important in microalgae cultivation in determining how much time is required for microalgae cells to flow around the FTPBR system before they can be harvested.

Particle tracking velocimetry (PTV) was used track the motion of the seeded polystyrene particles. PTV uses the displacements and exposure time of particles in two successive image frames to depict the particles' flow fields and their velocities. The motion of polystyrene tracer particles seeded in flexible tubes characterised the actual flow fields of fluid particles in flexible tubes. The particles in the flexible tube had an oscillatory motion

but with a net flow in the direction of waves. In uniform flows, particles move relatively forward and relatively downwards due to gravitational force but constrictions in the flexible tube force some particles to move upwards and backwards. Bursts of turbulence occurred at the end of every constriction of the flexible tube due to a sudden expansion of flow which caused rapid deceleration of particles. A constriction in the flexible tube pushes the fluid ahead of it in the wave direction but it also allows backward movement of fluid through itself. The turbulence is also noticed by a sudden increase in standard deviations in velocities of the particles as well as the Reynolds stresses. Even though the flow is oscillatory there is net flow in the wave direction. No turbulence was observed in the LDPE pipes since they are not susceptible to wave-induced pressure deformations. Froude number scaling can be used to establish geometric similarities between the laboratory model and full-scale prototypes.

5.2 Recommendations

Biofuels are renewable energy sources which can potentially replace non-renewable fossil fuels. There is need to develop efficient FTPBRs for algae cultivation as a feedstock for biofuel production, wastewater treatment and CO_2 sequestration. Since there are various species of algae, the choice depends on their growth rates, oil content and availability. FTPBR can allow for the cultivation of specific species of microalgae and this is not possible in ponds. The costs of producing biofuels are minimised by using cheap inputs such as wastewater discharges as a source of nutrients, CO_2 (from power plants and industries) and solar energy which. These are readily available at little or no cost. The operational processes such as pumping, mixing and harvesting of the microalgae are powered by ocean waves. The turbulence caused inside flexible tubes by ocean waves enhances the availability of nutrients to the microalgae cells. There is need for further studies on the effects of flow rates and turbulence on the growth of microalgae in FTPBRs in order to establish optimum conditions for operating these bioreactors. Modern day PTV or PIV equipment should be used for flow field measurements in order to get more accurate results about the fluid particles flow.

The research can be improved by simulating a larger range of typical ocean waves in the laboratory by increasing the depth of the wave flume and the frequency of the wave

generator. The sunlight intensity is maximum at the surface of the waves and reduces with depth. This should be the main factor when choosing the depth of flexible tubes from the free surface of the waves since microalgae cells need sunlight for photosynthesis. The diameter of the flexible tubes must be limited to allow sunlight to penetrate to the bottom of the tubes so that all the algae cells receive the sunlight. The tubes must be durable enough so that there is no need to replace them frequently since this disturbs the microalgae cultivation processes. The stiffness of the tubes can be increased by braiding the tubes with fibre (Pinnington, 1997). The length of the tubes must also be limited to reduce the accumulation of oxygen which is a by-product of photosynthesis and its presence inhibits the primary production of microalgae. The width of the wave flume was limited to 180*mm* which gave no room to change the angle of incident of the waves on the flexible tubes. Typical ocean waves can approach an obstacle at any angle. The tubes can be lowered to protect them against harsh wave conditions since the influence of waves reduces with water depth. In that case, the internal pressure of the tube can also be increased to reduce the flow through the tube.

REFERENCES

Biesel, F. and Suquet, F. 1951. Les Appareils Generateurs de Houle en Laboratoire. *La Houille Blanche*, 6(2), pp. 147-165.

Brennan, L. and Owende, P. 2010. Biofuels from Microalgae-A Review of Technologies for Production, Processing, and Extractions of Biofuels and Co-Products. *Renewable and Sustainable Energy Reviews*, 14 (2), pp. 557–577.

Chaplin, J. R., Heller, V., Farley, F. J. M., Hearn, G. E. and Rainey, R. C. T. 2012. Laboratory Testing the Anaconda. *Philosophical Transactions of Royal Society*, 370, pp. 403–424.

Chappell, E.R. 1969. *Theory and design of a wave generator for a short flume.* Master of Applied Science, Department of Civil Engineering, University of British Columbia, Canada.

Cheng, N. S. 1997. Effect of Concentration on Settling Velocity of Sediment Particles. *Journal of Hydraulic Engineering*, 123(8), pp. 728-731.

Chisti, Y. 2007. Biodiesel from Microalgae. *Biotechnology Advances.* 25(3), pp. 294–306.

Cowen, E. A., Chang, K. A. and Liao, Q. 2001. A Single-Camera Coupled PTV–LIF Technique. *Experiments in Fluids*, 31(1), pp. 63-73.

Cowen, E.A. and Monismith, S. G. 1997. A Hybrid Digital Particle Tracking Velocimetry Technique. *Experiments in Fluids*, 22, pp. 199-211.

Dean, R.G. and Dalrymple, R.A. 2010. *Water Wave Mechanics for Engineers and Scientists.* London: World Scientific Publishing Co. Pty. Ltd.

Dietrich, W.E. 1982. Settling Velocity of Natural Particles. *Water Resources Research*, 18(6), pp. 1615-1626.

Feng, Y., Goree, J. and Liu, B. 2011. Errors in Particle Tracking Velocimetry with High-Speed Cameras. *Review of Scientific Instruments*, 82(5), 053707. [Online]

Available at: http://dusty.physics.uiowa.edu/~goree/papers/Feng_RSI_2011-PTV-errors-high-speed-cameras-reprint.pdf [Accessed 12 October 2015].

Grotberg, J.B. and Jensen, O.E. 2004. Biofluid Mechanics in Flexible Tubes. *Annual Review of Fluid Mechanics,* 36, pp. 121-147.

Hayat, H., Wang, Y., Siddiqui A.M., Hutter, K. and Asghar, S. 2002. Peristaltic Transport of a Third-Order Fluid in a Circular Cylindrical Tube. *Mathematical Models and Methods in Applied Sciences,* 12, pp. 1691-1706.

Hoel, M. and Kvemdokk, S. 1996. Depletion of Fossil Fuels and the Impacts of Global Warming, *Resource and Energy Economics* 18, pp. 115-136.

Hoffmann, J.P. 1998. Wastewater Treatment with Suspended and Nonsuspended Algae. *Journal of Phycology,* 34, pp. 757-763.

Hughes, S.A. 1993. Physical Models and Laboratory Techniques in Coastal Engineering. London: World Scientific Publishing Co. Pte. Ltd.

Jensen, O. 2013. Instabilities of flows through deformable tubes and channels. In: Denier, J.P. and Finn, M.D. ed. *Mechanics Down Under*. Springer Netherlands. pp.101-116.

Kane, J.W. and Sternheim, M.M. 1983. *Physics*. 2nd ed. New York: John Wiley & Sons, Inc.

Lee, Y.K. and Hing, H.K. 1989. Supplying CO_2 to Photosynthetic Algal Cultures by Diffusion Through Gas-Permeable Membranes. *Applied Microbiology and Biotechnology,* 31(3), pp. 298-301.

Madsen, O. S. 1970. Waves Generated by a Piston-type Wavemaker. *Coastal Engineering Proceedings,* 1 (12), pp. 589-607.

Massey, B.S. 1983. *Mechanics of fluids.* 5th ed. Berkshire: Van Nostrand Reinhold (UK) Co. Ltd.

Mata, T.M., Martins, A.A. and Caetano, N.S. 2010. Microalgae for Biodiesel Production and other Applications: A Review. *Renewable and Sustainable Energy Reviews*, 14, pp. 217–232.

Misra, J. C. and Pandey, S. K. 2001. A Mathematical Model for Oesophageal Swallowing of a Food-Bolus. *Mathematical and Computer Modelling,* 33, pp. 997-1009.

Muthu, P., Kumar, B.V.R. and Chandra, P. 2001. Peristatic Motion in Circular Cylindrical Tubes: Effect of Wall Properties. *Indian Journal of Pure and Applied.* 32(9), pp. 1317-1328.

Muthu, P., Kumar, B.V.R. and Chandra, P. 2008. Peristaltic Motion of Micropolar Fluid in Circular Cylindrical Tubes: Effect of Wall Properties. *Applied Mathematical Modelling*, 32(10), pp. 2019–2033.

Ohmi, K. and Li, H. 2000. Particle-Tracking Velocimetry with new Algorithms. *Measurement Science Technology*, 11(6), pp. 603–616.

Park, J.B.K., Craggs, R.J. and Shilton, A.N. 2011. Wastewater Treatment High Rate Algal Ponds for Biofuel Production. *Bioresource Technology,* 102 (1), pp. 35–42.

Patil, V., Tran, K. and Giselrød, H. R. 2008. Towards Sustainable Production of Biofuels from Microalgae. *Int. J. Mol. Sci. 9*(7), pp. 1188-1195.

Phillips, O.M. 1977. *The Dynamics of the Upper Ocean*. 2nd ed. London: Cambridge University Press.

Pinnington, R J. 1997. The Axisymmetric Wave Transmission Properties of Pressurized Flexible Tubes. *Journal of Sound and Vibration,* 204(2), pp. 271-289.

Powlson, D.S., Riche, A.B. and Shield, I. 2005. Biofuels and Other Approaches for Decreasing Fossil Fuel Emissions from Agriculture. *Annals of Applied Biology* 146, pp. 193-201.

Richmond, A. 2004. *Handbook of Microalgal Culture: Biotechnology and Applied Phycology*. Oxford: Blackwell Science Ltd.

Shen, J. and Haas, L. 2004. Calculating Age and Residence Time in the Tidal York River Using Three-Dimensional Model Experiments. *Estuarine, Coastal and Shelf Science*, 61(3), pp. 449–461.

Smith, E. Q. 1983. *Energy Device Powered by the Motion of Water Beneath Waves,* U.S. Patent 4371788 A.

Sýkora, S. 2005. On the Circumference of Ellipses and Novel Approximations for the Complete Elliptic Integral E(x), Castano Primo, Italy. [Online] Available at: http://www.ebyte.it/library/docs/math05a/EllipseCircumference05.html [Accessed 12 September 2015].

Telleen, J., Sullivan, A., Yee, J., Wang, O., Gunawardane, P., Collins, I., and Davis, J. 2007. Synthetic Shutter Speed Imaging. *In: Computer Graphics Forum*, 26(3), pp. 591-598.

Wang,L.P. and Maxey, M.R. 1993. Settling Velocity and Concentration Distribution of Heavy Particles in Homogeneous Isotropic Turbulence. *Journal of Fluid Mechanics,* 256, pp. 21-68.

Westerweel J. 1997. Fundamentals of Digital Particle Image Velocimetry. *Meas. Sci. Technol.* 8, pp. 1379–1392.

Wiegel R. L. 1959. A Presentation of Cnoidal Wave Theory for Practical Application. *Journal of Fluid Mechanics*, 7(2), pp. 273- 286.

Umeyama, M. Shintani, T and Watanabe, S. 2010. Measurements of Particle Velocities and Trajectories in a Wave Current Motion Using PIV and PTV, *Proceedings of the 32nd International Conference on Coastal Engineering, ASCE, Waves 2*. [Online] Available at: http://dx.doi.org/10.9753/icce.v32.waves.2 [Accessed 10 Oct. 2015].

Xiao, Q. and Damodaran, M. 2002. A Numerical Investigation of Peristaltic Waves in Circular Tubes. *International Journal of Computational Fluid Dynamics*, 16(3), pp. 201-216.

APPENDICES

Appendix A Methodology

Table A-1 The diameters and the radii of 25 polystyrene particles measured using a Nikon inverted microscope and the NIS software.

Particle	Radius (μm)	Diameter (μm)
1	567.96	1135.92
2	576.81	1153.62
3	614.98	1229.96
4	643.39	1286.78
5	638.64	1277.28
6	548.70	1097.40
7	602.33	1204.66
8	638.38	1276.76
9	623.17	1246.34
10	622.75	1245.50
11	649.87	1299.74
12	647.28	1294.56
13	597.83	1195.66
14	686.06	1372.12
15	624.82	1249.64
16	576.43	1152.86
17	630.97	1261.94
18	532.08	1064.16
19	545.54	1091.08
20	707.65	1415.30
21	690.62	1381.24
22	595.45	1190.90
23	538.75	1077.50
24	554.81	1109.62
25	577.42	1154.84
Mean	609.64	1218.62
Standard deviation	47.38	94.77

Appendix B Results

The Figures B-1, B-2, B-3 and B-4 show the effect of frequency on the flow rates and the geometric distortions of the flexible tube. The flow rate and the rate of the geometric distortions increase with frequency. Further increase in frequency causes the rise (displacement) of the mid-section of the flexible tube from its initial position.

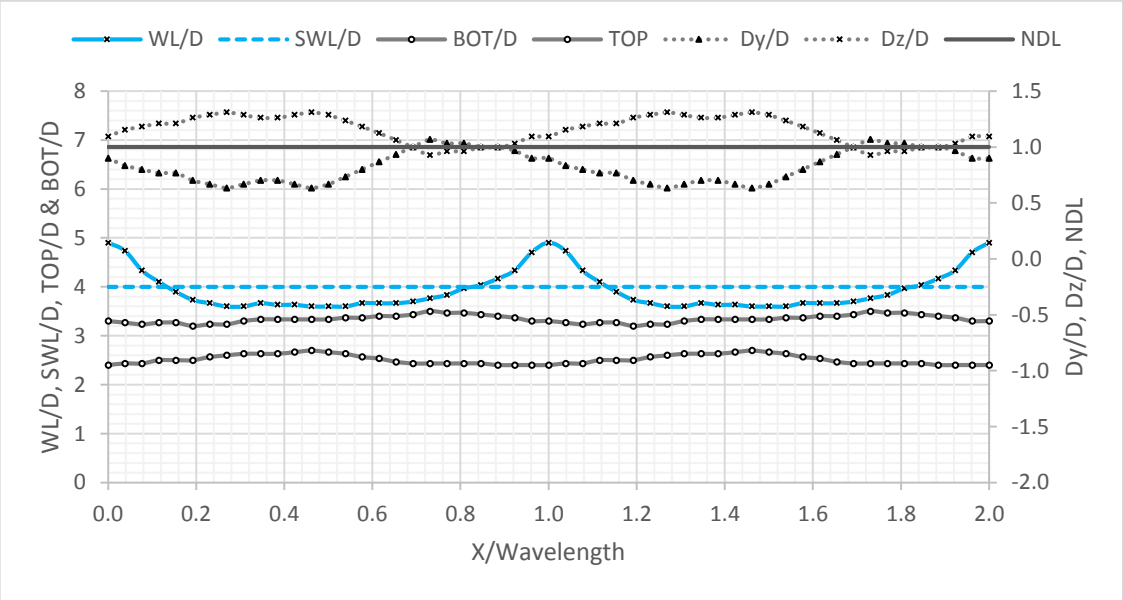

Figure B-1 *Tube deformation along the flume as the ratios D_y/D and D_z/D for vertical and horizontal deformations respectively at a frequency of 0.95Hz, a flow rate of 20.0ml/s and pressure head of 0mm. SWL and NDL are the 'still water level' and 'no deformation line' respectively. BOT/D and TOP/D are the relative bottom and top elevations respectively.*

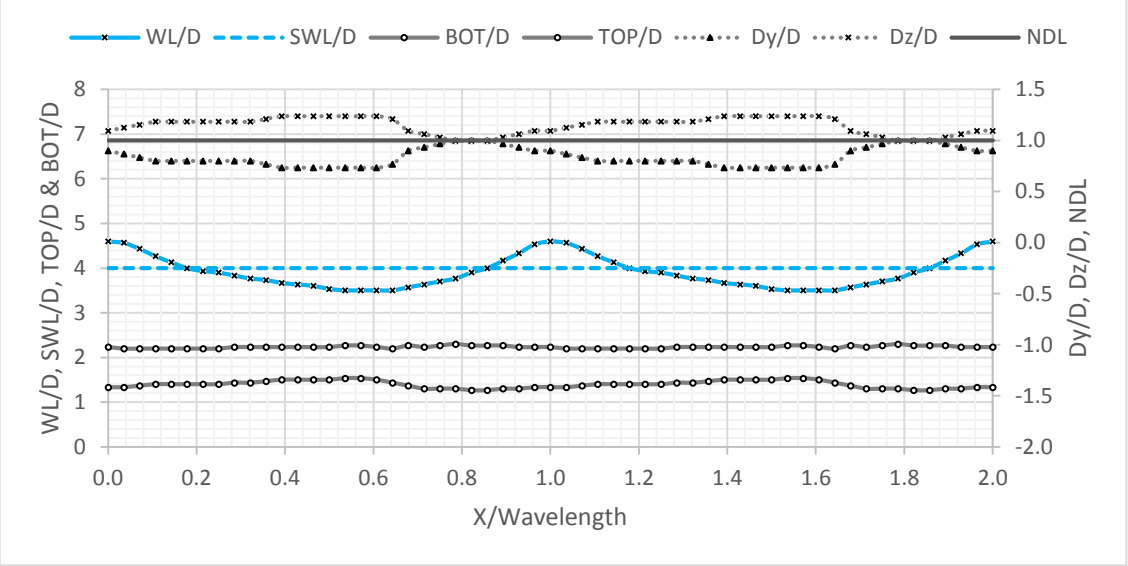

Figure B-2 *Tube deformation along the flume as the ratios D_y/D and D_z/D for vertical and horizontal deformations respectively at a frequency of 0.86Hz, a flow rate of 10.7ml/s and pressure head of 0mm. SWL and NDL are the 'still water level' and 'no deformation line' respectively. BOT/D and TOP/D are the relative bottom and top elevations respectively.*

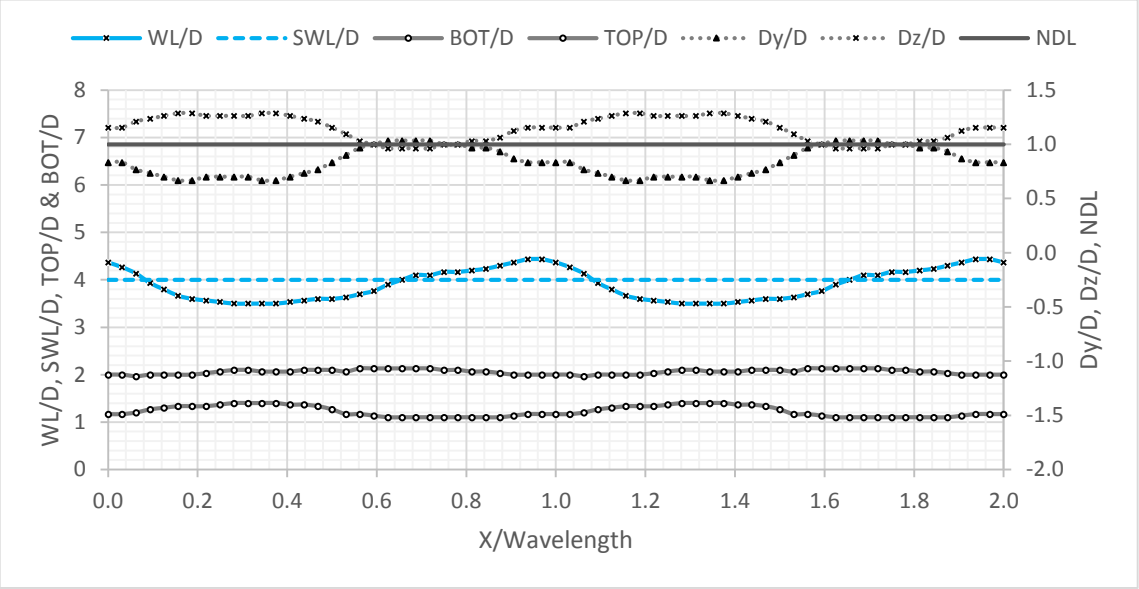

Figure B-3 *Tube deformation along the flume as the ratios D_y/D and D_z/D for vertical and horizontal deformations respectively at a frequency of 0.75Hz, a flow rate of 9.10 ml/s and pressure head of 0mm. SWL and NDL are the 'still water level' and 'no deformation line' respectively. BOT/D and TOP/D are the relative bottom and top elevations respectively.*

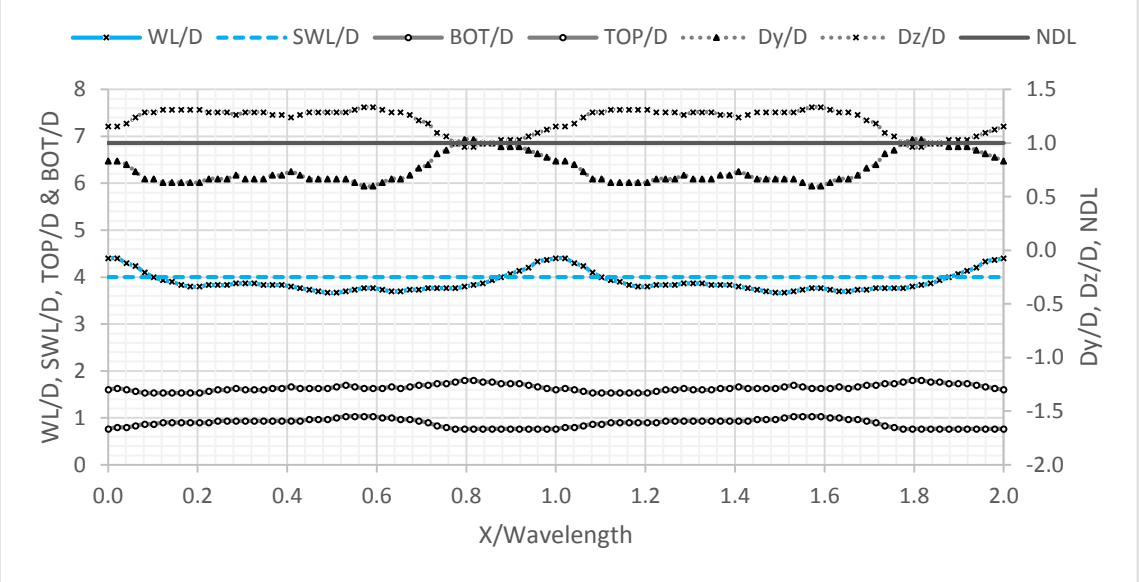

Figure B-4 *Tube deformation along the flume as the ratios D_y/D and D_z/D for vertical and horizontal deformations respectively at a frequency of 0.47Hz, a flow rate of 8.0ml/s and pressure head of 0mm. SWL and NDL are the 'still water level' and 'no deformation line' respectively. BOT/D and TOP/D are the relative bottom and top elevations respectively.*

The Figures B-5, B-6 and B-7 show the effect of wave height H on the flow rate and geometric tube distortions. The flow rate increases with H since wave energy is directly proportional to square of amplitude of the waves as discussed in chapter 4. The tube distortions increase with wave height. The tube distortions are responsible for the peristaltic flow of water in the tube so increase in tube distortions has effect of increasing flow rate.

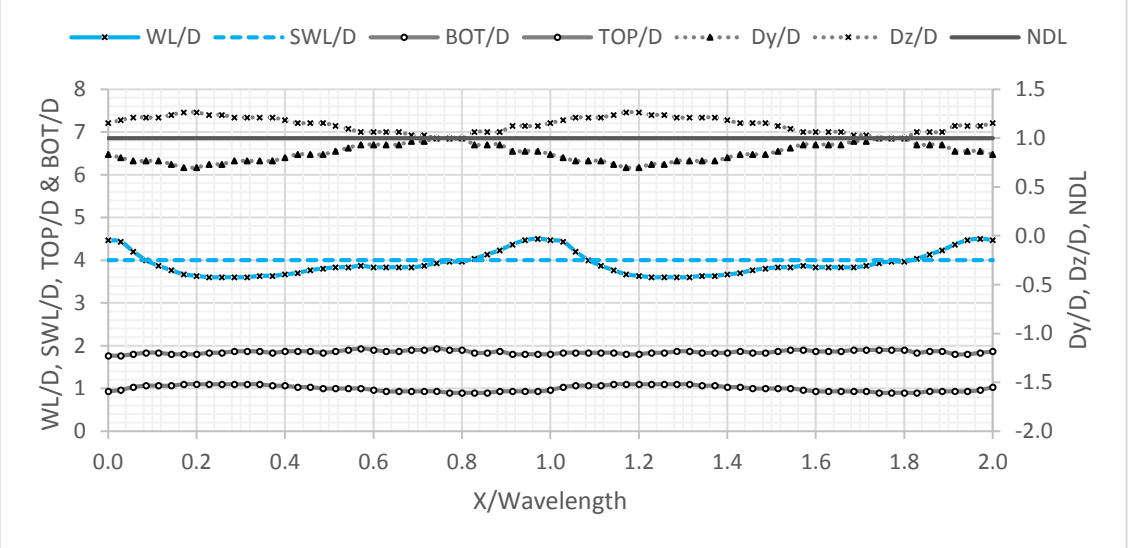

Figure B-5 *Tube deformation along the flume as the ratios D_y/D and D_z/D for vertical and horizontal deformations respectively at an average wave height H of 27mm, a flow rate of 4.6ml/s and pressure head of 0mm. SWL and NDL are the 'still water level' and 'no deformation line' respectively. BOT/D and TOP/D are the relative bottom and top elevations respectively.*

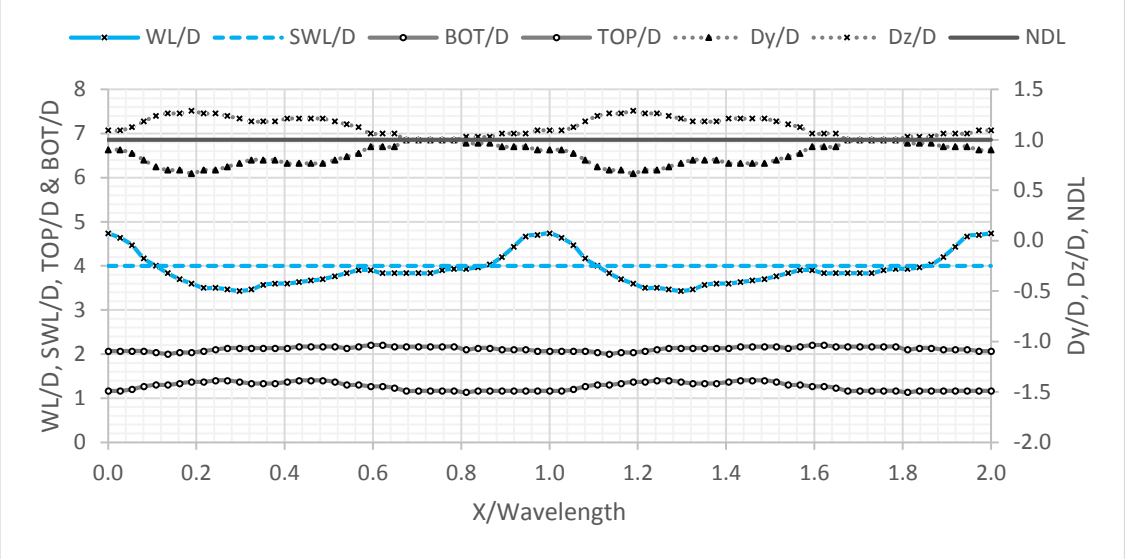

Figure B-6 *Tube deformation along the flume as the ratios D_y/D and D_z/D for vertical and horizontal deformations respectively at an average wave height H of 39mm, a flow rate of 8.6ml/s and pressure head of 0mm. SWL and NDL are the 'still water level' and 'no deformation line' respectively. BOT/D and TOP/D are the relative bottom and top elevations respectively.*

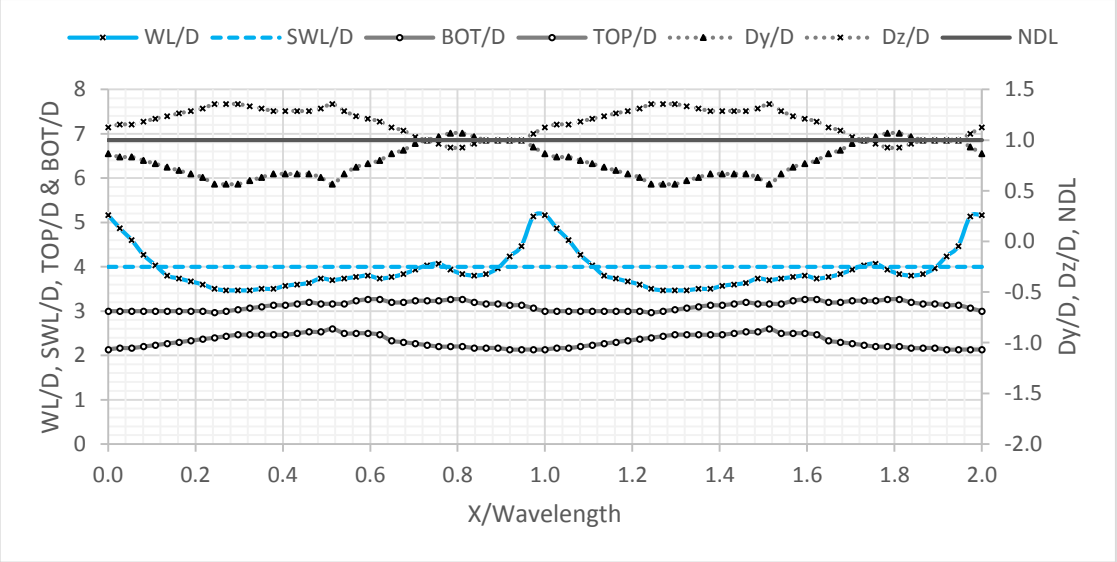

Figure B-7 *Tube deformation along the flume as the ratios D_y/D and D_z/D for vertical and horizontal deformations respectively at an average wave height H of 51mm, a flow rate of 16.7ml/s and pressure head of 0mm. SWL and NDL are the 'still water level' and 'no deformation line' respectively. BOT/D and TOP/D are the relative bottom and top elevations respectively*